

ARTICLE

<https://doi.org/10.1038/s41467-019-11231-8>

OPEN

Molecular mechanism of cytoplasmic dynein tension sensing

Lu Rao¹, Florian Berger ², Matthew P. Nicholas^{1,3,4} & Arne Gennerich ¹

Cytoplasmic dynein is the most complex cytoskeletal motor protein and is responsible for numerous biological functions. Essential to dynein's function is its capacity to respond anisotropically to tension, so that its microtubule-binding domains bind microtubules more strongly when under backward load than forward load. The structural mechanisms by which dynein senses directional tension, however, are unknown. Using a combination of optical tweezers, mutagenesis, and chemical cross-linking, we show that three structural elements protruding from the motor domain—the linker, buttress, and stalk—together regulate directional tension-sensing. We demonstrate that dynein's anisotropic response to directional tension is mediated by sliding of the coiled-coils of the stalk, and that coordinated conformational changes of dynein's linker and buttress control this process. We also demonstrate that the stalk coiled-coils assume a previously undescribed registry during dynein's stepping cycle. We propose a revised model of dynein's mechanochemical cycle which accounts for our findings.

¹Department of Anatomy and Structural Biology and Gruss Lipper Biophotonics Center, Albert Einstein College of Medicine, Bronx, NY 10461, USA.

²Laboratory of Sensory Neuroscience, Rockefeller University, New York, NY 10065, USA. ³Medical Scientist Training Program, Albert Einstein College of Medicine, Bronx, NY 10461, USA. ⁴Present address: Flaum Eye Institute, University of Rochester Medical Center, 210 Crittenden Blvd, Rochester, NY 14642, USA. Correspondence and requests for materials should be addressed to A.G. (email: arne.gennerich@einstein.yu.edu)

The microtubule (MT) transport system regulates essential eukaryotic activities, including cell division, cell migration and the transport of subcellular cargoes. Cytoplasmic dynein (referred to here as dynein), is a key mediator of these activities, serving as the major generator of MT minus-end-directed motility. Dynein's cargoes include nuclei and other organelles, proteins, mRNAs, and even viruses^{1–3}. Not surprisingly, its dysfunction is implicated in a growing number of human diseases^{4–10} termed dyneinopathies¹¹.

Dynein is a AAA+ATPase (AAA: ATPase associated with various cellular activities¹²) and is the largest and most complex cytoskeletal motor protein. It is a ~1.4 MDa protein complex composed of two identical heavy chains (HCs) and several other associated chains and accessory proteins that regulate dynein and bind it to cargo¹. Each HC contains a C-terminal ring-shaped motor domain (MD) composed of six tandem-linked AAA modules (AAA1–6), the first four of which (AAA1–4) can hydrolyze and/or bind nucleotide^{13,14} (Fig. 1a, b). By contrast, the other cytoskeletal motors, kinesin^{15–17} and myosin^{18,19}, have one ATPase per HC. While their ATPase cores directly interact with their cytoskeletal tracks, in dynein, a ~15-nm coiled-coil (CC) stalk emerges from AAA4¹³ and separates dynein's MT-binding domain (MTBD) from the AAA ring domain²⁰ (Fig. 1a, b). A second antiparallel coiled-coil called the buttress²⁰ (or strut²¹)

protrudes from AAA5 and contacts the stalk (Fig. 1b). Finally, a ~10-nm linker connects the N-terminal dimerizing tail domain to the AAA ring. The linker undergoes cyclic conformational changes that generate unidirectional motion and force^{22,23} (Fig. 1b).

The stalk acts as a bidirectional communication pathway between the AAA ring and MTBD: nucleotide state affects MT binding and vice versa^{24,25}. The registrations of the stalk coiled-coil (CC) helices (CC1 and CC2) influence both dynein's MT-binding affinity and the ATPase activities of the MD^{26,27}. In solution, the stalk helices predominately assume a low-affinity registration called the β + registration^{27,28} (referred to as β hereafter), and upon MT binding, transition to a high-affinity (α) registration^{29,30} (Fig. 1c). Communication along the stalk requires stalk-buttress interactions, as deletion of the buttress uncouples ATPase activity from MT binding^{14,31}. The linker also mediates communication between the AAA ring and MTBD, as preventing interactions between the linker and AAA5 prevents ATP-induced MT release¹³. However, how the stalk, buttress and linker work together to regulate dynein's MT interactions remains unknown.

We are only beginning to understand how dynein moves processively (the ability to take multiple steps before dissociating) against opposing forces. To move processively, one MD (head)

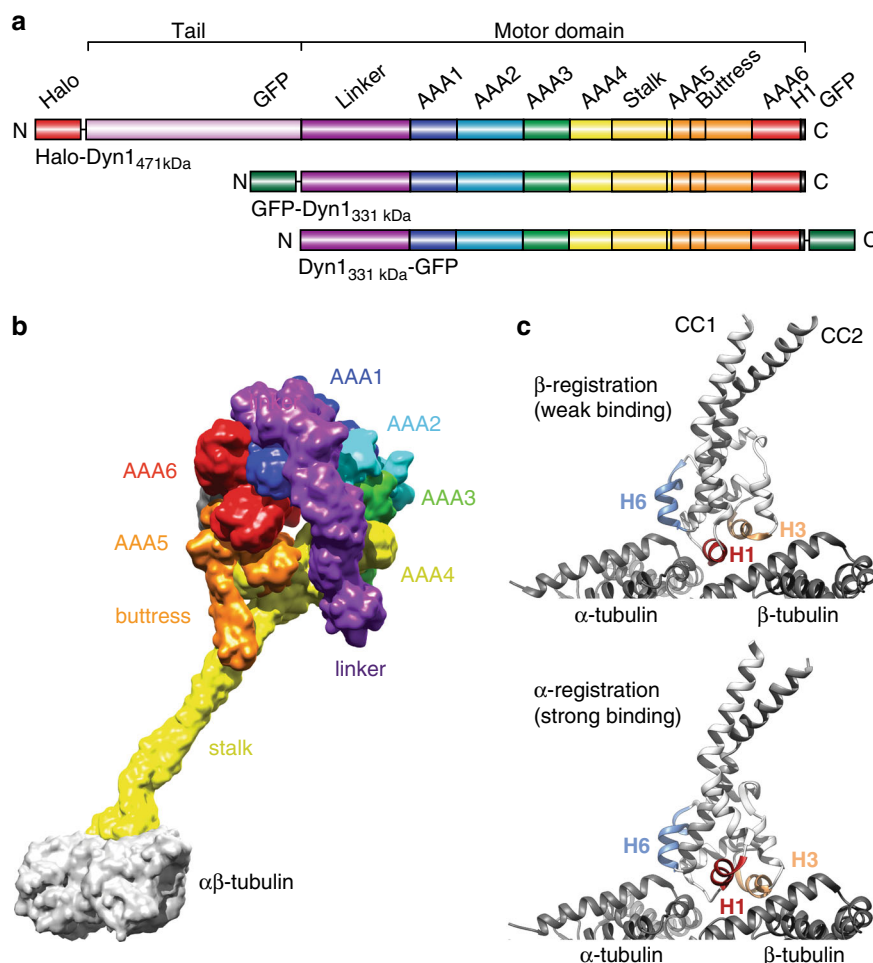


Fig. 1 Domain organization of cytoplasmic dynein and low- and high-affinity MT-bound states of the dynein MTBD. **a** Organization of the full-length cytoplasmic dynein heavy chain (HC) with an N-terminal Halo-Tag, Halo-Dyn1_{471kDa} (a.a. 1–4092) and the tail-truncated monomeric constructs, GFP-Dyn1_{331kDa} and Dyn1_{331kDa}-GFP (a.a. 1219–4092). **b** Dynein MD bound to α / β -tubulin in the strong binding state (merged from PDB entries 3VKG and 3JIT; see Supplementary Note 1). **c** MT-bound MTBD in the weak MT-binding β -registration of the stalk helices (top, PDB entry 3J1U) and in the strong MT-binding α -registration (bottom, PDB entry 3J1T)

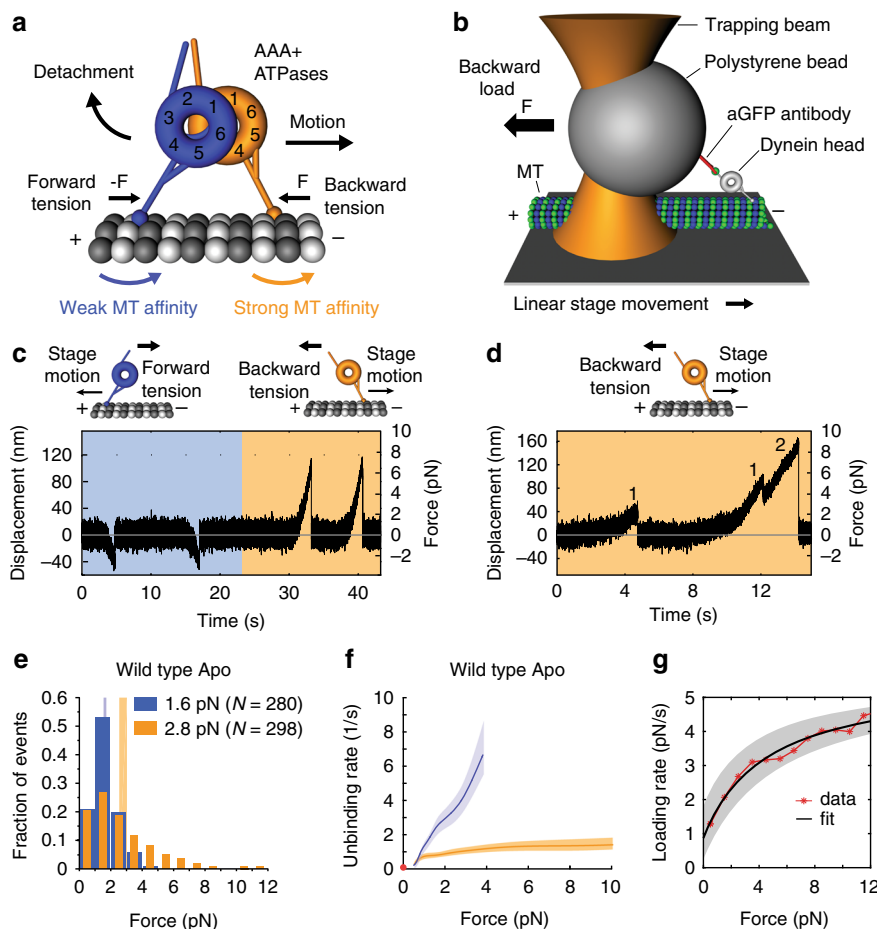


Fig. 2 Dynein-MT bond anisotropy. **a** Model for tension-based regulation of dynein stepping. Splaying of the dynein heads generates intramolecular tension. Under backward tension (front head) MT-binding strength is greater, and under forward tension (rear head) it decreases. **b** A polystyrene bead bearing a dynein MD is held in an optical trap as the microscope stage sweeps back and forth parallel to a MT (not to scale). **c** Force (position) vs. time for WT dynein (GFP-Dyn1_{331kDa}) in the apo state (see “Methods” section) acquired under non-reducing conditions. Orange and blue areas are periods of applied backward and forward tension, respectively. **d** Primary and secondary unbinding events. Event 1 is a primary event, beginning from zero force ($F_{start} = 0$). Secondary events (2) occur when the MD rebinds the MT before returning to the trap center, and thus $F_{start} > 0$. **e** Normalized histograms of primary forward (blue) and backward (orange) unbinding forces, with mean values noted (we plot the absolute force values to facilitate comparison of the unbinding-force distributions in both loading directions). Vertical bands are 95% CIs of the mean (forward: [1.5, 1.7] pN, backward: [2.5, 3.0] pN) estimated by bootstrapping 4,000 samples (source data are provided as a Source Data file). **f** Unbinding rate vs. force derived from the data in (e). The shaded areas are 95% CIs for the mean rates, estimated by bootstrapping. The depicted zero-load unbinding rate of $0.086 \pm 0.002 \text{ s}^{-1}$ (\pm SE, red circle) represents the inverse of the time constant obtained from the analysis of the experimental CDF of the MT-bound lifetimes measured via TIRF microscopy (Supplementary Fig. 2a) (the 95% CIs of the measured unbinding rate (lower limit, 0.084/s; upper limit, 0.11/s) are not shown as they are shorter than the height of the symbol). **g** Loading rate vs. force obtained from line fits to the 200-ms data segment before detachment of each measured unbinding-force event (see Supplementary Fig. 3 for underlying data)

must bind the MT tightly while the other head detaches and advances (Fig. 2a). Dynein accomplishes this in part by employing a tension-direction-dependent MT-binding strength^{32,33}. In nucleotide-free conditions, when force is applied to a MD in the forward direction (when the MD is pulled toward the MT minus-end), it forms a slip bond with MTs, exhibiting faster unbinding with increasing tension. However, when the MD is subjected to a hindering or backward load (pulled toward the MT plus end), it forms a slip-ideal bond with MTs, exhibiting faster unbinding for backward forces up to ~2 pN and constant, force-independent unbinding rates for greater forces³². This anisotropic MT-binding behavior explains why the likelihood for trailing head detachment (and subsequent forward movement) increases with the distance between the two heads^{34,35}. Thus, interhead tension, which increases as the heads spread apart, helps keep the dynein

heads out-of-phase¹⁵. These results imply that both external load and intramolecular tension contribute to the control of dynein motion along MTs.

By what structural mechanisms does tension alter dynein function? What roles do the stalk, buttress and linker play in dynein’s response to load? Here we combine structure-function, mutagenesis and chemical cross-linking with single-molecule optical tweezers studies to answer these questions. We demonstrate that the anisotropic effect of tension on the MT-binding strength arises from force-induced sliding of the helices in the stalk, and that coordinated conformational changes of dynein’s linker and buttress control this process. In addition, we show that dynein assumes a previously undescribed stalk registration under forward load in the nucleotide-free state which we term the γ -registration. Our results illustrate how, in response to tension, a complex interplay between the linker, stalk, and buttress control

conformational changes in the MTBD, facilitating the coordinated movements of dynein's MDs.

Results

Tension regulates MT-binding via stalk helix sliding. We previously demonstrated that a single dynein head responds anisotropically to tension³². Consistent with other reports^{33,36}, a dynein head binds tighter to MTs when pulled toward the MT plus end (Fig. 2b–f). We reasoned that this behavior might result from tension-induced reconfiguration of the coiled-coil stalk and/or force-induced changes in the MTBD or MT lattice³². Since the stalk configuration is known to influence MT affinity in the absence of load^{26,27}, we first tested whether dynein's anisotropic MT-binding strength is caused by a tension-direction-dependent sliding of dynein's stalk helices.

To prevent tension-induced stalk helix sliding, we introduced cysteine residues in the outgoing (CC1) and return (CC2) α -helices of the stalk of Dyn1_{331kDa}, a minimal *S. cerevisiae* MD that contains the linker and the AAA ring, and the stalk and MTBD. Dyn1_{331kDa} retains its motor activities^{32,33,37} and is equivalent to the *Dictyostelium discoideum* MD used in key biochemical studies^{22,26,38–41} (see Supplementary Fig. 1a for sequence alignment). The addition of the cysteine residues enabled reversible disulfide cross-linking. Under non-reducing conditions (without DTT) following oxidation²⁶, the stalk helices were cross-linked with an efficiency of >95% (Supplementary Note 2). Since our previous optical tweezers-based unbinding-force experiments were performed under reducing conditions³², we repeated the experiments with WT dynein and found that WT motors showed anisotropic responses under both reducing³² and non-reducing conditions (Fig. 2c–f). Thus, we can compare the anisotropic behavior of WT dynein with the tension response of the cross-linked constructs under non-reducing conditions.

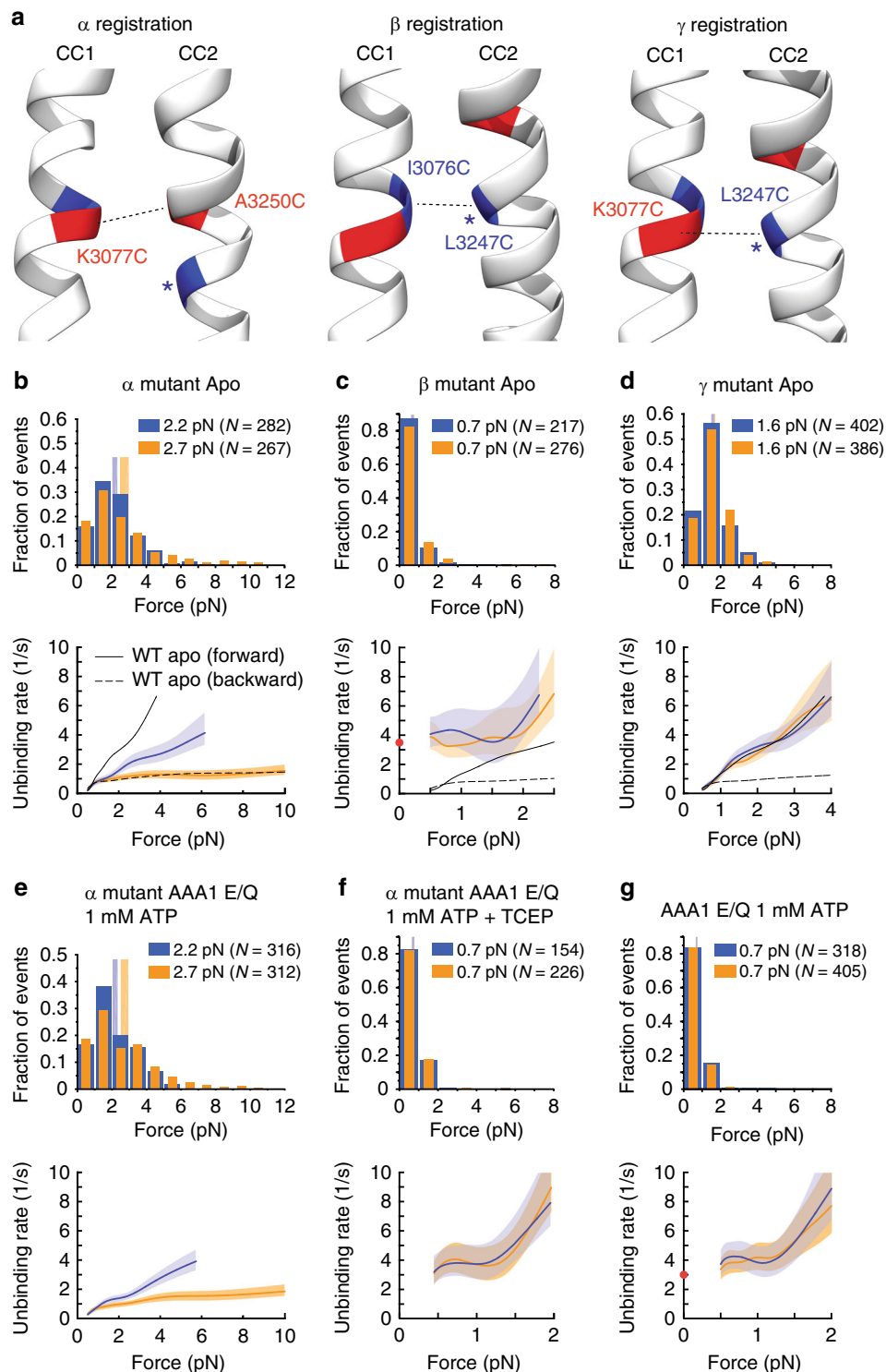
We then cross-linked the stalk helices in the high-affinity α -registry (K3077C and A3250C, Supplementary Fig. 1b) (Fig. 3a, b) and the low-affinity β -registry²⁷ (I3076C and L3247C, Supplementary Fig. 1b) and measured the unbinding behaviors of the cross-linked (CL) constructs (Fig. 3a, c). Cross-linking the stalk helices in the α -registry significantly reduces dynein's anisotropic response to directional tension in the absence of nucleotides ($p_m < 10^{-10}$ [Dyn1_{331kDa} apo forward vs. Dyn1_{331kDa} apo backward], and $p_m = 0.03$ [Dyn1_{331kDa}- α CL apo forward vs. Dyn1_{331kDa}- α CL apo backward] (Figs. 2e, f and 3a, b), with p_m being an estimate for the p -value for the difference of the means, see “Methods” section). When locked in the α -registry, dynein's slip bond with the MT under forward load became significantly stronger (Fig. 2e, f) (Dyn1_{331kDa} apo forward 1.6 [1.5, 1.7] pN vs. Dyn1_{331kDa}- α CL apo forward 2.2 [2.0, 2.3] pN, Fig. 3b). Under backward load, Dyn1_{331kDa}- α CL exhibited slip-ideal bonding statistically indistinguishable from WT Dyn1_{331kDa} ($p_{ks} = 0.83$ [Dyn1_{331kDa}- α CL apo backward vs. Dyn1_{331kDa} apo backward], with p_{ks} being the p -value resulting from a two-sample Kolmogorov–Smirnov (KS) test of the cumulative distribution functions (CDFs) calculated from the measured histograms of primary unbinding forces, see “Methods” section). In contrast, cross-linking the stalk helices in the β -registry caused dynein to respond isotropically to tension in nucleotide-free conditions (Fig. 3a, c). The β -registry resulted in weak MT-binding in both directions (forward 0.7 [0.7, 0.8] pN vs. backward 0.7 [0.6, 0.7] pN, $p_{ks} = 0.59$, Fig. 3c).

The β -registry results in an ideal-slip bond with MTs. The force-dependent unbinding rates of the dynein β -mutant remain relatively constant in both directions for forces up to ~1.5 pN (ideal bonding) and then increase with increasing load (slip

bonding) (Fig. 3c, bottom). To determine whether the β -mutant also exhibits ideal-bond behavior even down to zero load (as suggested by the unbinding rates for ~0.5–1.5 pN), we used a total internal reflection fluorescence (TIRF) assay to determine the unbinding rate of the β -mutant at zero load. Using surface-immobilized MTs, we imaged the binding and dissociation of our β -mutant heads (labeled with Cy3 via an inserted N-terminal SNAP-tag) at 100 ms/frame and determined an average MT-bound time of ~290 ms, corresponding to an unbinding rate of $3.5 \pm 0.1 \text{ s}^{-1}$ (mean \pm SEM; Supplementary Fig. 2b and Fig. 3c, red circle). The unbinding rate falls within the CIs of the unbinding rates in the ~0.5–1 pN force range and is therefore consistent with an ideal-bond behavior down to zero load. Of note, recent studies by the Howard and Ostap labs have shown that the vertical force component in single-head assays can increase the detachment rate of kinesin motors^{42,43}. As a dynein head could also be sensitive to vertical forces, it is possible that the zero-force unbinding rate projected based on the apparent ideal-bond behavior in the ~0.5–1.5 pN force range overestimates the zero-force detachment rate. In conclusion, the dominant unbinding behavior of the β -mutant is largely insensitive to forces below ~1.5 pN and increases rapidly with force above this value, a behavior we term ideal-slip bonding.

ATP-bound dynein assumes the β -registration. It is known that ATP binding to AAA1 induces a weak MT-binding state. We hypothesized that this is mediated by the stalk sliding into the β -registration. To test this, we compared the bond behaviors of the non-cross-linked WT motor bearing an E/Q mutation in the AAA1 Walker B motif (which allows ATP binding but prevents ATP hydrolysis) with the behavior of the β -mutant. In the presence of ATP, AAA1 E/Q Dyn1_{331kDa} shows markedly weaker unbinding forces (mean < 1 pN) in both directions compared to nucleotide-free conditions (Figs. 2e and 3g)³². Similar to the cross-linked β -mutant, the non-cross-linked AAA1 E/Q Dyn1_{331kDa} mutant in the presence of ATP exhibits slip bond behaviors in both directions for forces above ~1 pN and a similar zero-load unbinding rate ($3.0 \pm 0.1 \text{ s}^{-1}$, Supplementary Fig. 2c and Fig. 3c, g). In contrast, the cross-linked AAA1 E/Q α -mutant shows ATP-insensitive slip bonding under forward load and slip-ideal bonding under backward load (Fig. 3e), with statistically indistinguishable unbinding-force behavior from the Dyn1_{331kDa}- α CL motor in the apo state ($p_{ks} = 0.88$ [AAA1 E/Q Dyn1_{331kDa}- α CL ATP forward vs. Dyn1_{331kDa}- α CL apo forward] and $p_{ks} = 0.94$ [AAA1 E/Q Dyn1_{331kDa}- α CL ATP backward vs. Dyn1_{331kDa}- α CL apo backward], Fig. 3b, e). MT-binding sensitivity to ATP is restored to the AAA1 E/Q α -mutant when 2 mM TCEP (a reducing agent that breaks disulfide bonds) is added to reverse the cross-linking of the stalk helices. With TCEP present, ATP induces markedly weaker unbinding forces (mean < 1 pN) in both directions (Fig. 3f). These studies demonstrate that ATP binding to AAA1 induces the β -registration.

Forward load induces an intermediate stalk registry. Notably, under forward load (when pulled toward the MT minus-end) in the absence of ATP, the mean unbinding force of Dyn1_{331kDa} (1.6 pN) (Fig. 2e) is significantly larger than that of Dyn1_{331kDa}- β CL (0.7 pN) (Fig. 3c) ($p_m < 10^{-10}$). This suggests that the apo-state WT motor assumes a stalk configuration under forward load that is distinct from the β and α -registrations. We hypothesized that this stalk helix registration is a registration in between the weak (β) and strong (α) MT-binding registries, which we name the γ -registration (Fig. 3a). To test our hypothesis, we cross-linked the stalk helices a half registry in between the β - and α -registrations, so that K3077 of CC1



aligns with L3247 of CC2 (Fig. 3a, right, and Supplementary Fig. 1b). Cross-linking in the γ -registry results not only in a direction-independent slip bond with the MT (as observed for the apo-state WT MD under forward load; Fig. 2f) ($p_{ks} = 0.2$ [Dyn1_{331 kDa}- γ CL forward vs. Dyn1_{331 kDa}- γ CL backward], Fig. 3d), but also in MT-binding strengths statistically indistinguishable from the unbinding-force distribution of the apo-state WT motor under forward load ($p_{ks} = 0.43$ [Dyn1_{331 kDa}- γ CL forward vs. Dyn1_{331 kDa} apo forward], Figs. 2e and 3d). Thus, taken together, our results suggest that backward load induces the α -registration, while forward load

induces a previously undescribed γ -registry in the absence of nucleotides, and upon ATP binding to AAA1, the stalk assumes the β -registry.

MT-binding asymmetry involves stalk sliding and the AAA ring. We previously demonstrated that ATP binding to AAA1 (Fig. 3g) and ADP binding to AAA3 both reduce bond-strength anisotropy, while ADP binding to AAA1 strengthens it³², suggesting the AAA ring regulates bond strength anisotropy. However, Cleary and coworkers reported results suggesting the AAA

Fig. 3 Tension direction alters dynein MT-binding strength via sliding of the stalk helices. **a** High-affinity (α), low-affinity (β) and intermediate-affinity (γ) helix registrations of the dynein stalk generated from the morphing structure described in the Supplementary Note 1. **b**, top: Normalized histograms of primary forward and backward unbinding forces for the Dyn_{1331kDa}- α CL mutant, with mean values noted (95% CIs [2.0, 2.3] and [2.5, 3.0] pN, estimated by bootstrapping 4000 samples). **b**, bottom: Unbinding rate vs. force derived from the data above. The shaded areas are 95% CIs for the mean rates, estimated by bootstrapping. **c** As in (**b**), but for the Dyn_{1331kDa}- β CL mutant (95% CIs [0.6, 0.7] and [0.7, 0.8] pN). The depicted zero-load unbinding rate of $3.5 \pm 0.1 \text{ s}^{-1}$ (characteristic rate \pm SEM) (red circle) represents the inverse of the time constant obtained from the CDF analysis of the MT-bound lifetimes measured via TIRF microscopy (Supplementary Fig. 2c) (the 95% CIs of the measured unbinding rate (lower limit, 3.3/s; upper limit, 3.6/s) are not shown as they are shorter than the height of the symbol). **d** As in **b**, but for the Dyn_{1331kDa}- γ CL mutant (95% CIs [1.5, 1.7] and [1.6, 1.7] pN). **e** As in (**b**), but for the AAA1 E/Q Dyn_{1331kDa}- α CL mutant and 1 mM ATP (95% CIs [2.0, 2.3] and [2.5, 3.0] pN). **f** As in (**e**), but with 2 mM TCEP to cleave the disulfide bonds of the stalk helices (95% CIs [0.6, 0.8] and [0.7, 0.8] pN). **g** As in (**b**) but for the AAA1 E/Q Dyn_{1331kDa} mutant and 1 mM ATP (95% CIs [0.7, 0.7] and [0.7, 0.7] pN). The depicted zero-load unbinding rate of $3.0 \pm 0.1 \text{ s}^{-1}$ (red circle) was derived from Supplementary Fig. 2d as described for the zero-load unbinding rate in **c** (the 95% CIs of the measured unbinding rate (lower limit, 2.8/s; upper limit, 3.1/s) are not shown as they are shorter than the height of the symbol). For comparison, the force-dependent unbinding rates of the WT motor in the apo state are shown in (**b-d**) (dashed and solid black lines). Source data are provided as a Source Data file

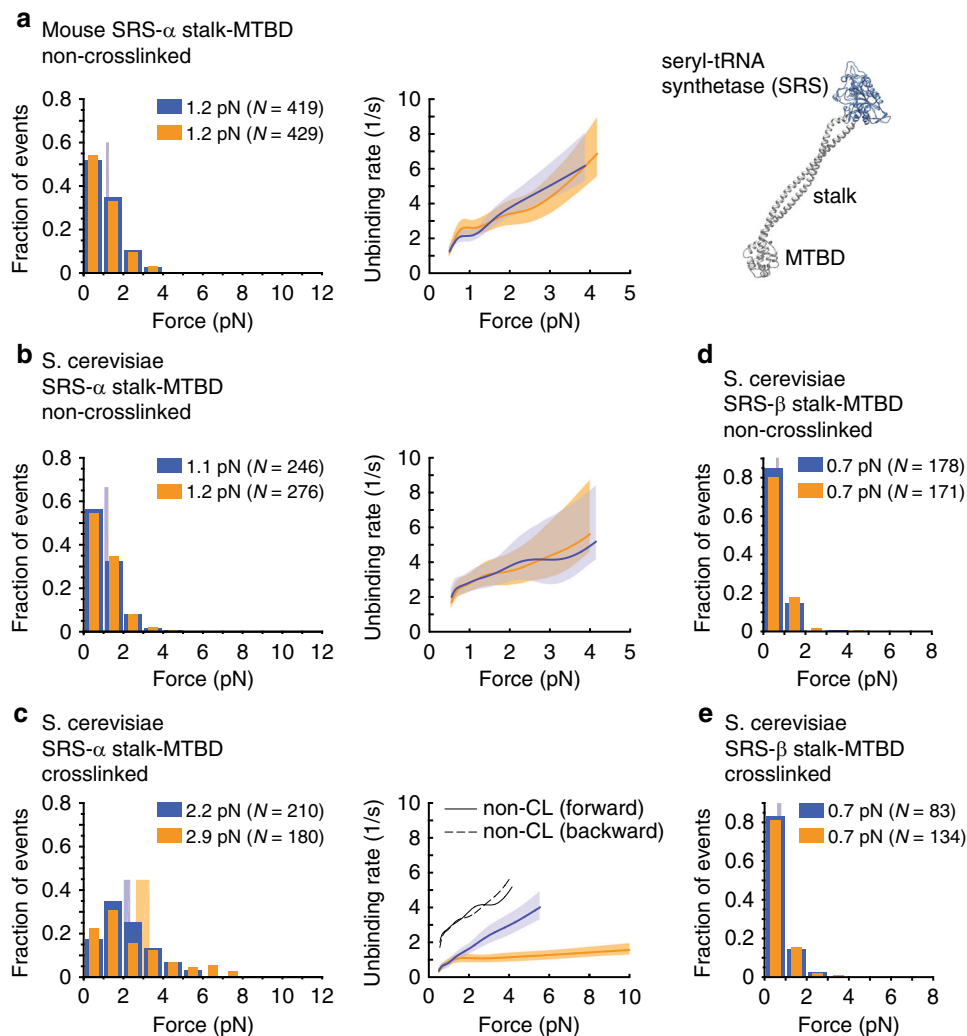


Fig. 4 Unbinding-force behaviors of the SRS-stalk-MTBD constructs. **a**, left: Normalized histograms of primary forward and backward unbinding forces for the SRS construct with the mouse stalk helices (a.a. 3019–3309) fused in the non-cross-linked α -registry (SRS 85:82), with mean values noted (95% CIs [1.1, 1.3] and [1.1, 1.3] pN, estimated by bootstrapping 4,000 samples). **a**, middle: Unbinding rate vs. force derived from the data on the left. The shaded areas are 95% CIs for the mean rates, estimated by bootstrapping. **a**, right: Model of monomeric *T. thermophilus* seryl-tRNA synthetase (SRS) (based on PDB entry 3ERR) fused to the near-full-length stalk and MTBD of dynein in the β -registry of the stalk helices (generated by aligning PDB entry 3WUQ and 4RH7, see Supplementary Note 1). **b** As in (**a**) but for the SRS construct with the *S. cerevisiae* stalk helices (a.a. 3019–3309) fused in the non-cross-linked α -registry (95% CIs [1.0, 1.2] and [1.1, 1.2] pN). **c** As in (**b**) but with the stalk helices cross-linked (K3077C, A3250C) in the α -registration (95% CIs [2.0, 2.4] and [2.6, 3.3] pN). **d** As in (**b**) but for SRS fused to the *S. cerevisiae* stalk and MTBD in the weak MT-binding β -registry (SRS 89:82) (a.a. 3015–3309) (95% CIs [0.6, 0.7] and [0.6, 0.7] pN). **e** As in (**d**) but with the stalk helices cross-linked (I3076C, L3247C) in the β -registration (95% CIs [0.6, 0.7] and [0.7, 0.8] pN). Source data are provided as a Source Data file

ring was not needed for dynein's anisotropic response to directional tension. When the mouse stalk and MTBD was fused to the coiled-coil base of *T. thermophilus* seryl-tRNA synthetase (SRS) in the α -registry (SRS- α stalk-MTBD), significant bond-strength anisotropy was observed³³ (these chimeric fusion constructs were used by Gibbons et al. to establish the α - and β -registries²⁷; Fig. 4a, right). This result suggested that bond-strength anisotropy is intrinsic to the stalk and MTBD, and not dependent on other structural elements, such as the AAA ring, linker, or buttress. In contrast, we did not observe significant bond-strength anisotropies for the SRS- α stalk-MTBD fusion construct with the mouse stalk-MTBD sequence ($p_{ks} = 0.38$ [forward vs. backward]; Fig. 4a) or the yeast stalk-MTBD sequence ($p_{ks} = 0.62$ [forward vs. backward]; Fig. 4b) in the absence of stalk cross-linking. To determine the reason for this discrepancy, we repeated the experiments with the mouse SRS- α stalk-MTBD construct on axonemes, the substrate used by Cleary and coworkers³³. As in the case of MTs, we observed no anisotropic MT-binding strength ($p_{ks} = 0.62$ [forward vs. backward]; Supplementary Fig. 4a). The cause for the different outcomes must therefore lie in the different unbinding-force assays used. Indeed, when we applied the oscillatory assay (Supplementary Note 3) used by Cleary et al. (in contrast to the constant-pulling assay used herein, Methods), we were able to reproduce the anisotropic unbinding behavior reported by Cleary and coworkers³³ (Supplementary Figs. 5–7).

Notably, the unbinding rates obtained from the two assays differed only under forward load (Supplementary Fig. 7). We wondered what might account for the significant increase in unbinding rates under forward load in the oscillatory assay compared to the constant-pulling assay. In the oscillatory assay, the trap moves very rapidly between two positions (± 250 nm) at an initial speed of ~ 1 mm/s (see Supplementary Note 4), whereas in the constant-pulling assay used herein, the coverslip-attached MT moves at a constant velocity of only ~ 100 nm/s past the stationary trapped bead. In the oscillatory assay, the binding of the SRS-stalk-MTBD construct to the MT most likely occurs during the extended dwelling of the bead in between the switching events⁴⁴. It is therefore possible that the extremely high loading rates at the beginning of the trap displacement modify the unbinding pathway of the MTBD-MT bond when the load is applied in the forward direction and reduce the bond lifetime (rates of up to $\sim 25,000$ pN/s can be produced, see Supplementary Note 4 and Supplementary Fig. 8).

Further comparison of the SRS- α stalk-MTBD construct using the constant-pulling assay reveals that an anisotropic response to directional tension is only observed when the stalk helices are cross-linked in the α -registry (Fig. 4c). Notably, the cross-linked SRS- α stalk-MTBD construct shows statistically indistinguishable behavior from the dynein MD with the cross-linked α -registry, Dyn1_{331kDa}- α CL (Fig. 3b and Fig. 4c). In contrast, the frequently used non-cross-linked SRS- α stalk-MTBD construct shows significantly different unbinding behavior from the cross-linked SRS- α stalk-MTBD construct ($p_{ks} < 10^{-21}$ [SRS- α stalk-MTBD forward vs. SRS- α stalk-MTBD CL forward], and $p_{ks} < 10^{-19}$ [SRS- α stalk-MTBD backward vs. SRS- α stalk-MTBD CL backward], Fig. 4b, c), suggesting that the non-cross-linked SRS- α stalk-MTBD construct does actually not assume the α -registry. However, the SRS- β stalk-MTBD construct shows the same unbinding behaviors whether the stalk helices are cross-linked in the β -registry or not ($p_{ks} = 0.76$ [SRS- β stalk-MTBD forward vs. SRS- β stalk-MTBD CL forward] and $p_{ks} = 0.42$ [SRS- β stalk-MTBD backward vs. SRS- β stalk-MTBD CL backward], Fig. 4d, e). This suggests that the SRS- β stalk-MTBD construct assumes the β -registry with or without stalk cross-linking. We conclude that the constant-pulling assay used herein provides

accurate data also when analyzing the short SRS fusion constructs.

Together, our data indicate that either tension-induced helix sliding is somehow prevented in the non-cross-linked SRS constructs when bound to the MT, or that other elements, such as the AAA ring, buttress, and linker, are required for registration changes of the stalk helices in response to directional tension (for a detailed discussion on why the stalk helices of the SRS- α stalk-MTBD construct can be cross-linked in different registrations in solution while directional tension alone is incapable of inducing registration changes, see Supplementary Note 5). We sought to further understand how tension induces helix sliding and to elucidate the roles of the AAA ring and its appendages in this process.

Tension-induced stalk sliding requires the buttress. In the absence of load, nucleotide state and MT binding affect one another^{24,25,27,38} via helix sliding²⁶, and helix sliding is facilitated by the coiled-coil buttress¹⁴ (Fig. 5a). ATP binding to AAA1 causes closure of the AAA ring, forcing subdomains of AAA6 and AAA5 to rotate⁴⁵ (Fig. 5a). This rotation displaces the buttress, which in turn appears to induce sliding of the stalk helices and transition from a strong to a weak MT-binding state (Figs. 1c and 5a). We hypothesized that the buttress also facilitates tension-induced helix sliding. To test this, we prevented stalk-buttress interactions by replacing the distal end of the buttress with a flexible linker (GSGS), similar to a construct used previously to uncouple ATPase activities from MT binding¹⁴ (Δ BUT, Fig. 5b). As expected, this mutant shows weak and symmetric unbinding forces in the apo state ($p_{ks} = 0.53$, forward vs. backward) and mean unbinding forces statistically indistinguishable from Dyn1_{331kDa}- β CL ($p_m = 0.31$ (forward) and $p_m = 0.36$ (backward), Figs. 3c and 5c). Thus, the tension-induced anisotropy of the dynein-MT bond depends on tension-induced conformational changes within the AAA ring that are transmitted to the stalk via the buttress.

AAA5-linker interactions control stalk helix sliding. In the nucleotide-free, post-powerstroke state, the linker contacts conserved residues in AAA5¹³ (Fig. 6a, b). As disruption of the linker-docking site in AAA5 severely reduces MT-activated ATPase activity, ATP-induced release from MTs, and dynein motility¹³, we sought to determine whether the conformation of the linker affects the buttress-mediated sliding of the stalk helices.

Comparison of the apo-state unbinding-force histograms acquired under forward load of Dyn1_{331kDa} (Fig. 2e) and Dyn1_{331kDa}- β CL (Fig. 3c) shows that forward tension alone is incapable of changing the γ -registration of the stalk helices (Fig. 3d) into the β -registry (Fig. 3c). However, ATP binding to AAA1 results in mean unbinding forces statistically indistinguishable from the β -mutant ($p_m = 0.31$ (forward) and $p_m = 0.79$ (backward) [AAA1 E/Q Dyn1_{331kDa} ATP vs. Dyn1_{331kDa}- β CL], Fig. 3c, g). Since ATP binding to AAA1 causes the transition from the post- to the pre-powerstroke conformational state of the linker²², we hypothesized that linker docking to AAA5 in the post-powerstroke linker conformation blocks transition into the β -registry. To test this idea, we mutated the highly conserved residue F3446 in the AAA5 linker-docking site (Fig. 6a, inset, and Fig. 6b) into glutamic acid, which impairs MT-activated ATPase activity¹³. Indeed, this mutant, F3446E-Dyn1_{331kDa}, shows β -mutant-like mean unbinding forces ($p_m = 0.17$ (forward) and $p_m = 0.35$ (backward) [F3446E-Dyn1_{331kDa} ATP vs. Dyn1_{331kDa}- β CL], Figs. 3c and 6b).

The interactions between the linker and AAA5 could sterically or allosterically affect the base of the buttress and thereby affect

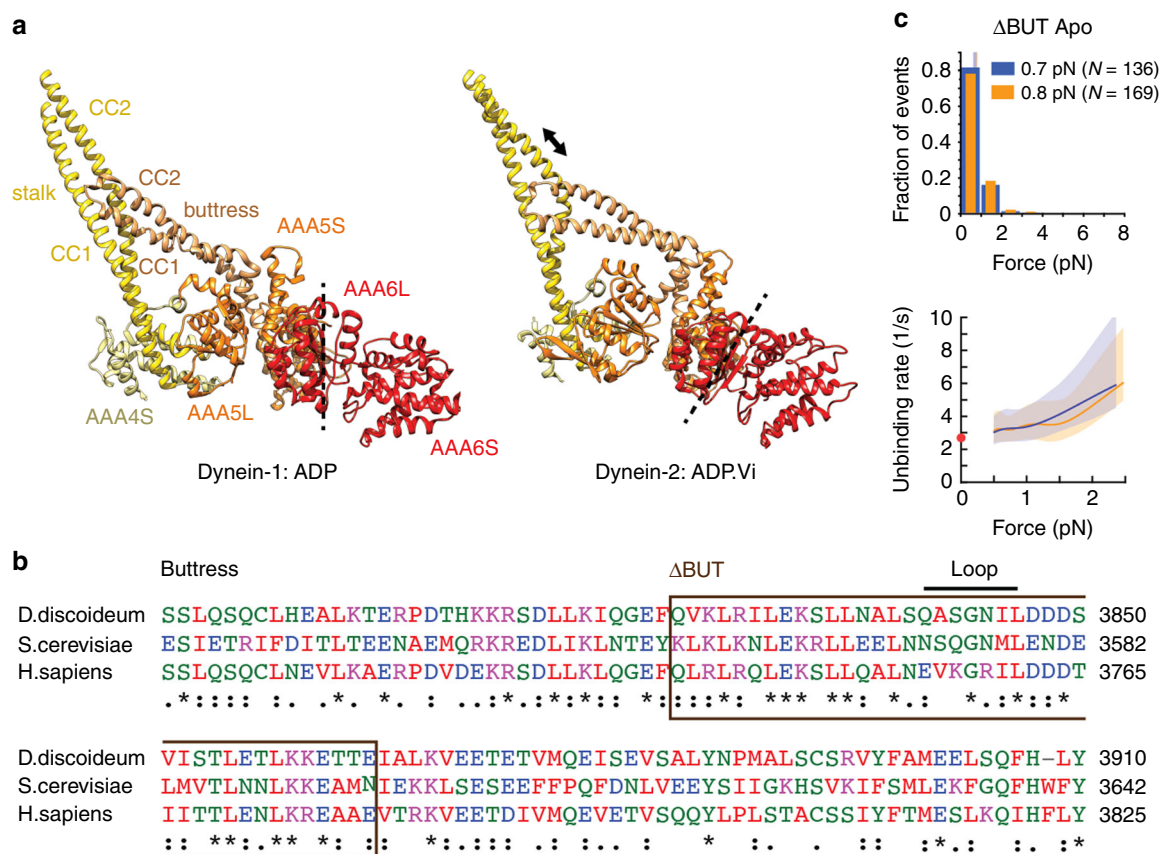


Fig. 5 Tension-induced registry changes of the stalk helices require stalk-buttress interactions. **a** A comparison of the crystal structures of dynein-ADP (PDB entry 3VKG¹⁴) and dynein-ADP.Vi (PDB: 4RH7⁴⁷) suggests that ATP binding to AAA1 causes a rotation of AAA6L/AAA5S (the dashed line indicates the orientation of AAA6L), resulting in displacement of the buttress (orange) and sliding of CC2 relative to CC1 (arrow), which in turn induces the low-affinity MT-bound state⁴⁵. **b** Alignment of buttress amino acid sequences. Deletion is highlighted. **c**, top: Normalized histograms of primary forward and backward unbinding forces for the Δ BUT-Dyn1_{331kDa} mutant (top), with mean values noted (95% CIs [0.6, 0.8] and [0.7, 0.8] pN, estimated by bootstrapping 4,000 samples) (source data are provided as a Source Data file). **c**, bottom: Unbinding rate vs. force derived from the data above. The shaded areas are 95% CIs for the mean rates, estimated by bootstrapping. The depicted zero-load unbinding rate of 2.67 ± 0.05 (characteristic rate \pm SEM) (red circle) represents the inverse of the time constant obtained from the analysis of the experimental CDF of the MT-bound lifetimes measured via TIRF microscopy (Supplementary Fig. 2e) (the 95% CIs of the measured unbinding rate (lower limit, 2.58/s; upper limit, 2.77/s) are not shown as they are shorter than the height of the symbol)

the buttress's interactions with the stalk helices. Alternatively, tension applied to the linker-AAA5 interface could induce a buttress conformation that prevents transition into the β -registration. To distinguish between these possibilities, we determined the unbinding-force behavior of the AAA3 E/Q mutant in the presence of 1 mM ATP while using a C-terminal GFP for the coupling to trapping beads in order to prevent tension from acting directly on the linker (AAA3 E/Q Dyn1_{331kDa} CT-GFP). We have previously shown that this mutant shows a strong and anisotropic unbinding behavior in the presence of ATP similar to the WT MD in the apo state³². In addition, Bhabha et al. showed that blocking nucleotide hydrolysis at AAA3 prevents the linker from moving from the post-powerstroke to the pre-powerstroke conformation²³. Thus, we hypothesized that AAA5-linker interactions, as a result of the post-powerstroke linker conformation, prevent the AAA3 E/Q mutant from showing the weak MT-binding seen in the WT MD under C-terminally applied tension in the presence of ATP³². To test this, we induced a F3446E mutation in AAA5 in the AAA3 E/Q Dyn1_{331kDa} CT-GFP mutant to prevent functional stalk-AAA5 interactions. As hypothesized, this mutant binds MTs weakly in both directions ($p_{ks} = 0.82$, forward vs. backward, Fig. 6c) and shows similar mean unbinding forces as the Dyn1_{331kDa} motor

construct with the equivalent F3446E point mutation ($p_m = 0.25$ (forward) and $p_m = 0.1$ (backward) [F3446E-AAA3 E/Q CT-GFP ATP vs. F3446E-Dyn1_{331kDa} apo]; Fig. 6b–c). In conclusion, linker-AAA5 interactions in the absence of linker-applied tension are sufficient to block the tension-induced transition into the β -registration.

Dynein motility requires buttress-stalk interactions. Buttress truncation uncouples ATPase activity and MT binding in the absence of load¹⁴ and also prevents tension-induced transition from weak to strong MT binding (Figs. 2f and 5c), suggesting that the buttress is essential for motility. To test this prediction, we developed an in vitro approach to homodimerize (or heterodimerize) our single-headed dyneins using an antibody against the N-terminal GFP of the motors (see Methods). While antibody-dimerized WT Dyn1_{331kDa} is highly processive and as fast as GST-dimerized Dyn1_{331kDa}³⁷ (Fig. 7a), antibody-dimerized Δ BUT-Dyn1_{331kDa} (i.e., with the distal part of the buttress deleted (Δ BUT, Fig. 5b)) only exhibits brief, non-motile MT interactions (as does Δ BUT-Dyn1_{471kDa}, a homodimeric full-length dynein bearing the same buttress truncation, see Supplementary Fig. 9a) as revealed by kymograph analysis (Fig. 7c, left).

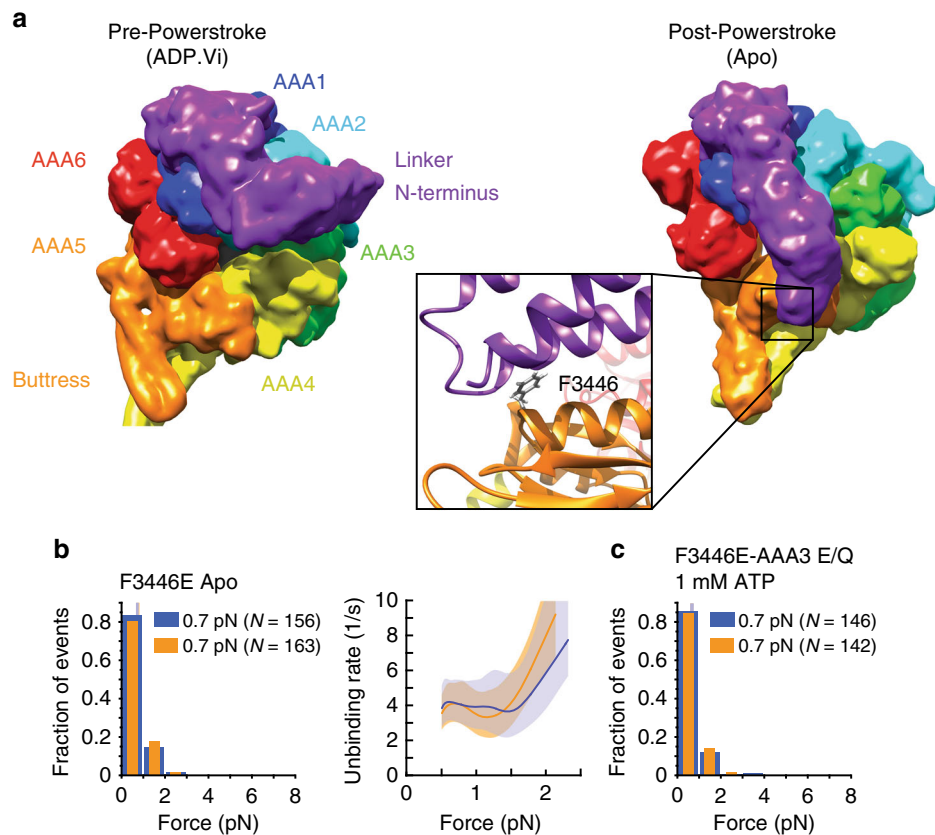


Fig. 6 Docking/undocking of the linker to and from AAA5 controls tension-induced reconfiguration of the stalk. **a** Structures of the dynein MD in the pre-powerstroke (ADP.Vi, *Homo sapiens* cytoplasmic dynein-2; PDB entry 4RH7⁴⁷) and post-powerstroke (Apo, *S. cerevisiae* dynein; PDB entry 4W8F¹³) states. In the pre-powerstroke state, the linker is bent and close to AAA2 (left), while in the post-powerstroke state, the linker is straight and docked on AAA5 (right). (inset) Interactions between hydrophobic residues of the linker and the highly conserved F3446 of AAA5 facilitate the docking of the linker N-terminus on AAA5¹³ (PDB entry 4W8F²³). **b**, left: Normalized histograms of primary forward and backward unbinding forces for the F3446E-Dyn_{1331kDa} mutant, with mean values noted (95% CIs [0.7, 0.8] and [0.7, 0.8] pN, estimated by bootstrapping 4000 samples). **b**, right: Unbinding rate vs. force derived from the data on the left. The shaded areas are 95% CIs for the mean rates, estimated by bootstrapping. **c** As in **b**, but for the F3446E-AAA3 E/Q Dyn_{1331kDa} CT-GFP mutant and 1 mM ATP (95% CIs [0.6, 0.8] and [0.6, 0.7] pN). Source data are provided as a Source Data file

In a recent study, Cleary et al. demonstrated that an active dynein head (capable of performing an ATP-dependent linker swing) fused to an inactive MT tether moves processively along MTs if the MT affinity of the tether is sufficiently high³³. A dynein head fused to a MT tether consisting of the SRS-stalk-MTBD construct in the low-affinity β -registration was incapable of processive motion, while the high-affinity α -registration exhibited a two-fold higher processivity than the dimeric WT motor, albeit at a threefold lower speed than the WT motor³³ (note that while this high affinity α -registration has a higher MT-binding strength than the SRS- β stalk-MTBD construct (Fig. 4b, d), the stalk registration of this construct is distinct from the true α -registration, which is only assumed when the stalk helices are cross-linked in the α -registration). Thus, a strongly bound leading head is capable of dragging an inactive, strongly MT-bound MTBD forward (at the cost of speed) by changing the linker conformation. As the previous work on *Dictyostelium* dynein has shown that a buttress truncation does not completely abolish ATP-dependent movements of the linker¹⁴, we wanted to test whether the weak MT-binding strength of the buttress-truncated dynein head (Fig. 5c) prevents antibody-dimerized Δ BUT-Dyn_{1331kDa} from moving processively. To test this, we increased the ionic interaction between the MTBD and MT by mutating the highly conserved glutamic acid E3197 in H6 of the MTBD to a basic amino acid (K)

(Fig. 1c). This mutation significantly increases the processivity of *S. cerevisiae* dynein³⁰, suggesting stronger MT binding by the MTBD³³. However, while the point mutation increased the time the antibody-dimerized Δ BUT-E3197K-Dyn_{1331kDa} motors interacted with MTs (Fig. 7c and Supplementary Fig. 9b), the motors were still non-processive.

It is possible that the buttress deletion not only prevents registration changes of the stalk helices but that the absence of stalk-buttress interactions also causes conformational changes at the base of the buttress and possibly within AAA5 or the entire AAA ring that negatively impact dynein's motion-generating linker conformational change. To test this possibility, we first determined whether dynein is capable of moving processively along MTs when its stalk helices are fixed in the weak, intermediate or strong MT-bound helix registrations with a buttress capable of interacting with the stalk. Intriguingly, while both the antibody-dimerized Dyn_{1331kDa}- β CL and Dyn_{1331kDa}- γ CL mutants show only brief, non-motile MT interactions (Fig. 7d), Dyn_{1331kDa}- α CL exhibits highly processive motion albeit at a significantly lower speed than the antibody-dimerized Dyn_{1331kDa} motor (Fig. 7a, b). In contrast, in the presence of TCEP, all three mutant motors are as processive and fast as antibody-dimerized WT Dyn_{1331kDa} (Fig. 7b, bottom right and Supplementary Fig. 10a, b), demonstrating not only the reversibility of the cross-linking of the stalk helices but also that

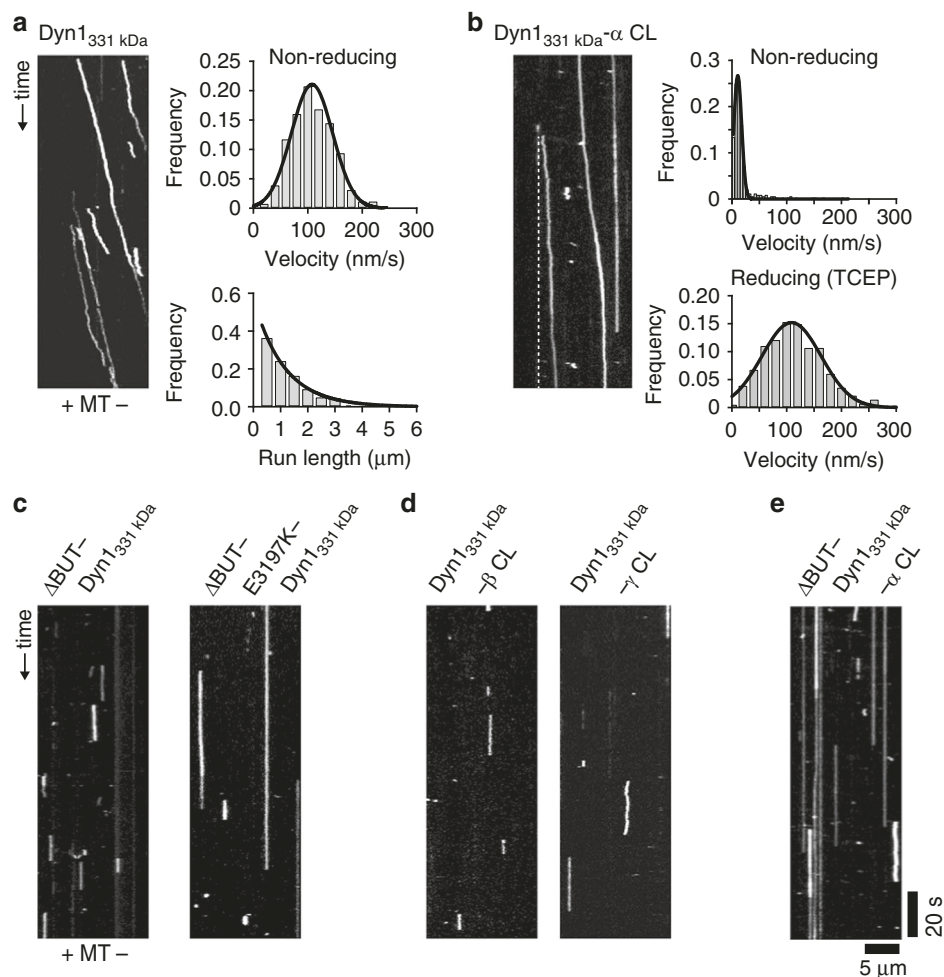


Fig. 7 Stalk-buttress interactions are essential for dynein motion. **a** Antibody-based dimerization of WT Dyn_{1331kDa} results in processive runs under non-reducing conditions in the single-molecule TIRF assay at 1 mM ATP (left). Diagonal lines in the kymograph represent dimerized dynein molecules that are moving over time. Fitting the histogram of measured velocities with a Gaussian (black line, top right), results in a mean velocity of 108 ± 2 nm/s (\pm SEM; $N = 255$). A histogram of measured run lengths fit with an exponential function (black line, bottom right) yields a characteristic run length of 1.1 ± 0.1 μ m (\pm SEM; $N = 255$) (source data are provided as a Source Data file). **b** In contrast to the motors with the cross-linked β and γ stalk registrations (**d**), Dyn_{1331kDa}- α CL shows highly processive motion (left) (the dashed white line serves as a visual guide to help recognize the slow moving Dyn_{1331kDa}- α CL mutant) under non-reducing conditions. Fitting the histogram of measured velocities with a Gaussian (black line, top right), yields a mean velocity of 10.6 ± 0.4 nm/s (\pm SEM; $N = 336$) (top right). Performing the experiments in the presence of 2 mM TCEP increases the velocity to 109 ± 3 nm/s (\pm SEM; $N = 281$) (bottom right), demonstrating the reversibility of the cross-linking of the stalk helices (source data are provided as a Source Data file). **c** Kymograph analysis of the antibody-dimerized motors with the buttress truncations reveals that neither Δ BUT1-Dyn_{1331kDa} (left) nor Δ BUT-E3197K-Dyn_{1331kDa} (right) move along MTs. Instead, both motors show non-motile MT interactions (increasing the ionic interaction strength between MTs and the MTBD via the E3197K mutation increases the lifetime of the non-motile binding events, see Supplementary Fig. 9b). **d** Kymograph analysis of the antibody-dimerized WT Dyn_{1331kDa}- β CL and WT Dyn_{1331kDa}- γ CL motors reveals only non-motile MT interactions. **e** Preventing stalk-buttress interactions in the Δ BUT-Dyn_{1331kDa}- α CL motor results in non-motile interactions, demonstrating the importance of stalk-buttress interactions. The depicted scale bars are the same for all kymographs shown in this figure

all three motors are as enzymatically active under non-cross-linked conditions as WT Dyn_{1331kDa}. Antibody-dimerized WT Dyn_{1331kDa} on the other hand, shows the same motility behavior under cross-linking (Fig. 7a) or non-cross-linking conditions (Supplementary Fig. 10b). Together, these results suggest that the Dyn_{1331kDa}- α CL motor is capable of generating a motility-driving linker conformational change even when its stalk helices are cross-linked via the inserted paired cysteines. In contrast, antibody-dimerized Δ BUT-Dyn_{1331kDa}- α CL motors without functional buttress-stalk interactions only show brief, non-motile MT interactions (Fig. 7e). Our data suggest that the disruption of stalk-buttress interactions results in conformational changes within AAA5 that impair motion-generating

conformational changes of the linker, possibly by preventing functional interactions between the linker and AAA5 during dynein's post-powerstroke state.

Discussion

While previous studies demonstrated that dynein's MT binding strength responds anisotropically to tension^{32–35}, the underlying mechanism was unclear. Here, by combining mutagenesis, structure-function and chemical cross-linking with single-molecule optical tweezers, we demonstrate that dynein's anisotropic response to tension is not intrinsic to the MTBD alone, but is controlled by dynein's AAA ring and its three appendages, the

stalk, buttress, and linker. These elements work together to control the MT-binding strength of the MTBD in a tension direction-dependent manner.

In the absence of stalk-buttress interactions, MT binding is weak in both directions and indistinguishable from the MT-binding strength of a motor with the stalk helices cross-linked in the β -registration. This suggests that the stalk helices assume a β -registration in the relaxed state of the stalk coiled-coil, in agreement with biochemical and structural studies^{14,27,28}. In contrast, backward load induces strong MT binding of the WT motor in the absence of nucleotides, similar to the MT-binding strength of a motor with the stalk helices cross-linked in the α -registration. Thus, backward tension applied to the MD induces the α -registration of the stalk.

Our data also reveal that forward tension alone is not sufficient to induce the β -registration in the WT MD in the absence of nucleotides and instead induces a stalk helix registration that is distinct from the known β - and α -registrations. This registration results in an intermediate MT-binding strength under forward load (Fig. 2e). As we showed previously³², the transition into dynein's weak MT-binding state under linker-applied forward load occurs only if AAA1 and AAA3 are bound to ATP (when tension is applied via dynein's C-terminus, AAA3 needs to be in the post-hydrolysis state^{32,46}). This suggests that tension-induced transition into the β stalk registration requires nucleotide-induced structural changes in the AAA ring.

What stalk helix registration does dynein assume under forward load in the apo state if not the β -registration? The crystal structures solved in dynein's post-powerstroke ADP state (*Dictyostelium* dynein 1)¹⁴ and pre-powerstroke ADP.Vi state (human dynein 2)⁴⁷ suggest that dynein's stalk helices transition between the α - and β -registrations. Locking the stalk helix registration in between the α - and β -registrations indeed results in MT-binding strengths under forward and backward load that are statistically indistinguishable from the MT-binding strength of the WT motor under forward load in the apo state (Figs. 2e and 3d). This intermediate stalk helix registration, which we term the γ -registration, is likely near the stalk registration assumed in dynein's rear head when ADP is still bound to AAA1 as well as after ADP release: the mean unbinding forces under forward load are the same for WT dynein in the apo state and for the dynein AAA3 K/A mutant with ADP bound to AAA1 and AAA4, no nucleotide bound to AAA3, and ATP firmly bound to AAA2^{13,32}. This finding suggests that dynein assumes at least three different stalk registrations during the mechanochemical stepping cycle and underlines the intricate nature of the pathway used to communicate bidirectionally between dynein's AAA ring and its MTBD.

Our buttress truncation experiment demonstrates that functional stalk-buttress interactions are necessary to induce the α -registration of the stalk helices under backward load. Whether tension applied to the linker results in a pulling or pushing of the buttress on the stalk helices remains to be shown. However, since the absence of functional buttress-stalk interactions results in the weak MT binding β -registration independent of the direction of tension, it is clear that the tension-induced transition into the α -registration requires a buttress-induced change from the β - to the α -registration. While dynamic changes in the registry of the stalk helices of dynein could occur so that different registries are dynamically sampled, with one registry favored over the others, our data suggest that the buttress together with applied tension highly stabilizes distinct registries depending on the direction of applied tension and nucleotide state.

The dynein mutant F3446E-Dyn1₃₃₁ kDa shows MT-binding strengths statistically indistinguishable from the motor with the stalk helices cross-linked in the β -registration. Thus, linker-AAA5

docking is required for the tension-induced α -registration under backward load and the γ -registration under forward load, while the undocking of the linker from AAA5 is required for the transition into the β -registration. Since the buttress truncation mutant and the cross-linked β -registration mutant have statistically indistinguishable MT-binding strengths, linker docking appears to control the conformational changes of the buttress. A tension-induced, strong MT-binding α -registration with the linker docked to AAA5 in its post-powerstroke conformation is consistent with the load-bearing requirements of the front head in the post-powerstroke state. In contrast, ATP-induced undocking of the linker from AAA5 would facilitate the detachment of dynein's rear head via a transition into the weak-MT binding β -registration under forward-directed (intermolecular) tension. Thus, ATP binding to AAA1 accelerates MT detachment via a transition into the β -registration initiated by the undocking of the linker.

We note that the requirement of AAA5-linker interactions for the tension-induced α -registration appears to conflict with the α -registration observed in the crystal structure of *Dictyostelium* dynein solved in the presence of ADP (i.e., in the presumed post-powerstroke state). In the crystal structure, the linker lies close to AAA4 rather than AAA5¹⁴. It is possible that the linker and/or stalk conformation is different when dynein is bound to MTs in the presence of ADP or that the linker and/or stalk helices assume different conformations in the crystal structure versus in solution. Indeed, we previously showed that ADP binding to AAA3 induces a weak MT-binding state of dynein under load³², which is inconsistent with the α -registration in the dynein crystal soaked with ADP (i.e., with an ADP molecule bound to AAA3). Furthermore, a recent cryoEM study has demonstrated that with ADP bound to AAA3, dynein assumes the low-affinity stalk registration in its auto-inhibited conformation known as the phi-particle⁴⁸. Thus, it is possible that the interactions between the MDs and/or the linkers as seen in the phi-particle have similar effects on the stalk helix registration as linker-applied tension. Solving the crystal structure of dynein bearing an AAA3 K/A mutation in the presence of ADP could help to resolve these apparent discrepancies.

Previous work has shown that the prevention of buttress-stalk interactions uncouples dynein's ATPase activity from MT binding and results in weak MT-binding^{14,31}. However, how this behavior affects the motion of two-headed dynein was undetermined. Here, we show that the two-headed motor with a buttress truncation is immotile, even if the MT-binding strength is increased with a point mutation in the MTBD. Since a single dynein head capable of a power stroke is able to move processively when linked to a strong MT-binding tether³³, we would have expected that our two-headed dynein motor with the buttress truncation and the increased MT-binding strength would be capable of processive motion—as long as the MD could perform a power stroke. Previous FRET studies on *Dictyostelium* dynein demonstrated that linker movements still occur in the absence of stalk-buttress interactions¹⁴, suggesting that dynein may still be capable of a power stroke without the buttress. However, our observations suggest that dynein is unable to generate a linker conformational change capable of powering unidirectional motion in the absence of buttress-stalk interactions. Our observation that an antibody-dimerized dynein with the stalk helices cross-linked in the α -registration is capable of generating processive motion (owing to its residual anisotropic MT-binding strength, Fig. 3b) only if the buttress can interact with the stalk further supports the conclusion that functional buttress-stalk interactions are not only required for the communication between the AAA ring and MTBD but also for an ATP-induced, motion-generating power stroke of the linker. As our data reveal

that linker interactions with AAA5 control the tension-induced and buttress-dependent registry changes of the stalk helices, it is possible that a lack of stalk-buttress interactions alters the base of the buttress and possibly the conformation of AAA5, thereby preventing functional interactions between the linker and AAA5. This could result in the weak MT-binding β -registration in dynein's post-powerstroke state and possible impairment of the post-powerstroke conformation of the linker.

Our findings support a revision of the current consensus model for dynein motion. In the current model, ATP binding to AAA1 of dynein's rear head causes head dissociation from the MT, followed by the priming stroke of the linker in the detached head^{3,45,49}. Our data suggest that rear head detachment occurs after the ATP-induced undocking of the linker from AAA5, an event required for the transition into the weak MT-binding β -registration. Thus, the priming stroke likely already starts while the rear head is still bound to the MT, rather than after MT dissociation. In addition, our data reveal that linker docking to AAA5 is required for the transition into the α -registration in dynein's front head. Thus, in contrast to models that postulate that dynein's front head assumes a strong MT-binding state before the power stroke occurs⁴⁹, our data suggest that the power stroke induces the strong MT-binding state of the leading head.

On the basis of our findings here and in previous work³², we propose the following model for dynein's mechanochemical cycle, taking into account the nucleotide states of AAA1 and AAA3 (Fig. 8). Because AAA2 likely remains bound to ATP throughout the mechanochemical cycle^{13,14}, it is unlikely to play an active regulatory role, and while AAA4 likely has a regulatory function^{50,51}, the significance of its nucleotide state in the overall mechanochemical cycle is undetermined. We start with ATP binding to AAA1 of dynein's trailing head (Fig. 8, step 1), which causes linker undocking from AAA5 and the subsequent transition into the weak MT-binding β -registration (Fig. 8, step 2). After detachment from the MT (Fig. 8, step 3), the free head undergoes a forward movement driven by the priming stroke of its linker (Fig. 8, step 4). The priming stroke occurs while ATP is bound to AAA1 and with AAA3 likely in the ADP.Pi transition state or bound to ADP, since ATP binding to AAA1 induces MT release only if AAA3 is in the post-hydrolysis state^{32,46} (if the linker is under tension, ATP binding to AAA3 is enough to open the gate³²).

Following ATP hydrolysis, the tethered head then binds to a new binding site on the MT (Fig. 8, step 5). It is under debate whether phosphate releases before MT binding or whether MT binding stimulates phosphate release^{14,24}. On the basis of our data, initial binding is likely via a weak interaction. MT binding then causes the transition from the 'high-energy ADP state' to the 'low-energy ADP state'^{24,39,52}, which is accompanied by the power stroke²² (Fig. 8, step 6). Binding of the linker N-terminus to AAA5 in the post-powerstroke state then allows the tension-induced transition into the strong MT-binding α -registration, a state capable of bearing load. We note that the crystal structure solved in the presence of ADP suggests that the force-bearing head in its post-powerstroke state assumes the α -registration¹⁴. However, our previous data show that ADP binding to AAA3 induces a weak MT-binding state under backward load³², suggesting that AAA3 may not contain ADP following the power-stroke. Recent work by Dewitt et al. suggests that AAA3 hydrolyzes ATP an order of magnitude slower than AAA1⁴⁶ under unloaded conditions, suggesting that AAA3 activity is not synchronized with the activity of AAA1. In addition, we previously showed that MT-binding strength is stronger under backward load when ADP is bound to AAA1³². We therefore suggest that in the post-powerstroke state of the force-bearing leading head, AAA1 is bound to ADP ('low-energy ADP state')

and AAA3 is in the ADP.Pi transition state. However, it remains to be shown whether a dynein head with ADP bound to AAA1 and AAA3 in the ADP.Pi transition state binds MTs strongly enough under backward load to remain attached. In addition, it is possible that AAA3 activity is synchronized with the activity of AAA1 under load, in which case AAA3 may assume a nucleotide-free state, which would result in strong MT binding under backward load when AAA1 is bound to ADP³². Thus, AAA3 may be ADP bound only at appropriate points in the cycle, such as when the head is detached from the MT or when ATP binds to the rear head AAA1, thereby assisting in MT release³².

It is possible that the power stroke of the MT-bound leading head increases intramolecular tension if the MT-bound rear head still has ADP bound to AAA1, or if ADP is released so that AAA1 assumes the apo state. This transition could induce the γ -registration, leading to an intermediate MT-binding strength, or directly contribute to forward movement if ATP binds AAA1 in time to induce rear head detachment. The latter event, which only occurs when ATP is bound to AAA3 (if the linker is under tension³²) or when AAA3 is in the post-hydrolysis state (ADP.Pi or ADP)⁴⁶, allows the rear head to transition into the weak MT-binding state by assuming the β -registration. With the ATP-induced rear head detachment, a new mechanochemical cycle begins.

In summary, our findings demonstrate the complex nature of dynein's force- and motion-generating mechanism, in which dynein's AAA+ MD and its three appendages, the stalk, buttress, and linker, work together to regulate the cyclic weak and strong MT interactions of the MTBDs. This regulation ensures that one MD holds tightly to the MT while the other detaches and advances. In the case of mammalian dynein, this mechanism may ensure processive dynein stepping following its activation by its largest cofactor, dynactin, which, together with a coiled-coil containing cargo adaptor (such as BICD2), converts mammalian dynein from a diffusive⁵³/weakly processive⁵⁴ motor to an ultraprocessive motor^{55,56}, possibly by reorienting dynein's MDs^{48,57,58}. Future studies will be needed to determine which orientations and stalk registrations dynein's MDs assume when complexed with dynactin and how teams of dynein motors are coordinated when recruited to dynactin via the cargo adaptors BICDR1 and HOOK3, which have been reported to predominantly bind two dynein motors^{59,60}. Finally, insights are needed into whether the activities of AAA1 and AAA3 are coordinated under load.

Methods

Generation of yeast strains. Mutant yeast strains (listed in Supplementary Table 1) were generated using two-step selection methods (SC/URA- and 5-FOA)⁶¹. PCR primers were designed using the PrimerQuest tool from Integrated DNA Technologies, and the PCR protocols for KOD Hot Start DNA polymerase (EMD Millipore) were followed (see Supplementary Table 2 for the list of primers used) to generate DNA fragments. Yeast transformation was performed using either the standard yeast transformation method (based on the LiAc/ss carrier DNA/PEG protocol⁶²) or the Frozen-EZ Yeast Transformation II kit from Zymo Research, with SC/URA- (synthetic media with uracil-dropout amino acid mix) and SC/5-FOA (5-fluorouracil) as selective agents. All newly engineered and mutated yeast strains were confirmed by PCR and sequencing.

Generation of plasmids for SRS-stalk-MTBD constructs. Standard molecular cloning methods were used to create chimeric constructs of monomeric *Thermus thermophilus* seryl-tRNA synthetase (SRS) fused to the stalk and MTBD of yeast dynein using SRS85:82, a construct with the near full-length mouse stalk and MTBD fused to the coiled-coil base of SRS in the α -registry^{27,33} as a template. Genomic yeast DNA was amplified to generate DNA fragments of the dynein stalk and MTBD. PCR products were then stitched with partial SRS sequences to enable insertion between the restriction enzyme sites, SalI and PstI, of the original vector (see Supplementary Table 2 for the list of primers used). Single point mutations in the SRS chimeras were generated using the Q5 site-directed mutagenesis kit from NEB. High efficiency 5- α competent *E. coli* cells (NEB) were used for transformation and plasmid amplification. Single colonies were inoculated in 3 mL of

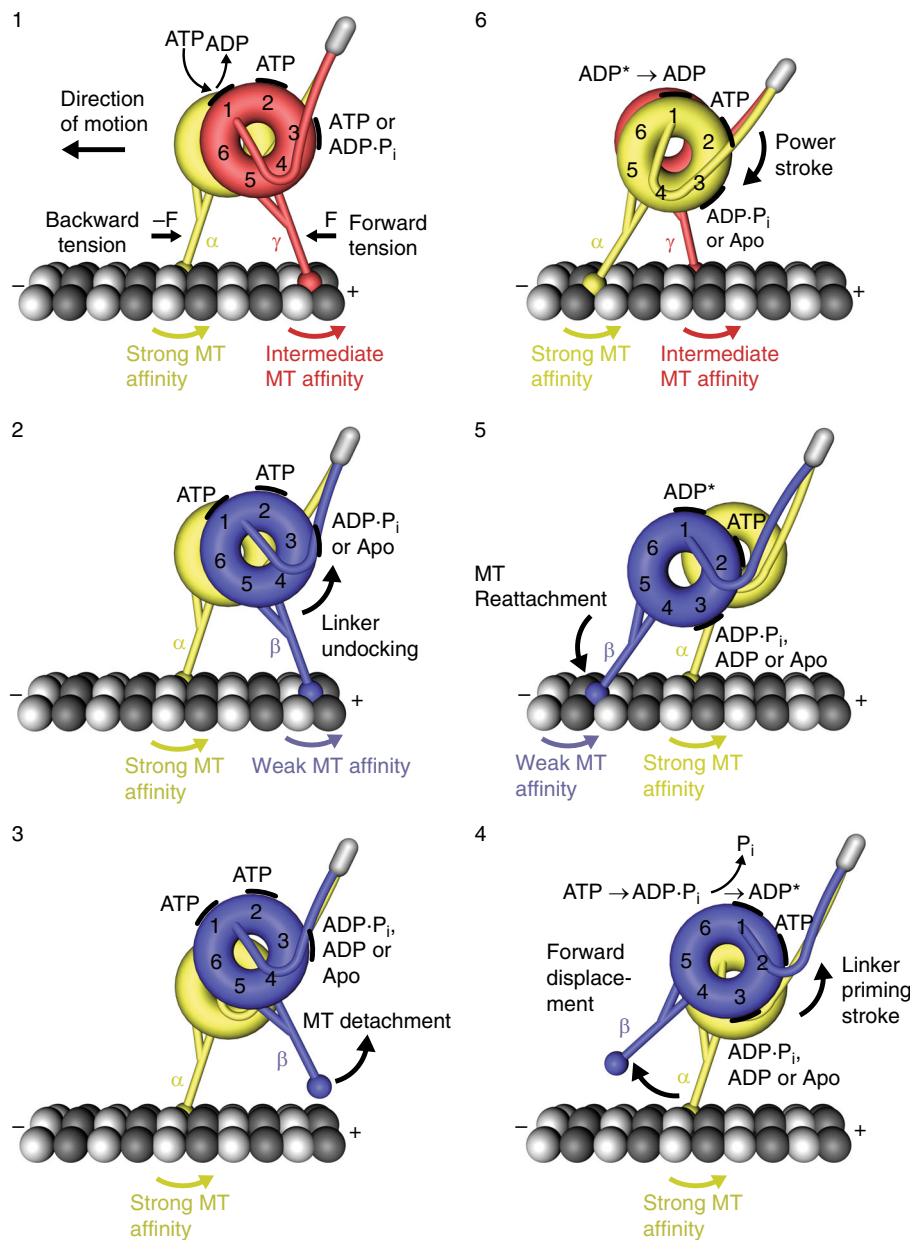


Fig. 8 Model for the mechanochemical cycle of dynein. Following ADP release from AAA1, ATP binding (step 1) causes the undocking of the linker from AAA5 and the subsequent transition from the γ -registry of the stalk helices with intermediate weak MT-affinity to the weakly MT-binding β -registry (step 2). After the detachment of the rear head (step 3), which occurs when AAA3 is in the ADP• P_i transition state or bound to ADP, the ‘recocking’ of the linker (priming stroke) displaces the detached head forward to a new front MT-binding site while the MT-attached head bears the load (step 4). Following ATP hydrolysis and P_i release from AAA1 (step 4), rebinding to the MT in the weakly MT-binding β -registry (step 5) causes the transition from the ‘high-energy ADP* state’ to the ‘low-energy ADP state’, which generates a linker swing (powerstroke), resulting in the docking of the linker to AAA5 and the transition into the strong MT-binding α -registry of the stalk helices (step 6). A prerequisite for the strong binding state is that AAA3 is not bound to ADP, suggesting that AAA3 is still in the ADP• P_i state or nucleotide free. The MT minus-end-directed linker swing generates the forward movement of dynein’s center of mass and the attached load

terrific broth (TB) with 30 μ g/mL of kanamycin and grown overnight shaking at 37 °C. Plasmids (listed in Supplementary Table 1) were purified using the PureYield plasmid miniprep kit from Promega and verified by standard sequencing.

Yeast growth and yeast dynein expression. Single-headed dynein constructs (based on tail-truncated dynein, Dyn1_{331kDa}) were expressed behind the inducible galactose promoter (GAL1-GAL10), while two-headed full-length dynein constructs (based on Dyn1_{471kDa}) were expressed behind the native promoter⁶¹. Yeast growth was done at 30 °C with shaking. For single-headed dynein, a single yeast colony was inoculated in 5 mL of 2 × YPD (20 g/L yeast extract, 40 g/L peptone, 4% (w/v) dextrose) overnight. Pre-cultures were then inoculated in 50 mL of YPR (2% (w/v) raffinose) for 8 h. Expression of dynein was induced by transferring the YPR

culture into 2 L of 2 × YPG (4% (w/v) galactose). Cultures were then grown to a final OD₆₀₀ between 1.5 and 2.5 (~16 h). To express full-length dynein, yeast cells were grown similarly to the growth for the expression of single-headed dynein, except that only 2 × YPD was used throughout the growth, and cells were grown to a final OD₆₀₀ of ~0.8. Cells were then harvested via centrifugation at 1000 × g for 3 min, and washed once with ddH₂O. Finally, pellets were resuspended in 0.2 volumes ddH₂O and flash-frozen in liquid nitrogen as small droplets, and stored in 50-mL conical tubes at -80 °C until further use.

Expression of SRS-stalk-MTBD constructs. For the expression of the SRS chimeras, plasmids encoding the SRS chimeric constructs were transformed into Rosetta (DE3) pLysS competent *E. coli* cells (Novagen) for protein expression.

E. coli growth was done in the presence of 15 µg/mL kanamycin and 17 µg/mL chloramphenicol at 37 °C with shaking unless specified otherwise. For each construct, a single colony was inoculated in 3 mL terrific broth overnight and then diluted into 100 mL terrific broth at a starting OD₅₉₅ of ~0.1 to create a pre-culture. Following a ~2-hour growth until OD₅₉₅ reached ~0.6–1, the pre-culture was added to 900 mL terrific broth. The full culture was grown at 37 °C until OD₅₉₅ reached ~0.8 and then cooled on the ice below 18 °C. Protein expression was induced by addition of 0.1 mM IPTG (isopropyl β-D-1-thiogalactopyranoside), followed by incubation at 18 °C with shaking for 16 h. The cells were then pelleted at 3000 × g for 5 min, the supernatant was discarded and the residual liquid was used to resuspend the cells. The cell slurry was then transferred to a 50-mL conical tube and stored at –80 °C until further use.

Yeast dynein purification. All dynein constructs have an N-terminal ZZ-tag (synthetic two-domain IgG-binding sites based on staphylococcal protein A⁶⁵) for binding to beads coated with IgG (immunoglobulin G) during affinity purification, followed by an enhanced TEV (tobacco etch virus) protease cleavage sequence, a GFP (yEGFP3, a yeast-codon optimized enhanced green fluorescence protein, GFPmut3⁶⁴), and a hemagglutinin (HA) tag (not employed in this work). The construct for full-length dynein, Dyn1_{471kDa}, has an additional Halo-Tag between the GFP and HA tags. The SNAP-tagged single-head dyneins based on Dyn1_{331kDa} have an additional SNAPf-tag between the GFP and HA tags. Protein purification was done at 4 °C unless specified otherwise. For each purification, the stored frozen cell droplets were pulverized using a kitchen coffee grinder pre-chilled using liquid nitrogen, followed by addition of 0.25 volumes of 4× lysis buffer (1× lysis buffer: 30 mM HEPES, 50 mM KAc, 2 mM Mg(Ac)₂, 1 mM EGTA, 10% glycerol, 1 mM DTT, 0.1 mM Mg-ATP, 0.5 mM Pefabloc, 10 ng/mL Leupeptin, 10 ng/mL Pepstatin A, 0.2% v/v Triton X-100, pH 7.2) to reach a final concentration of 1× lysis buffer. The cell lysate was then cleared via ultracentrifugation at 290,000 × g for 30 min. Next, 250 µL of IgG sepharose 6 fast flow beads (GE Healthcare) was added to the supernatant. The solution was then incubated for 1 hr while rotating. The dynein-bound IgG beads were then washed with 20 mL of 1× lysis buffer. To fluorescently label native dynein (or single-head dynein) with TMR (tetramethylrhodamine), TMR-conjugated Halo-tag ligand (Promega) (or SNAP-Cell® TMR-star ligand (NEB)) was added to the beads to a final concentration of 10 µM, and incubated with the beads at room temperature for 10 min. Afterwards, the beads were washed with 10 mL of 1× TEV protease cleavage buffer (30 mM HEPES, 150 mM KAc, 2 mM Mg(Ac)₂, 1 mM EGTA, 10% glycerol, 0.1 mM Mg-ATP, 0.5 mM Pefabloc, 0.1% v/v Triton X-100, pH 7.2). The beads were then resuspended in an equal volume of the cleavage buffer and 40 units of AcTEV protease (ThermoFisher Scientific) was added. The mixture was nutated for 2 h, resulting in cleavage of dynein from IgG beads. Beads were then sedimented by centrifugation, and the dynein-containing supernatant was flash-frozen in 50 µL aliquots in liquid nitrogen (TEV-released dynein). The aliquots were finally stored at –80 °C until further usage.

Microtubule binding and release purification of dynein. To further purify dynein and to remove dynein aggregates, we performed a MT binding and release assay for each dynein construct that was responsive to ATP. To 50 µL of TEV-released dynein, 10 µL of 5 mg/mL paclitaxel-stabilized MTs were added in the presence of 20 µM paclitaxel (Sigma). The solution was then layered onto a 100 µL sucrose cushion (30 mM HEPES, 200 mM KCl, 2 mM MgCl₂, 10% glycerol, 25% w/v sucrose, 20 µM paclitaxel, pH 7.4) and centrifuged at 25 °C for 10 min at 60,000 × g. After the supernatant and cushion were gently removed without disturbing the pellet, the MT pellet was gently rinsed with 100 µL wash buffer (30 mM HEPES, 150 mM KCl, 2 mM MgCl₂, 10% glycerol, pH 7.2; EGTA was not added due to its interference with oxidation by copper phenanthroline) and resuspended in 52 µL of wash buffer with 6 mM Mg-ATP. The solution was then centrifuged again for 5 min at 60,000 × g. Finally, the dynein-containing supernatant was aliquoted into 2 µL volumes, flash frozen in liquid nitrogen and stored at –80 °C until further use. For constructs that are insensitive to ATP, 2 µL of 5 mg/mL paclitaxel-stabilized MTs were added to 50 µL of TEV-released dynein in the presence of 20 µM paclitaxel and 6 mM Mg-ATP, and the sample was centrifuged for 5 min at 60,000 × g at room temperature to remove dynein aggregates.

Purification of SRS constructs. An *E. coli* cell pellet was thawed at room temperature and an equal amount (1 mL per 1 g of cell wet weight) of 2× lysis buffer (1× lysis buffer: 50 mM Tris, 200 mM NaCl, 1 mM EGTA, 10% glycerol, 1 mM PMSF, 1 mM β-ME (β-mercaptoethanol), pH 7.6; β-ME was not added for the SRS mutants with the paired cysteines in the stalk helices) was added. After resuspension of the pellet, the cells were lysed by sonication at 4 °C. The lysate was then cleared by centrifugation at 400,000 × g for 10 min. 200 µL Ni-NTA resin (Qiagen) was added to the cleared lysate and imidazole (2 M, pH 8) was added to a final concentration of 10 mM. The solution was nutated for 1 h at 4 °C. The Ni-NTA resin was then washed with 10 mL of wash buffer (the same as 1× lysis buffer but with 20 mM imidazole), and the protein was eluted from the Ni-NTA resin with elution buffer (the same as 1× lysis buffer but with 250 mM imidazole and without PMSF). The protein solution was aliquoted in 50 µL volumes and flash-frozen in liquid nitrogen. To remove imidazole, one aliquot of the eluted protein was

exchanged into storage buffer (the same as elution buffer but without imidazole) using a Zeba™ Spin Desalting Column (ThermoFisher Scientific). The flow-through was aliquoted into 2 µL volumes. Finally, the aliquots were stored at –80 °C until further use.

Preparation of coverslips for MT immobilization. Using forceps, coverslips (18 × 18 × 0.170 mm, Zeiss) were placed into a porcelain coverslip rack, submerged in HNO₃ (25% v/v) for 10 min, rinsed with ddH₂O, and then submerged in NaOH (2 M) for 2 min, followed by extensive rinsing with ddH₂O. The coverslip rack was placed onto a heating block set at 90 °C to air-dry the cleaned coverslips for 10–20 min and then stored in a vacuum desiccator. The slide chamber was assembled as described previously⁶⁵. For MT immobilization, 10 µL of 5 mg/ml biotinylated α-casein was flown into the slide chamber and incubated for 10 min. Then 3 × 20 µL of blocking buffer (80 mM PIPES, 2 mM MgCl₂, 1 mM EGTA, 1% Pluronic F-127, 1 mg/ml α-casein, 20 µM Taxol) was used to wash the chamber, and incubated for 1 h to fully block the glass surface. Following the blocking step, the solution inside the chamber was completely removed, and 12 µL of 1 mg/ml streptavidin was flown into the chamber and incubated for 10 min. The chamber was then washed with 3 × 20 µL blocking buffer.

Polymerization of polarity-marked MTs. The direction of unbinding forces was confirmed using polarity-marked MTs with bright, densely fluorescently labeled minus ends. To prepare polarity-marked MTs, 0.5 µL of 2 mg/mL TMR-labeled tubulin and 0.5 µL of 1 mg/mL biotin-labeled tubulin (Cytoskeleton) with 1 mM Mg-GTP were combined and incubated at 37 °C for 5 min to generate bright MT seeds. Next, 5 µL of 1 mg/mL unlabeled tubulin, 0.5 µL of 0.1 mg/mL TMR-labeled tubulin, and 0.5 µL of 0.1 mg/mL biotin-labeled tubulin with 1 mM Mg-GTP was added to the seeds. The mixture was incubated at 37 °C for 15 min. 0.7 µL of 0.2 mM paclitaxel in DMSO was then added to the mixture, and free tubulin was removed by centrifuging through a 60 µL glycerol cushion (80 mM PIPES, 2 mM MgCl₂, 1 mM EGTA, 60% glycerol, 20 µM paclitaxel, pH 6.8) at 250,000 × g for 10 min. The cushion was then removed, and the pellet was washed with 2 × 20 µL wash buffer (80 mM PIPES, 2 mM MgCl₂, 1 mM EGTA, 10% glycerol, 20 µM paclitaxel, pH 6.8), and resuspended in 20 µL wash buffer. The polymerized MTs were stored in the dark at room temperature.

Constant-pulling assay. Unbinding force measurements were performed as previously described³² with the modifications indicated here. Briefly, the optical trap was calibrated via power spectrum analysis⁶⁶ and the trap stiffness (*k*) was adjusted between ~0.025 and 0.06 pN/nm, depending on whether a weak MT-binding or strong MT-binding construct was studied. The speed of the nano-positioning stage, which varied between ~90 and ~225 nm/s depending on which trap stiffness was used, was adjusted to produce a theoretical loading rate of 5.6 pN/s once the motor bound to the MT (the actual loading rate that the MTBD-MT bond is exposed to is somewhat smaller than this value and force dependent due to the compliance of the motor construct, see Fig. 2g). Trapping buffer (TB: 30 mM HEPES, 2 mM MgAc₂, 1 mM EGTA, 20 µM paclitaxel, 20 mM glucose, 2 mM Trolox, pH 7.2) was used for all experiments unless specified otherwise. 20 µL of 0.01 mg/mL polymerized MTs was flown into the prepared flow chamber described above and flushed immediately with 2 × 20 µL TB. The oxidation reagent, copper phenanthroline (Cu (PT)₃), was prepared fresh before each experiment by mixing equal volumes of 60 mM CuSO₄ and 180 mM phenanthroline. Dynein (or SRS-stalk-MTBD) constructs were diluted stepwise in TB containing 0.75 mg/mL α-casein. Next, a 4 µL solution containing anti-GFP antibody Fab fragment-coated, ~1-µm diameter beads (870 nm, carboxyl-modified polystyrene microspheres, Bangs Laboratories) (prepared as described previously⁶⁶, except that α-casein was used in place of BSA, and anti-GFP antibody Fab fragments were used instead of anti-GFP antibodies; the Fab fragment was prepared following the vendor's protocol) was incubated with appropriate concentrations of diluted dynein (or SRS-stalk-MTBD) to produce MT binding by <50% of the probed beads in the final assay to ensure trapping experiments were performed at the single-molecule level³² (the required dilution was in all cases (t100). The motor-bead solution was then incubated on ice for 10 min. To remove free unbound motors, beads were centrifuged for 2 min at 3000 rcf at 4 °C, followed by the removal of the supernatant. To crosslink the paired cysteines in the stalk, 20 µL oxidation buffer (30 mM HEPES with 300 µM Cu (PT)₃, pH 7.2) was used to resuspend the beads, followed by an incubation of the solution on ice for 10 min. A concentration of 20 µL TB with 0.75 mg/mL α-casein was then added to the solution and the centrifugation was repeated. After the supernatant was removed, 40 µL TB with 0.75 mg/ml α-casein and Gloxy (a glucose oxidase and catalase-based oxygen scavenging system⁶⁷) was used to resuspend the beads. The mixture was then introduced into the flow chamber, and the flow chamber was sealed with vacuum grease. As all dynein constructs are pre-diluted at least 100 times, followed by a resuspension of the motor-bound beads with 40 µL buffer twice, the nucleotide-free apo experiments reported herein were performed in the presence of a residual ATP concentration of 37.5 nM (the initial ATP concentration is 6 mM after the MT-binding and -release assay described above). For the experiments with TCEP (tris(2-carboxyethyl)phosphine) (reducing conditions), TCEP was added to a final concentration of 1 mM and incubated with the

dynein (or SRS-stalk-MTBD) construct on ice for 10 min before the construct was diluted. TCEP was added to the final resuspension solution to 0.2 mM.

Oscillatory trap assay. The measurement of the force-dependent unbinding rates of the mouse SRS- α stalk-MTBD construct using the oscillatory assay (Supplementary Figs. 5–7) was done as previously described by Cleary and coworkers³³. For detailed protocols, see Supplementary Note 3.

Single-molecule fluorescence motility assay. TB with 75 mM KAc (TBK75) was used for all single-molecule motility experiments. 20 μ L of 0.01 mg/ml Cy5-labeled MTs⁶⁵ was flown into the slide chamber as described above, and flushed immediately with 2 \times 20 μ L TBK75. To image the antibody-dimerized motors in the TIRF assay, 100 μ g anti-GFP antibody was labeled with 20 μ M Cy3-NHS at room temperature for 1 h, followed by the removal of the free dyes using an Amicon[®] Centrifugal Filter Unit. To oxidize the paired cysteines in the stalk, dynein constructs were diluted appropriately in a dilution buffer (30 mM HEPES, 2 mM MgCl₂, 150 mM KCl, pH 7.2), followed by the addition of an equal volume of 600 μ M Cu(PT)₃ in dilution buffer. The solution was then incubated on ice for 10 min, after which EDTA was added to final concentration of 5 mM and incubated on ice for 5 min to quench Cu(PT)₃. To reduce the disulfide bond that cross-linked the stalk helices, dynein was diluted appropriately in dilution buffer and an equal volume of 2 mM TCEP in dilution buffer was added to the motor. The solution was then incubated on ice for 10 min. Once the motor was either oxidized or reduced, Cy3-labeled anti-GFP antibody was added to the motor solution to a final concentration of 50 μ g/mL, and incubated on ice for 10 min. A final TBK75 solution containing 1 mM ATP, 1 mg/mL α -casein, 2 mM Trolox, Gloxy, 1 mM TCEP (in case of reducing experiments) and 0.5 μ L of the motor-antibody mixture was flown into the chamber, which was then sealed with vacuum grease. For the full-length homodimeric WT dynein, Dyn1_{471 KD}, the final TBK75 buffer containing the motor was directly flown into the chamber after the MTs were immobilized on the glass surface. Experiments were performed with a custom-built total TIRF microscope equipped with an Andor iXon Ultra EMCCD. The acquisition time was set to 500 ms/frame (if not specified otherwise), and a total 600 images was acquired for each movie. The kymographs were generated using Fiji.

Single-molecule dwelling time measurements. a concentration of 20 μ L of 0.01 mg/ml Cy5-labeled MTs⁶⁵ was flown into the slide chamber as described above, and flushed immediately with 2 \times 20 μ L TB. To oxidize the paired cysteines in the stalk, dynein constructs were diluted appropriately in a dilution buffer (30 mM HEPES, 2 mM MgCl₂, pH 7.2), followed by the addition of an equal volume of 600 μ M Cu(PT)₃ in dilution buffer. The solution was then incubated on ice for 10 min, after which EDTA was added to final concentration of 5 mM and incubated on ice for 5 min to quench Cu(PT)₃. To reduce the disulfide bond that cross-linked the stalk helices, dynein was diluted appropriately in dilution buffer and an equal volume of 2 mM TCEP in dilution buffer was added to the motor. The solution was then incubated on ice for 10 min. Once the motor was either oxidized or reduced, a final TB solution containing 1 mg/mL α -casein, 2 U/ml apyrase (apo state) or 1 mM ATP (ATP state), 2 mM Trolox, Gloxy, 1 mM TCEP (in case of reducing conditions) and 0.5 μ L of the motor was flown into the chamber, which was then sealed with vacuum grease. Experiments were performed with the custom-built TIRF microscope described above. The acquisition time was set to 100 ms per frame, and a total of 1000 images was acquired for each movie. Image sequences were analyzed using a custom-written MATLAB kymograph program described previously⁶⁸. GraphPad Prism was then used to fit the experimental CDFs of the measured dwell times to a theoretical CDF derived from an exponential decay function, yielding the unbinding rate k (Supplementary Fig. 2).

Analysis of data generated by the constant-pulling assay. As we showed previously³², the largest forces in our unbinding experiments using the constant-pulling assay (Fig. 2b) usually occur when the bead rebinds the MT before returning to the trap center (Fig. 2d). We call these secondary binding/unbinding events. For primary events, zero force is applied to the MD immediately after MT binding ($F_{\text{start}} = 0$), while for secondary events, $F_{\text{start}} > 0$. As the history of force applied to the bond depends on F_{start} , we focus only on primary events (Fig. 2d). Unbinding forces (example traces for all constructs studied are shown in Supplementary Figs. 11–27) were then analyzed using a semi-automated detection program written in MATLAB as previously described³². Measurements from multiple beads and experiments under the same conditions were pooled together and used to generate unbinding force histograms with 1-pN bins (as our force detection limit is \sim 0.3 pN, we only plot the force-dependent unbinding rates for forces above 0.5 pN). To facilitate comparison of the unbinding-force distributions and the derived force-dependent unbinding rates for both loading directions, we plot the data as a function of the absolute force values. Normalized histograms, approximating the probability density functions for unbinding at a given force, were then calculated by dividing the value of each bin by N , the total number of unbinding force measurements. Because the unbinding force distributions were not normally distributed, we estimated the sampling error by bootstrapping rather than calculating the standard error of the mean. For each histogram, 95% confidence intervals (CIs) for the mean statistic were calculated using the MATLAB `bootci()` function as described

before³². To compare the measured histograms of primary unbinding forces, we calculate the empirical (Kaplan-Meier) cumulative probability distribution functions using the MATLAB function `ecdf()` and perform a two-sample Kolmogorov-Smirnov (KS) test (yielding a p -value p_{KS}). To estimate p -values when comparing means of different distributions, we first created a dataset representing the sampling distribution of the mean for each original dataset, by bootstrapping 10⁵ means with the MATLAB function `bootstrp()`. We then subtracted these means pairwise to create a dataset representing the sampling distribution of the difference of the means. From each measurement in this dataset, we subtracted the mean difference of means, so as to shift the distribution to a mean of zero, consistent with the null hypothesis of no difference between the means of the original unbinding force distributions. The p -value (p_m) was then calculated as the proportion of the bootstrapped mean differences that were at least as great as difference observed between the means of the original datasets (two tailed test). If no bootstrapped mean differences met this criterion, p_m is reported as $<10^{-5}$.

Unlike our previous work, which assumed a constant loading rate in our unbinding-force assay³², here we considered the compliance of the dynein motor and bead linkage, resulting in a force-dependent loading rate (Fig. 2g and Supplementary Fig. 3). Uncertainty arises in the calculated unbinding rates as a function of force due to limited statistics for larger forces. To reduce this uncertainty, we used a kernel density estimator⁶⁹ to describe the probability density functions of the measured unbinding forces before transforming them into force-dependent unbinding rates⁷⁰ (see Supplementary Note 6 and Supplementary Figs. 28–31). While our new analysis confirms our previous conclusions, the absolute values of the calculated unbinding rates are slightly reduced compared to our previous results due to the motor's force-dependent compliance.

Reporting Summary. Further information on research design is available in the Nature Research Reporting Summary linked to this article.

Data availability

Data supporting the findings of this manuscript are available from the corresponding author upon reasonable request. A reporting summary for this Article is available as a Supplementary Information file. The datasets underlying Figs. 2e, 3b–g, 4a–e, 5c, 6b, c and 7a, b and Supplementary Figs. 2, 3, 4a, b and 6, 9b and 10 are provided as a Source Data file.

Received: 20 September 2018 Accepted: 2 July 2019

Published online: 26 July 2019

References

- Kardon, J. & Vale, R. Regulators of the cytoplasmic dynein motor. *Nat. Rev. Mol. Cell Biol.* **10**, 854–865 (2009).
- Vallee, R. B., Williams, J. C., Varma, D. & Barnhart, L. E. Dynein: an ancient motor protein involved in multiple modes of transport. *J. Neurobiol.* **58**, 189–200 (2004).
- Roberts, A. J., Kon, T., Knight, P. J., Sutoh, K. & Burgess, S. A. Functions and mechanics of dynein motor proteins. *Nat. Rev. Mol. Cell Biol.* **14**, 713–726 (2013).
- Niu, Q., Wang, X., Shi, M. & Jin, Q. A novel DYNC1H1 mutation causing spinal muscular atrophy with lower extremity predominance. *Neurol. Genet.* **1**, e20 (2015).
- Strickland, A. V. et al. Mutation screen reveals novel variants and expands the phenotypes associated with DYNC1H1. *J. Neurol.* **262**, 2124–2134 (2015).
- Ding, D. et al. Identification of a de novo DYNC1H1 mutation via WES according to published guidelines. *Sci. Rep.* **6**, 20423 (2016).
- Weedon, M. N. et al. Exome sequencing identifies a DYNC1H1 mutation in a large pedigree with dominant axonal Charcot-Marie-Tooth disease. *Am. J. Hum. Genet.* **89**, 308–312 (2011).
- Poirier, K. et al. Mutations in TUBG1, DYNC1H1, KIF5C and KIF2A cause malformations of cortical development and microcephaly. *Nat. Genet.* **45**, 639–647 (2013).
- Willemsen, M. H. et al. Mutations in DYNC1H1 cause severe intellectual disability with neuronal migration defects. *J. Med. Genet.* **49**, 179–183 (2012).
- Fiorillo, C. et al. Novel dynein DYNC1H1 neck and motor domain mutations link distal spinal muscular atrophy and abnormal cortical development. *Hum. Mutat.* **35**, 298–302 (2014).
- Peeters, K. et al. Novel mutations in the DYNC1H1 tail domain refine the genetic and clinical spectrum of dyneinopathies. *Hum. Mutat.* **36**, 287–291 (2015).
- Snider, J. & Houry, W. A. AAA+ proteins: diversity in function, similarity in structure. *Biochem. Soc. Trans.* **36**, 72–77 (2008).
- Schmidt, H., Gleave, E. S. & Carter, A. P. Insights into dynein motor domain function from a 3.3-Å crystal structure. *Nat. Struct. Mol. Biol.* **19**, 492–497 (2012).

14. Kon, T. et al. The 2.8 Å crystal structure of the dynein motor domain. *Nature* **484**, 345–350 (2012).
15. Gennerich, A. & Vale, R. D. Walking the walk: how kinesin and dynein coordinate their steps. *Curr. Opin. Cell Biol.* **21**, 59–67 (2009).
16. Hancock, W. O. The Kinesin–1 Chemomechanical Cycle: Stepping Toward a Consensus. *Biophys. J.* **110**, 1216–1225 (2016).
17. Block, S. M. Kinesin motor mechanics: binding, stepping, tracking, gating, and limping. *Biophys. J.* **92**, 2986–2995 (2007).
18. Sweeney, H. L. & Houdusse, A. Structural and functional insights into the Myosin motor mechanism. *Annu. Rev. Biophys.* **39**, 539–557 (2010).
19. Batters, C. & Veigel, C. Mechanics and activation of unconventional myosins. *Traffic* **17**, 860–871 (2016).
20. Carter, A. P., Cho, C., Jin, L. & Vale, R. D. Crystal structure of the dynein motor domain. *Science* **331**, 1159–1165 (2011).
21. Kon, T., Sutoh, K. & Kurisu, G. X-ray structure of a functional full-length dynein motor domain. *Nat. Struct. Mol. Biol.* **18**, 638–642 (2011).
22. Kon, T., Mogami, T., Ohkura, R., Nishiura, M. & Sutoh, K. ATP hydrolysis cycle-dependent tail motions in cytoplasmic dynein. *Nat. Struct. Mol. Biol.* **12**, 513–519 (2005).
23. Bhabha, G. et al. Allosteric communication in the dynein motor domain. *Cell* **159**, 857–868 (2014).
24. Holzbaur, E. L. & Johnson, K. A. Microtubules accelerate ADP release by dynein. *Biochemistry* **28**, 7010–7016 (1989).
25. Porter, M. E. & Johnson, K. A. Transient state kinetic analysis of the ATP-induced dissociation of the dynein-microtubule complex. *J. Biol. Chem.* **258**, 6582–6587 (1983).
26. Kon, T. et al. Helix sliding in the stalk coiled coil of dynein couples ATPase and microtubule binding. *Nat. Struct. Mol. Biol.* **16**, 325–333 (2009).
27. Gibbons, I. R. et al. The affinity of the dynein microtubule-binding domain is modulated by the conformation of its coiled-coil stalk. *J. Biol. Chem.* **280**, 23960–23965 (2005).
28. McNaughton, L., Tikhonenko, I., Banavali, N. K., LeMaster, D. M. & Koonce, M. P. A low affinity ground state conformation for the Dynein microtubule binding domain. *J. Biol. Chem.* **285**, 15994–16002 (2010).
29. Uchimura, S. et al. A flipped ion pair at the dynein-microtubule interface is critical for dynein motility and ATPase activation. *J. Cell Biol.* **208**, 211–222 (2015).
30. Redwine, W. B. et al. Structural basis for microtubule binding and release by dynein. *Science* **337**, 1532–1536 (2012).
31. Sivagurunathan, S. et al. Analyses of Dynein heavy chain mutations reveal complex interactions between Dynein motor domains and cellular Dynein functions. *Genetics* **191**, 1157–1179 (2012).
32. Nicholas, M. P. et al. Cytoplasmic dynein regulates its attachment to microtubules via nucleotide state-switched mechanosensing at multiple AAA domains. *Proc. Natl Acad. Sci. USA* **112**, 6371–6376 (2015).
33. Cleary, F. B. et al. Tension on the linker gates the ATP-dependent release of dynein from microtubules. *Nat. Commun.* **5**, 4587 (2014).
34. Qiu, W. et al. Dynein achieves processive motion using both stochastic and coordinated stepping. *Nat. Struct. Mol. Biol.* **19**, 193–200 (2012).
35. DeWitt, M. A., Chang, A. Y., Combs, P. A. & Yildiz, A. Cytoplasmic dynein moves through uncoordinated stepping of the AAA+ring domains. *Science* **335**, 221–225 (2012).
36. Gennerich, A., Carter, A. P., Reck-Peterson, S. L. & Vale, R. D. Force-induced bidirectional stepping of cytoplasmic dynein. *Cell* **131**, 952–965 (2007).
37. Reck-Peterson, S. L. et al. Single-molecule analysis of dynein processivity and stepping behavior. *Cell* **126**, 335–348 (2006).
38. Imamura, K., Kon, T., Ohkura, R. & Sutoh, K. The coordination of cyclic microtubule association/dissociation and tail swing of cytoplasmic dynein. *Proc. Natl Acad. Sci. USA* **104**, 16134–16139 (2007).
39. Mogami, T., Kon, T., Ito, K. & Sutoh, K. Kinetic characterization of tail swing steps in the ATPase cycle of Dictyostelium cytoplasmic dynein. *J. Biol. Chem.* **282**, 21639–21644 (2007).
40. Roberts, A. J. et al. AAA+Ring and linker swing mechanism in the dynein motor. *Cell* **136**, 485–495 (2009).
41. Shima, T., Kon, T., Imamura, K., Ohkura, R. & Sutoh, K. Two modes of microtubule sliding driven by cytoplasmic dynein. *Proc. Natl Acad. Sci. USA* **103**, 17736–17740 (2006).
42. Khataee, H. & Howard, J. Force generated by two kinesin motors depends on the load direction and intermolecular coupling. *Phys. Rev. Lett.* **122**, 188101 (2019).
43. Pypassopoulos, S., Shuman, H. & Ostap, E. M. Modulation of kinesin's load-bearing capacity by force geometry and the microtubule track. *bioRxiv* 587089. <https://doi.org/10.1101/587089> (2019).
44. Belyy, V. & Yildiz, A. Studying the mechanochemistry of processive cytoskeletal motors with an optical trap. *Methods Enzym.* **582**, 31–54 (2017).
45. Schmidt, H. & Carter, A. P. Structure and mechanism of the dynein motor ATPase. *Biopolymers* **105**, 557–567 (2016).
46. DeWitt, M. A., Cypranowska, C. A., Cleary, F. B., Belyy, V. & Yildiz, A. The AAA3 domain of cytoplasmic dynein acts as a switch to facilitate microtubule release. *Nat. Struct. Mol. Biol.* **22**, 73–80 (2015).
47. Schmidt, H., Zalyte, R., Urnavicius, L. & Carter, A. P. Structure of human cytoplasmic dynein-2 primed for its power stroke. *Nature* **518**, 435–438 (2015).
48. Zhang, K. et al. Cryo-EM reveals how human cytoplasmic Dynein Is auto-inhibited and activated. *Cell* **169**, 1303–1314 (2017).
49. Cianfrocco, M. A., DeSantis, M. E., Leschziner, A. E. & Reck-Peterson, S. L. Mechanism and regulation of cytoplasmic dynein. *Annu. Rev. Cell Dev. Biol.* **31**, 83–108 (2015).
50. Cho, C., Reck-Peterson, S. L. & Vale, R. D. Regulatory ATPase sites of cytoplasmic dynein affect processivity and force generation. *J. Biol. Chem.* **283**, 25839–25845 (2008).
51. Kon, T., Nishiura, M., Ohkura, R., Toyoshima, Y. Y. & Sutoh, K. Distinct functions of nucleotide-binding/hydrolysis sites in the four AAA modules of cytoplasmic dynein. *Biochemistry* **43**, 11266–11274 (2004).
52. Holzbaur, E. L. & Johnson, K. A. ADP release is rate limiting in steady-state turnover by the dynein adenosinetriphosphatase. *Biochemistry* **28**, 5577–5585 (1989).
53. Trokter, M., Mücke, N. & Surrey, T. Reconstitution of the human cytoplasmic dynein complex. *Proc. Natl Acad. Sci. USA* **109**, 20895–20900 (2012).
54. Nicholas, M. P. et al. Control of cytoplasmic dynein force production and processivity by its C-terminal domain. *Nat. Commun.* **6**, 6206 (2015).
55. McKenney, R. J., Huynh, W., Tanenbaum, M. E., Bhabha, G. & Vale, R. D. Activation of cytoplasmic dynein motility by dynactin-cargo adapter complexes. *Science* **345**, 337–341 (2014).
56. Schlager, M. A., Hoang, H. T., Urnavicius, L., Bullock, S. L. & Carter, A. P. In vitro reconstitution of a highly processive recombinant human dynein complex. *EMBO J.* **33**, 1855–1868 (2014).
57. Torisawa, T. et al. Autoinhibition and cooperative activation mechanisms of cytoplasmic dynein. *Nat. Cell Biol.* **16**, 1118–1124 (2014).
58. Toropova, K., Mladenov, M. & Roberts, A. J. Intraflagellar transport dynein is autoinhibited by trapping of its mechanical and track-binding elements. *Nat. Struct. Mol. Biol.* **24**, 461–468 (2017).
59. Urnavicius, L. et al. Cryo-EM shows how dynactin recruits two dyneins for faster movement. *Nature* **554**, 202–206 (2018).
60. Grotjahn, D. A. et al. Cryo-electron tomography reveals that dynactin recruits a team of dyneins for processive motility. *Nat. Struct. Mol. Biol.* **25**, 203–207 (2018).
61. Rao, L., Hulsemann, M. & Gennerich, A. Combining structure-function and single-molecule studies on cytoplasmic dynein. *Methods Mol. Biol.* **1665**, 53–89 (2018).
62. Gietz, R. D. & Schiestl, R. H. High-efficiency yeast transformation using the LiAc/SS carrier DNA/PEG method. *Nat. Protoc.* **2**, 31–34 (2007).
63. Nilsson, B. et al. A synthetic IgG-binding domain based on staphylococcal protein A. *Protein Eng.* **1**, 107–113 (1987).
64. Cormack, B. P. et al. Yeast-enhanced green fluorescent protein (yEGFP): a reporter of gene expression in *Candida albicans*. *Microbiology* **143**, 303–311 (1997). (Pt 2).
65. Nicholas, M. P., Rao, L. & Gennerich, A. Covalent immobilization of microtubules on glass surfaces for molecular motor force measurements and other single-molecule assays. *Methods Mol. Biol.* **1136**, 137–169 (2014).
66. Nicholas, M. P., Rao, L. & Gennerich, A. An improved optical tweezers assay for measuring the force generation of single kinesin molecules. *Methods Mol. Biol.* **1136**, 171–246 (2014).
67. Yildiz, A. et al. Myosin V walks hand-over-hand: single fluorophore imaging with 1.5-nm localization. *Science* **300**, 2061–2065 (2003).
68. Rao, L. et al. *Mol. Biol. Cell* **24**, 2362–2377 (2013).
69. Silverman, B. W. *Density estimation for Statistics and Data Analysis* (Chapman & Hall/CRC, Boca Raton, FL, 1998).
70. Dudko, O. K., Hummer, G. & Szabo, A. Theory, analysis, and interpretation of single-molecule force spectroscopy experiments. *Proc. Natl Acad. Sci. USA* **105**, 15755–15760 (2008).

Acknowledgements

A.G. thanks Erik Schäffer and Henry Hess for helpful comments on the manuscript and Lisa Baker for help with the editing of the manuscript. The authors are supported by the National Institutes of Health (NIH) grant R01GM098469. M.P.N. received support from the NIH-funded Medical Scientist Training and Molecular Biophysics Training programs at the Albert Einstein College of Medicine (NIH grants T32GM007288 and T32GM008572, respectively). F.B. was supported by the Alexander von Humboldt Foundation.

Author contributions

L.R., F.B., M.P.N. and A.G. designed research; L.R., F.B., and A.G. performed research; L.R. engineered mutant yeast strains and produced and purified proteins; L.R., F.B. and

A.G. analyzed the data; F.B. designed algorithms to transform unbinding-force data into force-dependent unbinding rates; F.B. and A.G. performed the theoretical analysis of the differences between the oscillatory and constant-pulling assays; L.R., F.B., M.P.N. and A.G. wrote the paper.

Additional information

Supplementary Information accompanies this paper at <https://doi.org/10.1038/s41467-019-11231-8>.

Competing interests: The authors declare no competing interests.

Reprints and permission information is available online at <http://npg.nature.com/reprintsandpermissions/>

Peer review information: *Nature Communications* thanks Erik Schäffer and the other anonymous reviewer(s) for their contribution to the peer review of this work.

Publisher's note: Springer Nature remains neutral with regard to jurisdictional claims in published maps and institutional affiliations.



Open Access This article is licensed under a Creative Commons Attribution 4.0 International License, which permits use, sharing, adaptation, distribution and reproduction in any medium or format, as long as you give appropriate credit to the original author(s) and the source, provide a link to the Creative Commons license, and indicate if changes were made. The images or other third party material in this article are included in the article's Creative Commons license, unless indicated otherwise in a credit line to the material. If material is not included in the article's Creative Commons license and your intended use is not permitted by statutory regulation or exceeds the permitted use, you will need to obtain permission directly from the copyright holder. To view a copy of this license, visit <http://creativecommons.org/licenses/by/4.0/>.

© The Author(s) 2019

“Molecular mechanism of cytoplasmic dynein tension sensing”

Rao et al.

Supplementary Information

Supplementary Notes

Supplementary Note 1

Structural rendering. All images showing dynein structures were rendered using Chimera (UCSF). To construct the dynein motor domain bound to α/β -tubulin in its strong binding state (Fig. 1b), the structure of the *D. discoideum* dynein motor domain (PDB entry 3VKG) was combined with the mouse MTBD with the short stalk bound to bovine α/β -tubulin in the strong binding state (PDB entry 3J1T) using a sequence alignment tool. To construct the dynein motor domain bound to α/β -tubulin in its weak binding state, the structure of the mouse MTBD with stalk in the weak binding state (PDB entry 3WUQ) and the structure of the human dynein-2 motor domain (PDB entry 4RH7) were aligned and combined. The created dynein structures were then used to generate the morphing conformations shown in Fig. 3a and Supplemental Fig. 1b.

Supplementary Note 2

Cross-linking efficiency of the stalk helices. The cross-linking efficiency of the stalk helices of the dynein and SRS α -, β - and γ -mutants was determined by a combination of optical trapping measurements and zero-load motility experiments using the antibody-dimerized cross-linked motors. The cross-linking efficiency of the β - and γ -mutants can be directly determined from the performed unbinding-force experiments: under non-reducing conditions to promote cross-linking of the stalk helices, only 2 out of 40 beads coated with the β -mutant and 1 out of 26 beads coated with the γ -mutant exhibited the anisotropic unbinding behavior as seen for the WT motor (Figs. 2e-f and 3c,d) (at a bead fraction of less than 50% to ensure measurements at the single-molecule level¹), suggesting that the cross-linking efficiencies for the β - and γ -mutants are close to 95%.

To estimate the cross-linking efficiency of the α -mutant, which shows large unbinding forces in both directions but with an overall remaining asymmetry (Fig. 3b), we performed zero-load motility experiments in the absence and presence of 2 mM TCEP (which cleaves the disulfide bonds of the cross-linked stalk helices). In the absence of TCEP under non-reducing conditions following the cross-linking of the cysteine pair, the antibody-dimerized Dyn1_{331kDa}- α CL motor moved processively at a reduced average speed of ~ 11 nm/s (Fig. 7b, top right). In the presence of TCEP, the movement of the antibody-dimerized Dyn1_{331kDa}- α motor (109 ± 3 nm/s [\pm SEM; $N = 281$]; Fig. 7b, bottom right) was identical to that of the antibody-dimerized WT motor, Dyn1_{331kDa}, which moved at an average speed of ~ 110 nm/s under non-reducing (Fig. 7a, top right) and reducing (Supplemental Fig. 10b, top) conditions. To determine whether some of the moving Dyn1_{331kDa}- α motors were heterodimers consisting of a motor domain with non-cross-linked stalk helices (Dyn1_{331kDa}- α) and a motor domain with cross-linked stalk helices (Dyn1_{331kDa}- α CL) or homodimers of non-cross-linked Dyn1_{331kDa}- α motor domains, we first determined the velocity of the heterodimers by mixing the Dyn1_{331kDa}- α CL mutant with a two-fold higher concentration of WT Dyn1_{331kDa} (a condition in which 44% of the motors are expected to be heterodimers, see legend to Supplemental Fig. 10). Analyzing the obtained velocity histogram with three velocity peaks yields a velocity of 43.4 ± 1.2 nm/s (mean \pm SEM) for the Dyn1_{331kDa}-Dyn1_{331kDa}- α CL heterodimers when the measured velocities of Dyn1_{331kDa}- α CL (Fig. 7b, top right) and WT Dyn1_{331kDa} (Fig. 7a, top right) are used as fixed parameters (see also legend to Supplemental Fig. 10). The velocity of the heterodimer is therefore $\sim 40\%$ of the velocity of the WT motor. Consistent with this measurement, Cleary et al. reported that a heterodimer of a WT motor domain fused to an SRS-stalk-MTBD construct in the presumed “ α -

registration” (see discussion in the main text) moves at a threefold lower speed than the WT homodimeric motor². That the WT Dyn1_{331kDa}-Dyn1_{331kDa}- α CL heterodimers move faster (relative to the WT motor) than the WT Dyn1_{331kDa}-SRS-stalk-MTBD heterodimers makes sense: while both motor domains of the Dyn1_{331kDa}-Dyn1_{331kDa}- α CL heterodimers can contribute to forward-directed motion by generating power strokes, only the WT motor domain of the Dyn1_{331kDa}-SRS-stalk-MTBD heterodimers is an active motor that can generate a power stroke (the SRS-stalk-MTBD construct acts just as a MT tether). With two motors generating power strokes instead of one, one might expect that the average velocity of the Dyn1_{331kDa}-Dyn1_{331kDa}- α CL heterodimers compared to the Dyn1_{331kDa}-SRS-stalk-MTBD heterodimers would have been more markedly increased, however, the relative velocity changes of the two constructs compared to the WT homodimers are still close. This may be explained by the fact that the Dyn1_{331kDa}- α CL motor domains with the cross-linked stalk helices—because they are cross-linked into the true α -registration—have a significantly higher MT-binding strength than the SRS-stalk-MTBD construct used by Cleary et al. (Fig. 4a-c).

With the knowledge of the velocity of the Dyn1_{331kDa}-Dyn1_{331kDa}- α CL heterodimers, we can now estimate the stalk cross-linking efficiency of the Dyn1_{331kDa}- α CL mutant by fitting two Gaussian functions to the histogram in Fig. 7b (top right): one centered at 10.6 nm/s (free parameter), and another one at 43.4 nm/s (the mean velocity and its standard deviation, SD = 20.2 nm/s [obtained from the analysis of the histogram in Supplemental Fig. 10c] are used as fixed parameters). The number of events in each bin under the Gaussian curve centered at 43.4 nm/s (see inset in Supplemental Fig. 10d) correspond to the number of Dyn1_{331kDa}-Dyn1_{331kDa}- α CL heterodimers (the number of the fast moving Dyn1_{331kDa}-Dyn1_{331kDa} homodimers was too low to

fit a third Gaussian function). Calculation of the number of events under the two Gaussian functions as well as the scattered events of higher velocities generated by non-crosslinked homodimers yielded a total of 332 events: 290 events for the Dyn1_{331kDa}- α CL homodimers (comprised of 580 Dyn1_{331kDa}- α CL motor domains with cross-linked stalk helices), 35 events for the Dyn1_{331kDa}-Dyn1_{331kDa}- α CL heterodimers (comprised of 35 Dyn1_{331kDa}- α CL motor domains with cross-linked stalk helices and 35 Dyn1_{331kDa}- α motor domains without cross-linked stalk helices), and 7 events for the Dyn1_{331kDa}- α homodimeric motors (14 Dyn1_{331kDa}- α motor domains without cross-linked stalk helices). From a total number of 664 motor domains, 613 Dyn1_{331kDa}- α CL motor domains had cross-linked stalk helices, yielding a cross-linking efficiency of the stalk helices of 92.3%. However, as a result of the limited number of heterodimeric motors in this experiment, the Gaussian function centered at 43.4 nm/s slightly overestimates the true number of events under the curve that overlaps with the 10.6 nm/s peak (Supplemental Fig. 10d, inset). We therefore consider the ~92% cross-linking efficiency calculated here to be the lower bound. In addition, the ~95% cross-linking efficiency estimated for the β - and γ -mutants suggest that the increased time that passes under non-reducing conditions until the trapping experiments are performed (see protocol above) could also increase the cross-linking efficiency of the α -mutant to a value close to ~95% when performing the trapping experiments.

Supplementary Note 3

Oscillatory trap assay. The measurement of the force-dependent unbinding rates of the mouse SRS- α stalk-MTBD construct using the oscillatory trap assay (Supplementary Figs. 5-8) was done as previously described by Cleary and co-workers². Briefly, a polystyrene bead coated with the SRS- α stalk-MTBD construct (at a concentration where less than 30% of the beads interacted

with the surface-attached MTs) is rapidly moved ($v > 250 \mu\text{m/s}$) between two positions ($\pm 250 \text{ nm}$) every 2.5 seconds (Supplementary Fig. 5, left). When a bead-bound SRS construct binds to the MT before (most likely) or during the switching event, the bead eventually stops following the moving trap, during which time the SRS construct experiences a constant load given by the momentarily maintained bead-trap separation times the spring constant; however, before the constant-load phase of the assay is reached, the MTBD-MT bond experiences a rapidly changing loading rate (Supplementary Fig. 8). Once the SRS construct detaches, the bead quickly follows the trap to its new position (Supplementary Fig. 5). The waiting time between switching events was adjusted so that the detachments of the SRS constructs from the MTs occurred before the trap moved on to a new position. To prevent the measurement of multiple SRS constructs contributing to the linkage between the bead and MT, multi-step release events were discarded from the analysis². The MT-bound times of the SRS- α stalk-MTBD construct under the various constant loads were then automatically detected and measured using a custom-written MATLAB program. The measured MT-bound times were then sorted by force and binned every ~ 100 data points and converted into cumulative distributions to allow a bin-size independent estimation of the force-dependent unbinding rates (Supplementary Fig. 6). The average detachment rate for each bin was then determined by fitting the experimental cumulative distributions to a theoretical cumulative distribution function (CDF) derived from a single exponential decay function:

$$CDF(t) = 1 - \exp(-kt),$$

where k is the characteristic unbinding rate (in s^{-1}). The nonlinear least squares fitting was performed using MATLAB. To estimate the error of the unbinding rate k , we bootstrapped 200 samples and fit them as described above. The standard deviation of the resulting set of unbinding rates was taken as the error estimate. The unbinding rate was then plotted with the average force of the data points in each bin (Supplementary Fig. 8a).

Supplementary Note 4

Calculation of force and loading rate for the oscillatory and constant-pulling assays, and discussion of the possible impacts of the calculated values on the performed bond-lifetime measurements. The loading rate is defined as the rate of change of the force on the molecular bond between the MTBD and the MT. The force on the molecular bond is given by the force-extension relation $F_m(x_B)$ for the bead position x_B . By differentiation, we obtain the time-dependent loading rate

$$\frac{dF_m}{dt} = \frac{dF_m}{dx_B} \frac{dx_B}{dt}.$$

We therefore have to calculate the derivative dF_m/dx_B of the force-extension relation and the velocity dx_B/dt of the bead to obtain the loading rate. Assuming an overdamped motion for the bead, its position is described by the differential equation

$$\gamma \frac{dx_B}{dt} = k(x_T - x_B) - F_m(x_B), \quad \text{Eq. 1}$$

in which k is the spring constant of the optical trap, x_T is the position of the trap and γ is the hydrodynamic drag coefficient of the bead. As γ is influenced by the proximity of the bead to the cover slip surface, we calculate γ from the drag in bulk solution, $\gamma_0 = 3\pi d\eta$, according to Faxén's law³:

$$\gamma = \frac{\gamma_0}{1 - \frac{9R}{16} + \frac{1R^3}{8} - \frac{45R^4}{256} - \frac{1R^5}{16}}.$$

Here, $R = d/(d + 2Z_B)$, d the bead diameter, and Z_B the distance from the surface of the cover slip to the surface of the bead⁴. With a bead diameter of 870 nm and $Z_B=50$ nm, we obtain $\gamma = 2.3\gamma_0$. As the viscosity of water at 25 °C is 0.89 cP, γ_0 assumes a value of 7.3 nNs/m and we obtain

$\gamma = 16.8$ nNs/m. With a trap stiffness of 0.05 pN/nm used by Cleary et al.² and a trap displacement of $x_0 = 250$ nm, an initial speed (at $t = 0$) of 0.74 mm/s can be reached.

In the following, we demonstrate that the force-extension is related to the force-dependent loading rate as measured in the constant-pulling assay (Supplementary Fig. S3). In this assay, the strength of the molecular bond between the MTBD and MT is probed with the optical trap and the loading rate follows from a simple calculation of two springs in series, as given by⁵

$$r = \frac{k v}{1 + k \frac{dL}{dF_m}}, \quad \text{Eq. 2}$$

in which k is the trap stiffness, v the pulling speed of the trap and dL/dF_m is the change of the molecule length L with respect to a change of force F_m . Consistency with our measured loading rates in Supplementary Figure 3 implies

$$F_m(L) = \hat{a}(e^{L/\hat{b}} - 1)$$

as an Ansatz for the force-extension relation. Using this Ansatz in Equation 2, and comparing it to the fit to the force-dependent loading rate measured for the SRS α -stalk-MTBD construct (Supplementary Fig. 3b), we obtain $\hat{a} = a = 0.23$ pN and $\hat{b} = (b - a)/k = 40$ nm.

In the oscillatory trap used by Cleary and co-workers², the trap is displaced by 250 nm. However, the motor can bind to different positions along the MT during the dwelling of the bead in-between the switching events so that the extension of the construct varies from switching event to switching event. If we assume that the SRS α -stalk-MTBD construct is soft and does not bind to the MT under tension, the maximum distance that the SRS α -stalk-MTBD construct can be theoretically stretched is 250 nm. In contrast, if the construct binds to a MT-binding site located toward the

switching direction and/or if the bead has to rotate before the construct is stretched, the total extension of the construct is less than the maximum 250 nm. To account for this variability of the total extension, we include the parameter L_0 in the force-extension relation in such a way that the construct is not stretched if $L < L_0$:

$$F_m(L) = \begin{cases} 0, & L < L_0 \\ \hat{a}(e^{L/\hat{b}} - 1), & L \geq L_0 \end{cases} \quad \text{Eq. 3}$$

For the oscillatory trap, we assume that the trap is displaced by 250 nm instantaneously. To calculate the position of the bead, its velocity, the force, and the loading rate, we combine Equations 2 and 3 and solve Equation 1 numerically for the initial conditions $x_B(0) = 0$ nm and $x_T(0) = 250$ nm, and examine three different cases of molecular tension. By choosing $L_0 = 0$ nm, $L_0 = 90$ nm, and $L_0 = 165$ nm, the tension on the molecular bond of the SRS α -stalk-MTBD construct is 6.4 pN, 3 pN, and 1 pN, respectively (Supplementary Fig. 8a-c). The maximum force that can be measured when the trap is displaced by $\Delta x = 250$ nm is given by $F = k\Delta x = 12.5$ pN for a spring constant of 0.05 pN/nm. In this limit, the construct is infinitely stiff and the bead remains at the same position ($x_B = 0$ nm) although the trap is displaced. However, when we consider the compliance of the construct (see above), we obtain a theoretical maximal measurable force of ~ 6.5 pN. This suggests that the detachment forces measured with the oscillatory assay that are significantly larger than this value may be the result of two (or more) SRS α -stalk-MTBD constructs contributing to the linkage between the bead and MT, which could increase the overall stiffness. In overall agreement with this theoretical upper force limit, out of 473 single release events we measured in backward direction, less than 1.5% (7 events) were larger than 7 pN with a maximum measured value of 8.6 pN.

Our results show that loading rates between a few thousand up to almost 25,000 pN/s can be reached when using the oscillatory assay (Supplementary Fig. 8a-c). These loading rates are usually reached after a few hundreds of microseconds ($\sim 180 \mu\text{s}$ when establishing a final force of 6.4 pN, $\sim 340 \mu\text{s}$ for 3 pN and $\sim 470 \mu\text{s}$ for 1 pN). The time it takes to reach 63% ($1/e$ value) of the final maximal force is similar: $\sim 250 \mu\text{s}$ for 6.4 pN, $\sim 320 \mu\text{s}$ for 3 pN and $\sim 360 \mu\text{s}$ for 1 pN. In comparison to the constant-pulling experiments, which can be analyzed by combining Equation 1 with the pulling protocol $x_T(t) = v t$, these are rather extreme numbers. In the constant-pulling assay used herein, loading rates are typically smaller than 5 pN/s and reached after a couple of seconds (Supplementary Fig. 8d and Fig. 2g).

The time during which the extreme loading rates act on the MTBD-MT bond of the SRS α -stalk-MTBD constructs when using the oscillatory assay are close to the timescales within which topological reorganizations of proteins occur⁶. It may therefore be possible that the conformation of the MT-bound MTBD is affected by quick changes in tension even when the absolute force is in the lower pN range. That we only observe a significant discrepancy in the bond lifetimes obtained from both unbinding-force assays under forward load (Supplementary Fig. 7) suggests that the MTBD-MT bond of the SRS α -stalk-MTBD construct with the non-crosslinked stalk helices is more sensitive to external perturbations when the force is applied in forward direction.

Supplementary Note 5

Discussion of the effects of the cross linking the stalk helices of the SRS constructs. Our analysis revealed that the non-cross-linked SRS- α stalk-MTBD construct and the SRS- α stalk-MTBD construct with the stalk helices cross-linked in the α -registration (85:82 SRS- α stalk-MTBD CL)

show statistically different unbinding-force behaviors ($p_{ks} < 10^{-21}$ (forward) and $p_{ks} < 10^{-19}$ (backward) [SRS- α stalk-MTBD vs. SRS- α stalk-MTBD CL], Fig. 4b,c) and statistically different mean unbinding forces (SRS- α stalk-MTBD apo 1.1 [1.0, 1.2] pN vs. SRS- α stalk-MTBD CL apo 2.2 [2.0, 2.4], $p_m < 10^{-10}$ (forward) and SRS- α stalk-MTBD apo 1.2 [1.1, 1.2] pN vs. SRS- α stalk-MTBD CL apo 2.9 [2.6, 3.3], $p_m < 10^{-10}$ (backward)). As the SRS- α stalk-MTBD CL construct shows statistically indistinguishable unbinding-force behavior from the dynein motor domain with the cross-linked α -registration, Dyn1_{331kDa}- α CL ($p_{ks} = 0.63$ (forward) and $p_{ks} = 0.38$ (backward) [SRS- α stalk-MTBD CL vs. Dyn1_{331kDa}- α CL]), Figs. 3b and 4c), these data suggest that the SRS- α stalk-MTBD construct with the non-cross-linked stalk helices does not assume the α -registration. In contrast, the SRS- β stalk-MTBD construct shows the same unbinding behaviors whether the stalk helices are cross-linked in the β -registration or not ($p_{ks} = 0.76$ [SRS- β stalk-MTBD forward vs. SRS- β stalk-MTBD CL forward] and $p_{ks} = 0.42$ [SRS- β stalk-MTBD backward vs. SRS- β stalk-MTBD CL backward], Fig. 4d,e), suggesting that the SRS- β stalk-MTBD constructs assumes the β -registration with or without stalk cross-linking.

Interestingly, when paired cysteines were placed at the same positions as in the dynein motor domain with the cross-linked β -registration (Dyn1_{331kDa}- β CL mutant), the SRS- α stalk-MTBD construct could be cross-linked in the β -registration despite the apparent fusion of the dynein stalk to the coiled-coil base of SRS in the α -registration (Supplemental Fig. 4b). This result, together with the statistically different unbinding-force behaviors of the cross-linked and non-cross-linked SRS- α stalk-MTBD constructs, suggest that a thermodynamically-driven sliding of the helices between the α - and β -registrations (half a heptad) is possible in the absence of load (while the constructs are in solution) despite the inability of applied tension to cause registration changes in the non-crosslinked MT-bound SRS- α stalk-MTBD construct. This suggests that

registration changes in the MT-bound SRS- α stalk-MTBD construct are somehow prevented in the SRS construct when bound to MTs under applied directional tension.

Supplementary Note 6

Calculation of the unbinding rates from the unbinding-force histograms. To determine the force-dependent unbinding rates from the measured unbinding forces, Dudko and coworkers⁷ introduced the relation for the unbinding rate,

$$\epsilon(F) = \frac{\dot{F}P(F)}{1 - \int_0^F P(F')dF'},$$

in which $P(F)$ is the probability density of the unbinding forces and \dot{F} is the force-dependent loading rate¹. The denominator is also known as the survival function, $S(F) = 1 - CDF(F)$. The loading rate \dot{F} is the change of the force applied to the bond per unit of time and depends on the stiffness of the trap, the compliance of the bond, and the pulling speed. As a first approximation and for proteins with negligible compliance, the loading rate can be estimated by the product of the pulling speed and the trap stiffness as we have done before⁸. However, to further improve the accuracy of the unbinding rates obtained from our unbinding-force experiments of single-headed dynein, we now take the motor's compliance indirectly into account by determining the force-dependent loading rates from the unbinding-force traces. To do so, we fit a line to the 200-ms trace segment preceding the detachment of the motor of each measured unbinding-force event. This

¹ We have previously shown that the Dudko method can be applied to more complex bonds (such as slip-ideal and catch-slip bonds) if the time scale of the experiment (the time of how fast one pulls on the bond) is long compared to the time scale of how fast the bond reaches steady state. At a loading rate of smaller than 5 pN/s in our constant-pulling assay (Fig. 2g), the force increases by less than 0.5 pN in 100 ms. In addition, the fastest unbinding rate we have measured herein is smaller than 10/s, which corresponds to a bond lifetime of 100 ms. As the typical equilibration time in proteins is less than a millisecond¹⁷, the condition that we pull slowly enough to assume equilibrium is therefore fulfilled.

way, we obtained a loading rate (in pN/s) for each unbinding event. By binning all measured slopes according to their associated unbinding forces and averaging them in each bin (1-pN bins), we calculated an average force-dependent loading rate (Supplemental Fig. 3a). To further improve the statistics of our measurements, we measured the force-dependent loading rates for the WT motor, Dyn1_{331kDa}, and the α -mutant with the cross-linked stalk helices, both in forward and in backward direction. The fact that the force-dependent loading rates for all four data sets (two data sets for forward and backward directions for each construct) coincide, suggests that the compliance is similar for both constructs and neither depends on the direction of pulling nor on whether the stalk helices are cross linked. Therefore, we combined all measured slopes into single data set and calculated the average loading rate (Supplemental Fig. 3a, red dots). To obtain a theoretical approximation, we fit a rational function to this average loading rate using two free parameters and the maximum loading rate of 5.6 pN/s as a fixed parameter. This approach provides us with an excellent approximation for the force-dependent loading rate of the tail-truncated, single-headed *S. cerevisiae* dynein, which we use to convert the measured unbinding-force histograms into unbinding rates. We applied the same procedure to the data of the SRS constructs to obtain the force-dependent loading rate (see Supplemental Fig. 3b).

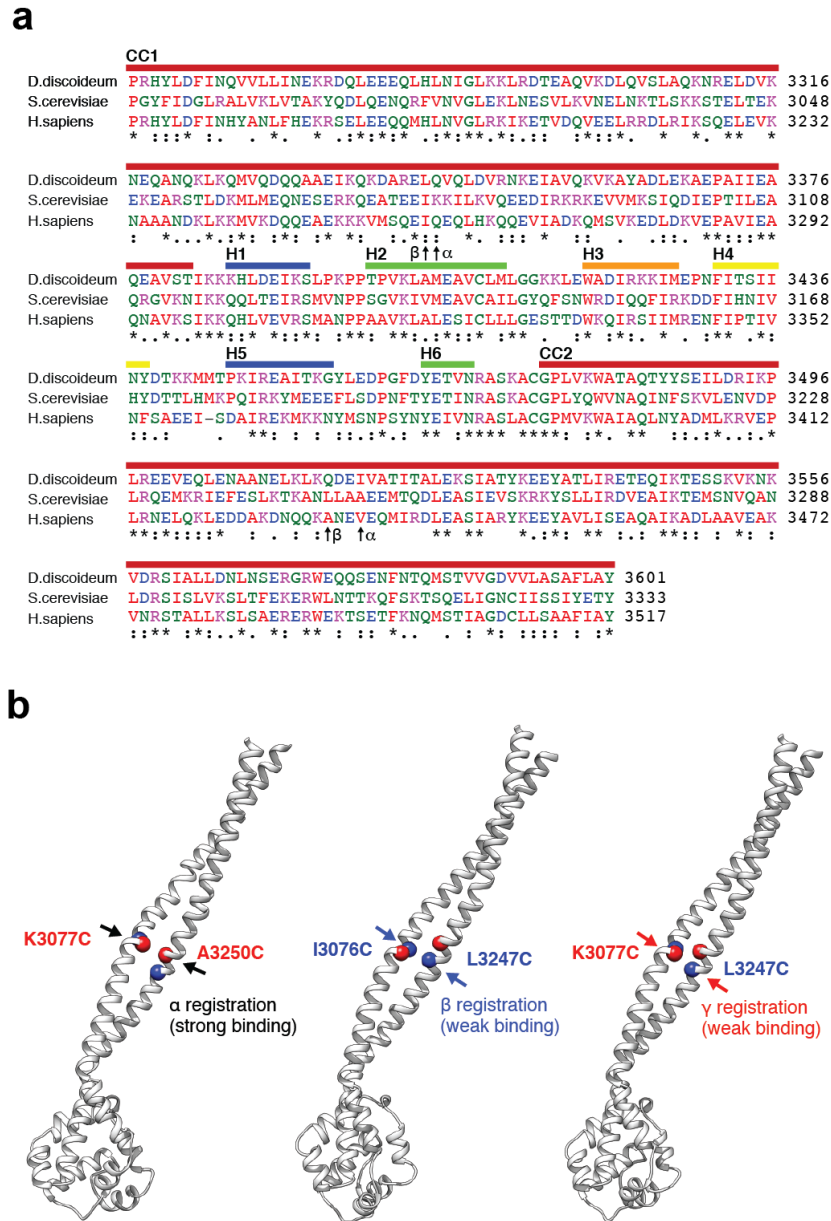
To determine $\epsilon(F)$, we have to evaluate $P(F)$ and $S(F)$. An estimator for these quantities has been suggested by Dudko and coworkers⁷, based on bin size-dependent histograms. To improve statistics and to reduce the effects of bin size on the transformation of unbinding forces into unbinding rates, we are estimating $P(F)$ and $S(F)$ by applying a kernel density estimator to the measured unbinding forces using the statistical toolbox of MATLAB. Because the Dudko method is very sensitive to extreme large outliers, we only consider the unbinding events that lie within

the 99% area of the probability distribution of the measured data. In addition, the detection limit of our unbinding-force measurements is on the order of 0.3 pN. We therefore set the lower limit for the force range we evaluate to 0.5 pN.

A comparison between the histogram-based method, which takes all measured unbinding forces including extreme outliers into account, and the method using kernel density estimators (KDE), shows that for smaller bin sizes the probability density functions (PDFs) of both methods agree better and that both methods result in very similar force-dependent average unbinding rates. However, while the unbinding rates derived from the histogram-based method start to oscillate for increasing forces, the kernel density-based method results in a smooth progression of the unbinding rate with force.

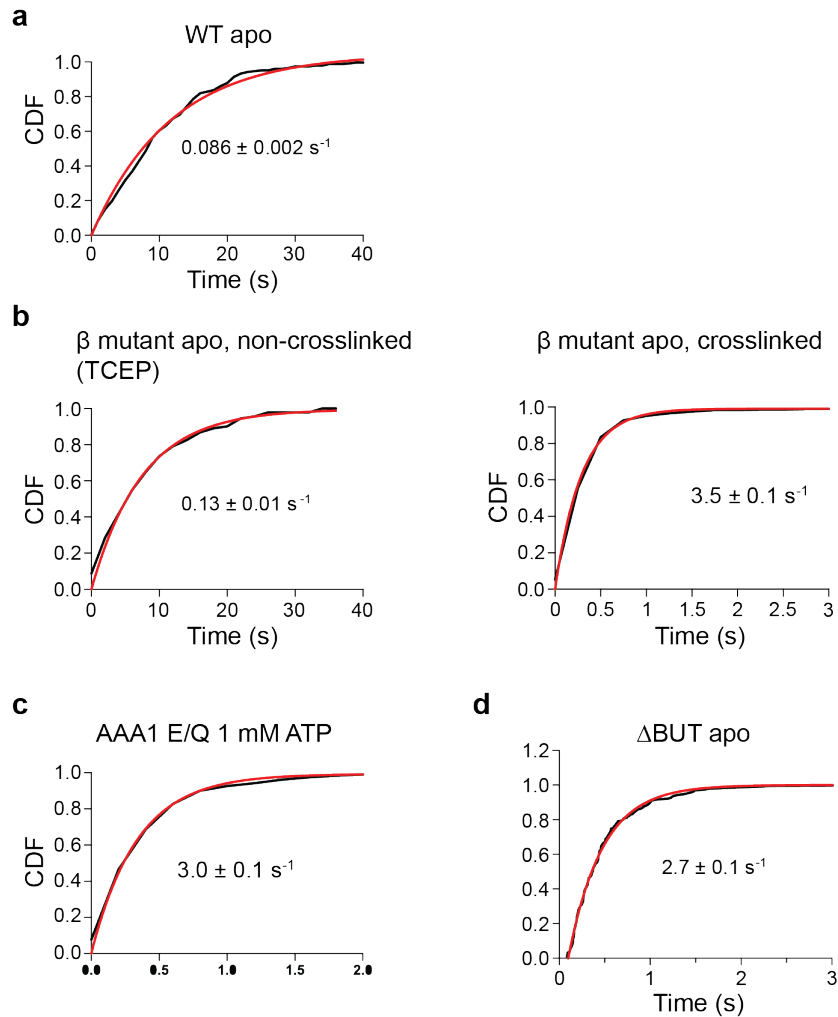
To determine the force-dependent unbinding rates and the associated confident intervals (CIs), we wrote a MATLAB routine that uses the measured unbinding forces (to calculate unbinding rates) and the measured slopes (in pN/s) and the corresponding unbinding forces (to determine the force-dependent loading rates) as inputs. The 95% CIs were estimated by bootstrapping 4000 data sets containing two input data subsets, one resampled from the measured unbinding forces and one resampled from the measured slopes. The resampled data sets always had the same number of elements as the measured data sets. For each of the 4000 resampled data sets, we applied our MATLAB routine to determine the force-dependent loading rates and the force-dependent unbinding rates. The 95% CIs of the 4000 unbinding rates were obtained by estimating the area under the probability distribution with the MATLAB kernel density estimator.

Supplementary Figures:

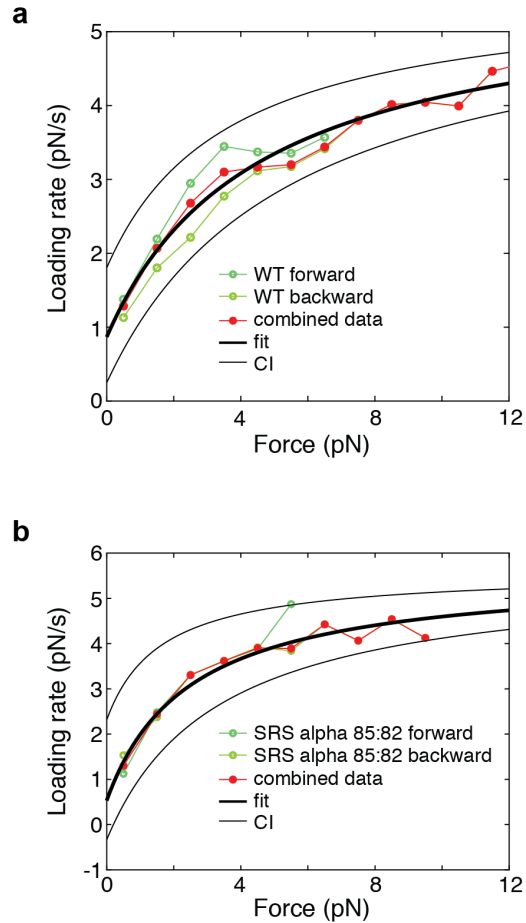


Supplementary Figure 1 Alignment of stalk and MTBD sequences and structures of the distal part of the stalk and MTBD in the strong, weak and intermediate MT-binding states. (a) Alignment of stalk and MTBD sequences from *Dictyostelium discoideum* (D. discoideum), *Saccharomyces*

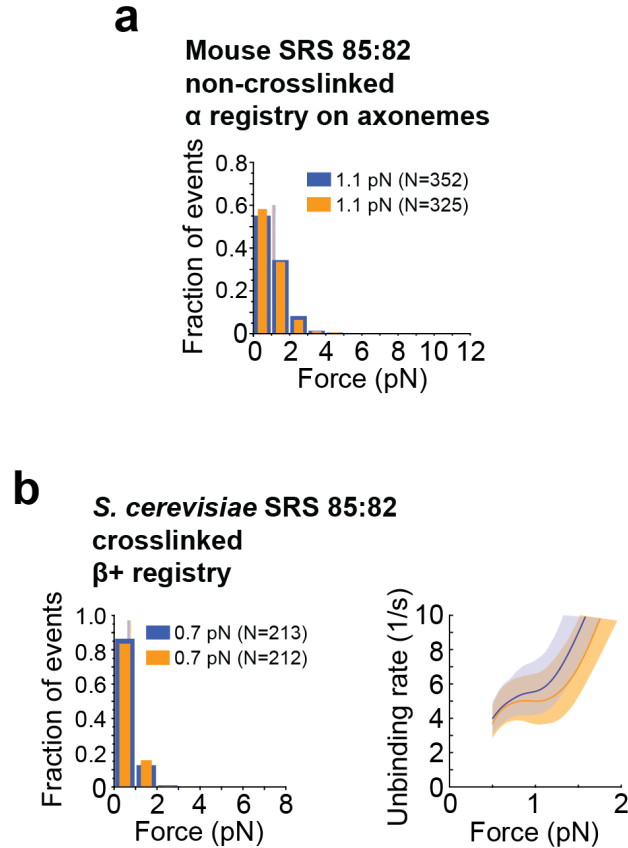
cerevisiae (*S. cerevisiae*), and *Homo sapiens* (*H. sapiens*) cytoplasmic dynein. The positions of the cysteine mutations are indicated. The alignment was generated using Clustal Omega. **(b)** Structures of the distal one-half portion of the stalk helices and MTBD in the strong (α), weak (β), and intermediate (γ) MT-binding states created using the morphed structures described in the Supplementary Note 1.



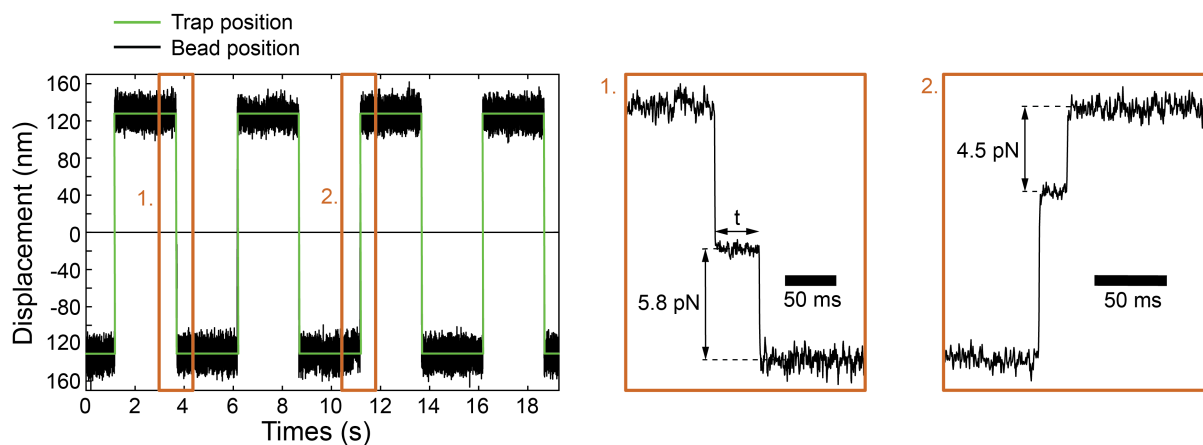
Supplementary Figure 2 Zero-load unbinding rates of Cy3-tagged WT and mutant dynein motor domains obtained from the analysis of the experimental CDFs of MT-bound lifetimes measured via TIRF microscopy. Fitting theoretical CDFs (red curves) derived from an exponential decay function to the experimental cumulative probabilities (black curves) yields the unbinding rate k for each motor construct (mean \pm SEM). **(a)** WT dynein, Dyn1_{331kDa}, in the absence of nucleotides (apo) ($N = 220$). **(b)** Non-crosslinked β -mutant, Dyn1_{331kDa}- β + TCEP (left) ($N = 91$), and cross-linked β -mutant, Dyn1_{331kDa}- β ($N = 351$), both in apo state. **(c)** AAA1 ATP-hydrolysis mutant, AAA1 E/Q Dyn1_{331kDa}, in the presence of 1 mM ATP ($N = 312$). **(d)** Buttress-truncation mutant, Δ BUT-Dyn1_{331kDa}, in the absence of nucleotides (apo) ($N = 190$). Source data are provided as a Source Data file.



Supplementary Figure 3 Force-dependent loading rates for the WT motor, Dyn1_{331kDa} (**a**) and the SRS- α stalk-MTBD construct with the cross-linked stalk helices (**b**) under MT plus- and minus-end-directed loading, determined as described in Supplementary Note 6. The data sets for MT plus- and minus-end-directed loading for each construct coincide and can be combined to calculate an average loading rate (red dots). The force-dependent average loading rate of the WT motor is fit to the rational function, $r(F) = 5.6 \text{ pN s}^{-1}(F + 0.70 \text{ pN})/(4.5 \text{ pN} + F)$ (black line in part *a*). The average loading rate of the SRS construct (red dots in *b*) is fit to $r(F) = 5.6 \text{ pN s}^{-1}(F + 0.23 \text{ pN})/(2.47 \text{ pN} + F)$ (black line in *b*). The 95% confidence intervals are given by MATLAB's fit function. Source data are provided as a Source Data file.

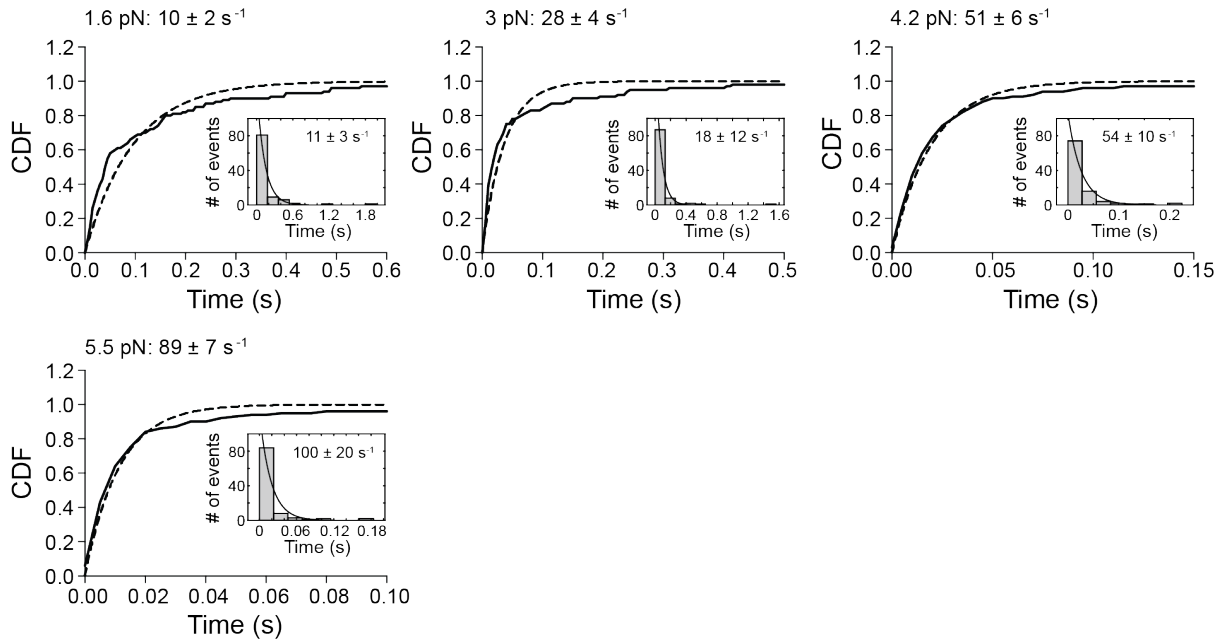


Supplementary Figure 4 Unbinding-force behaviors of SRS-stalk-MTBD constructs. **(a)** Normalized histograms of primary forward and backward unbinding forces for the SRS 85:82 construct with the mouse stalk helices (a.a. 3019-3309) fused in the non-crosslinked α -registry measured on axonemes, with mean values noted (95% CIs [1.1, 1.2] and [1.0, 1.2] pN), estimated by bootstrapping 4,000 samples). **(b)** As in *a* but for the SRS 85:82 construct with the *S. cerevisiae* stalk helices (a.a. 3019-3309) fused in the α -registry and cross-linked (I3076C, L3247C) in the β -registration (95% CIs [0.6, 0.7] and [0.7, 0.8] pN). Source data are provided as a Source Data file.

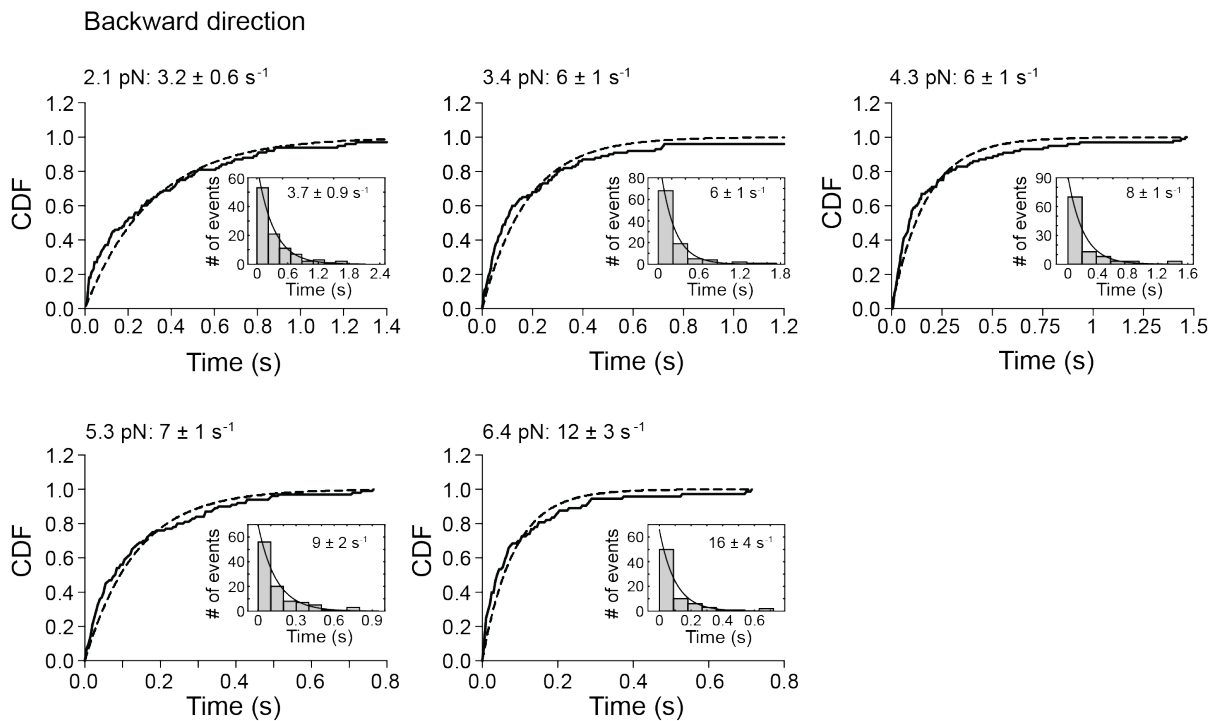


Supplementary Figure 5 Oscillatory trapping assay used by Cleary and co-workers². A representative trace of trap (green) and bead position (black) is shown on the left. The two trace segments on the right correspond to the data marked by the rectangular boxes on the left. The first segment shows a binding event of lifetime t that occurs while the bead moves along the long MT axis toward the MT plus-end, while the second segment shows a binding event while the bead moves to the MT minus-end. As a result of the binding of the SRS construct to the MT surface, the bead stops following the moving trap, during which time the SRS construct experiences a constant load given by the momentarily maintained bead-trap separation times the spring constant. Once the SRS construct detaches, the bead quickly follows the trap to its new position (see Supplementary Note 3 for a detailed description of the oscillatory assay and Supplementary Note 4 for a theoretical analysis of the generated loading rates).

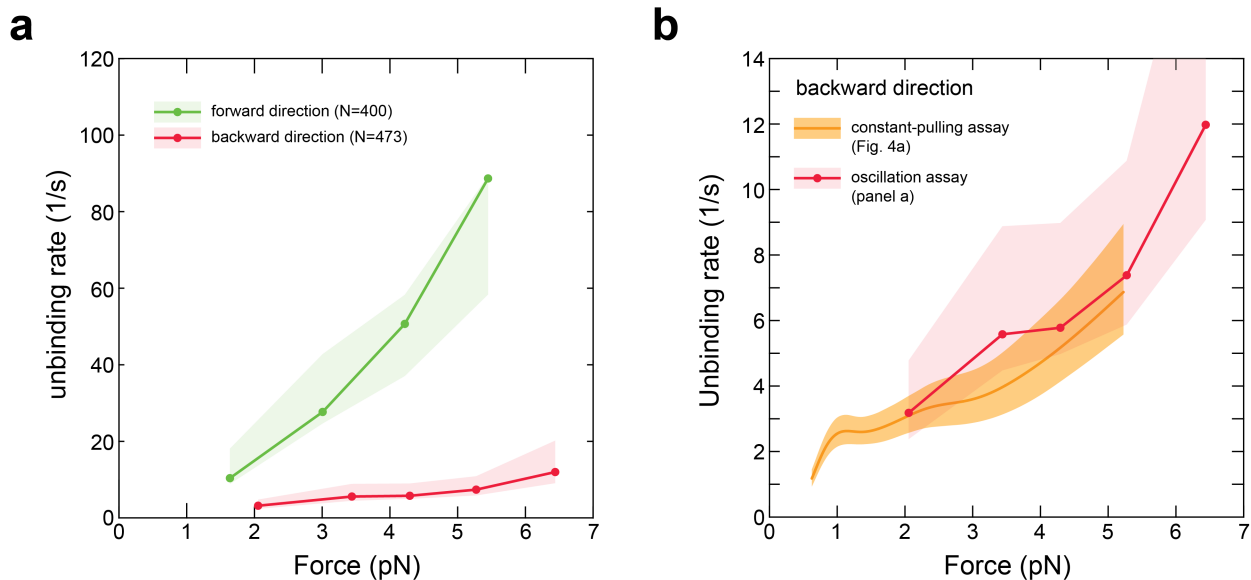
a Forward direction



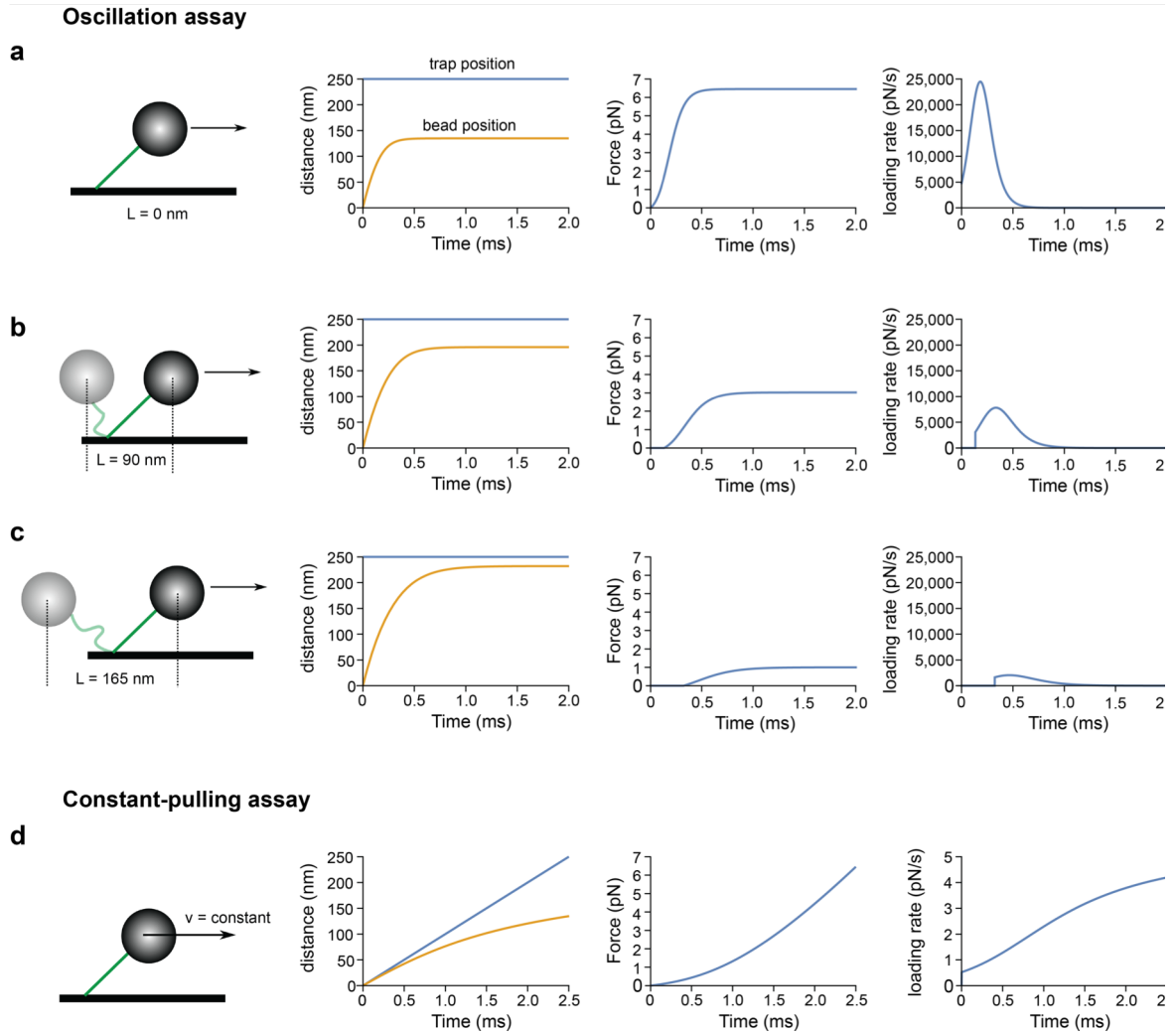
b Backward direction



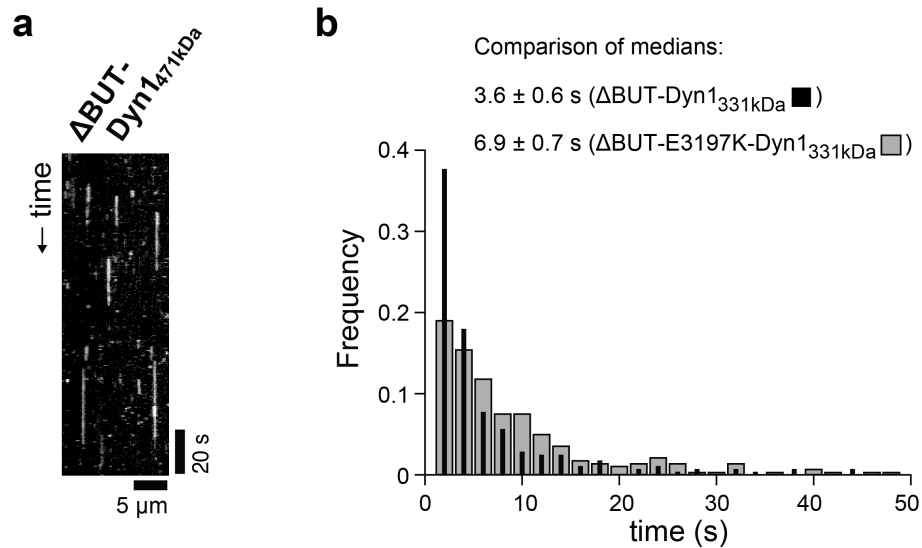
Supplementary Figure 6 Force-dependent unbinding rates of the SRS 85:82 construct with the non-crosslinked mouse stalk helices (a.a. 3019-3309) fused in the α -registry (SRS- α stalk-MTBD) measured with the oscillatory trap assay used by Cleary and co-workers². (**a** and **b**) Cumulative probabilities of the measured bond lifetimes obtained under forward (panel *a*) and backward loading (panel *b*) following a sorting of the lifetimes by force and a binning of the data every 100 data points (the cumulative probabilities of the lifetimes in each force bin are shown). Fitting a theoretical cumulative distribution function (CDF) derived from an exponential decay function to the experimental cumulative probabilities (dashed curves) yields the unbinding rate k for each force value (depicted in Supplementary Fig. 7a). The given error (SE) of each unbinding rate was calculated by bootstrapping 200 samples (see Supplementary Note 3 for a detailed description of the processing and analysis of the oscillatory trap data). For comparison, we also show the unbinding rates that result from fitting the histograms of the measured lifetimes of each force bin to an exponential function as done by Cleary and co-workers². Here, we calculated the optimal bin size using the MATLAB `calcnbins()` function (setting ‘middle’). The resulting rates agree with the rates obtained via CDF analysis within the estimated errors. As the CDF analysis provides a bin size-independent analysis, we plot the unbinding rates obtained from the CDF analysis in Supplementary Fig. 7a. Source data are provided as a Source Data file.



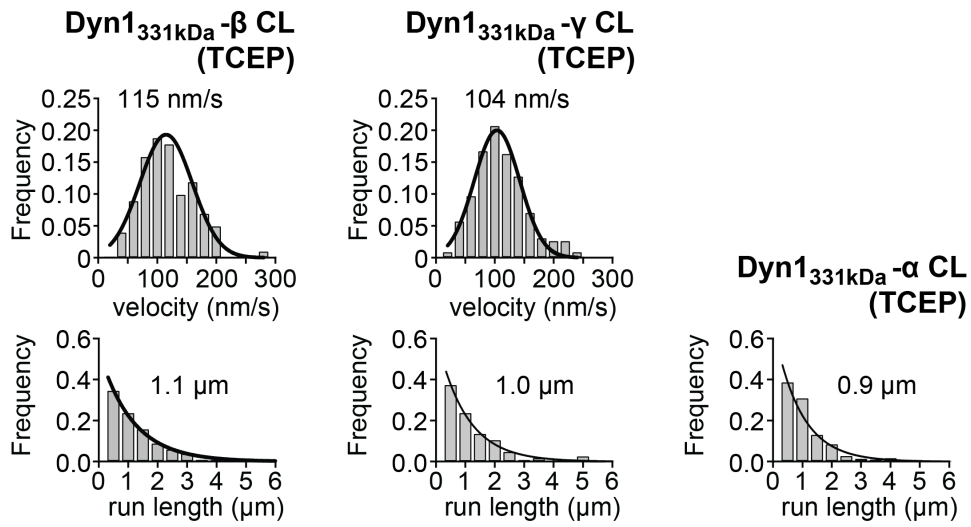
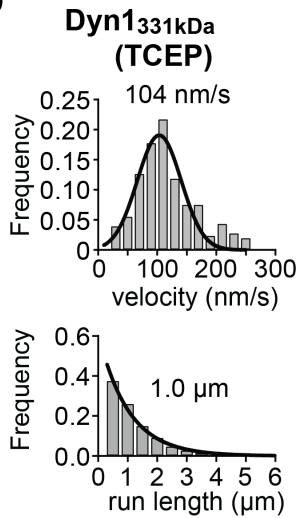
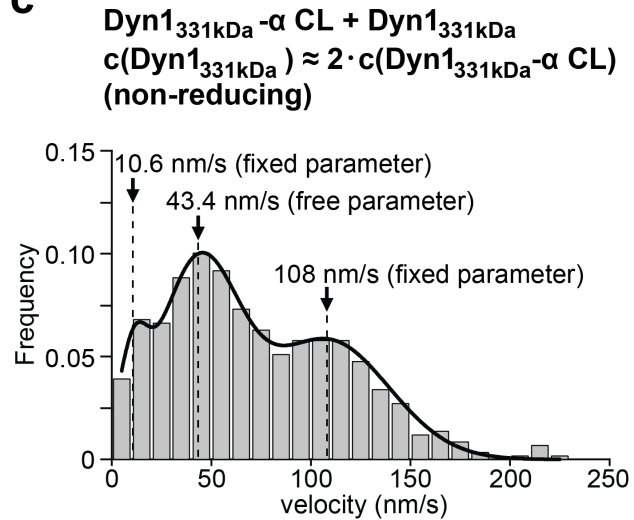
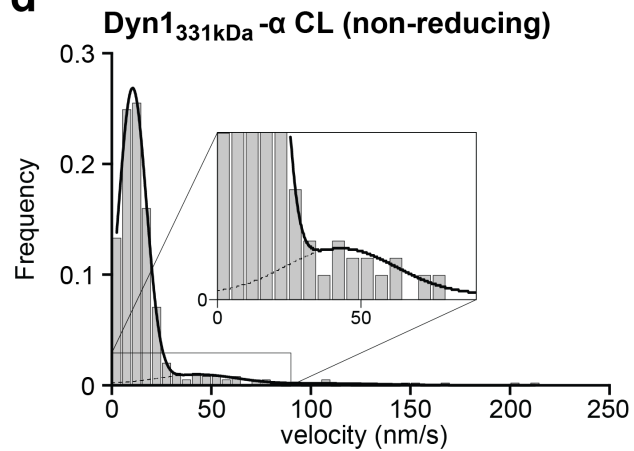
Supplementary Figure 7 Unbinding rate vs. force for the SRS- α stalk-MTBD construct. (a) Unbinding rate vs. force measured with the oscillatory assay used by Cleary and co-workers² (see Supplementary Fig. 6 for the data underlying the depicted values and Supplementary Note 3 for a detailed description of the generation and analysis of the oscillatory trap data). The shaded areas are 95% CIs for the mean rates, estimated by bootstrapping. Our analysis shows that the oscillatory trap assay results in an anisotropic detachment rate as previously reported by Cleary and co-workers². (b) Unbinding rate as a function of backward load (applied along the long MT axis) measured with the oscillatory trap assay (panel a) and the constant-pulling assay used herein (Fig. 4a).



Supplementary Figure 8 Theoretical analysis of bead position, force and loading rate generated by the oscillatory and constant-pulling assays as discussed in Supplementary Note 4.



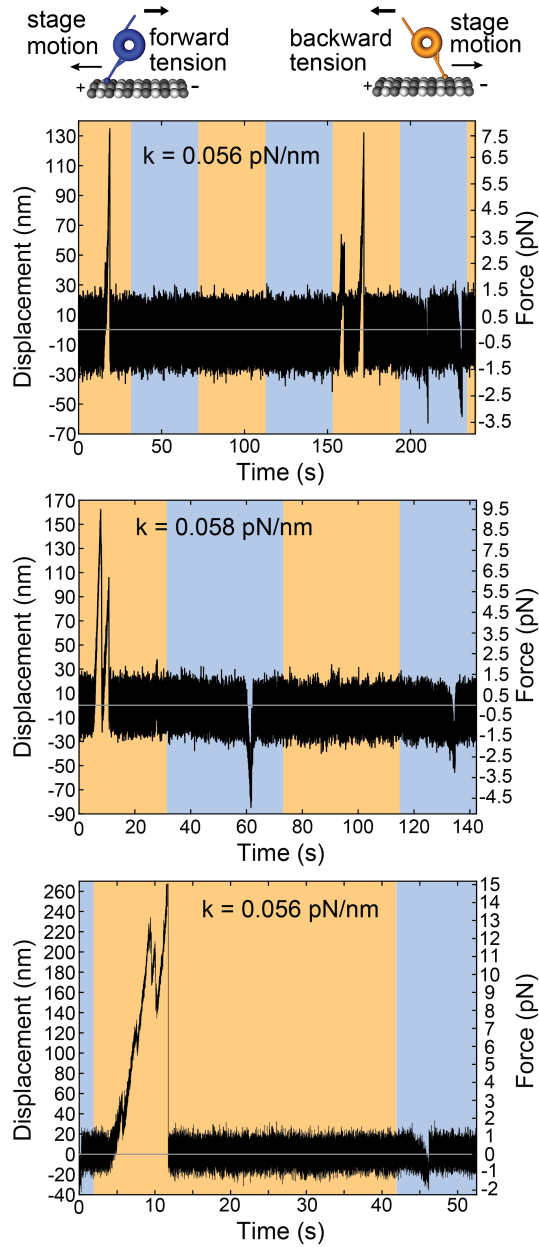
Supplementary Figure 9 Motility analysis of the homodimeric motor, Δ BUT-Dyn1_{471kDa}, and comparison of the MT-bound lifetimes of the antibody-dimerized motors, Δ BUT-Dyn1_{331kDa} and Δ BUT-E3197K-Dyn1_{331kDa}. **(a)** Kymograph analysis reveals that Δ BUT-Dyn1_{471kDa} only shows non-motile interactions. **(b)** Plotting the histograms of the MT-bound lifetimes of the Δ BUT-Dyn1_{331kDa} and Δ BUT-E3197K-Dyn1_{331kDa} motors acquired in the presence of 1 mM ATP reveals that the increased ionic strength between MTs and the MTBD via the E3197K mutation increases the MT-bound lifetime of the non-motile binding events: 3.6 ± 0.6 s (median \pm SEM; $N = 262$) [Δ BUT-Dyn1_{331kDa}] vs. 6.9 ± 0.7 s⁻¹ (median \pm SEM; $N = 257$) [Δ BUT-E3197K-Dyn1_{331kDa}] (source data are provided as a Source Data file).

a**b****c****d**

Supplementary Figure 10 Velocity and processivity analyses of antibody-dimerized mutant and WT motors under reducing (non-cross-linking) and non-reducing (cross-linking) conditions. **(a)** TIRF-based motility experiments conducted in the presence of 2 mM TCEP demonstrate that the cross-linking of the stalk helices is fully reversible and that the mutant motors, Dyn1_{331kDa}-β CL, Dyn1_{331kDa}-γ CL, Dyn1_{331kDa}-α CL, are as enzymatically active under reducing conditions as WT Dyn1_{331kDa}. Fitting the acquired velocity and run length histograms with Gaussian and first-order decay functions yields mean velocities of 115 ± 10 nm/s (mean \pm SEM; $N = 101$) for Dyn1_{331kDa}-β CL and 104 ± 3 nm/s (mean \pm SEM; $N = 227$) for Dyn1_{331kDa}-γ CL (see Fig. 7b in the main text for the mean velocity of the Dyn1_{331kDa}-α CL motor in the presence of TCEP). Characteristic run lengths were 1.1 ± 0.1 μm (\pm SEM; $N = 101$) for Dyn1_{331kDa}-β CL, 1.0 ± 0.1 μm (\pm SEM; $N = 227$) for Dyn1_{331kDa}-γ CL, and 0.9 ± 0.1 μm (\pm SEM; $N = 281$) for Dyn1_{331kDa}-α CL. These values are similar to the values of the WT motor both under non-reducing (Fig. 7a, top right) and reducing (panel b) conditions. **(b)** Kymograph-based analysis of the antibody-dimerized WT Dyn1_{331kDa} motor under reducing conditions (2 mM TCEP) results in a velocity (104 ± 2 nm/s [\pm SEM; $N = 253$]) and run length (1.0 μm \pm 0.1 [\pm SEM; $N = 253$]), which are similar to the velocity and run length of the antibody-dimerized WT motor measured under non-reducing conditions (Fig. 6a, top right). This demonstrates that the cross-linking conditions do not affect the function of the WT motor. **(c)** Velocity histogram ($N = 594$) of populations of antibody-dimerized homodimeric (Dyn1_{331kDa}-α CL or WT Dyn1_{331kDa}) and heterodimeric motors (Dyn1_{331kDa}-α CL motor domain coupled to a WT Dyn1_{331kDa} motor domain) created under non-reducing (cross-linking) conditions by combining the Dyn1_{331kDa}-α CL mutant with a two-fold higher concentration of WT Dyn1_{331kDa}. The velocity of the heterodimers (43.4 ± 1.2 nm/s [\pm SEM; $N_{\text{heterodimer}} = 285$]) was determined by

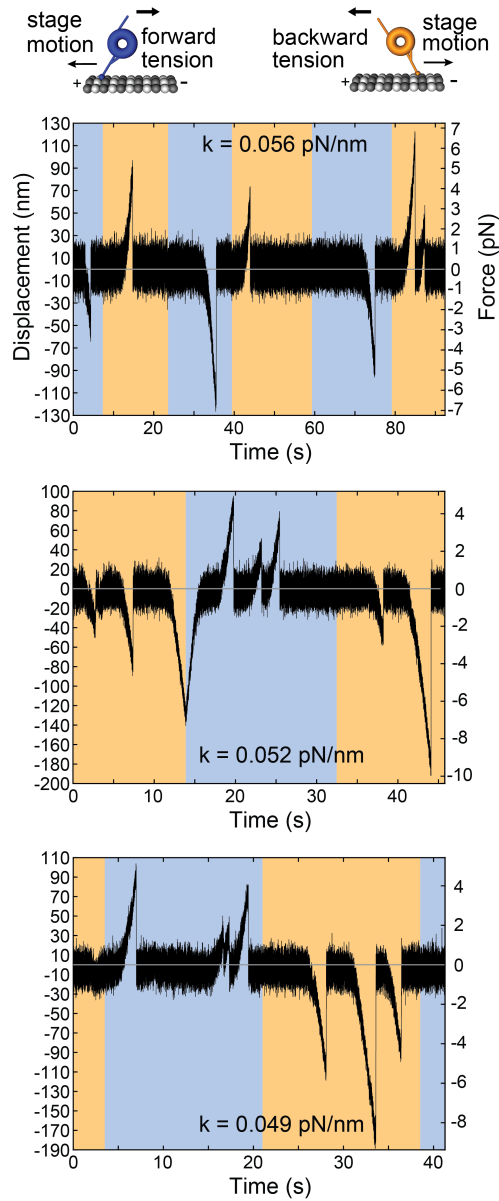
fitting the histogram to three Gaussian functions. The velocity peaks of the homodimeric Dyn1_{331kDa}- α CL motor (10.6 ± 1.2 nm/s [\pm SEM; $N_{\text{mutant_homodimer}} = 36$]; Fig. 7b, top right) and the homodimeric WT Dyn1_{331kDa} motor (108 ± 2 nm/s [\pm SEM; $N_{\text{WT_homodimer}} = 273$]; Fig. 7a, top right) were used as fixed parameters, while the mean velocity of the heterodimer was a free parameter. The standard deviation of the mean velocity of the Dyn1_{331kDa}- α CL homodimer (7 nm/s), taken from the fit of the Gaussian function to the velocity peak of Dyn1_{331kDa}- α CL under cross-linking conditions (Fig. 7b, top right), was also taken as a fixed parameter. The number of events for each dimeric motor species was determined from the relative surface areas of each Gaussian function; the calculated 6, 48 and 46% contributions of the Dyn1_{331kDa}- α CL homodimer, the Dyn1_{331kDa}- α CL-Dyn1_{331kDa} heterodimer and the Dyn1_{331kDa} homodimer, are reasonably close to the theoretically expected contributions of 10, 44, and 46% assuming the WT Dyn1_{331kDa} concentration is twice as high (2.1x) as the concentration of the Dyn1_{331kDa}- α CL mutant. **(d)** Fitting the velocity histogram of the Dyn1_{331kDa}- α CL mutant motors acquired under cross-linking conditions (Fig. 7b, top right) with two Gaussian functions, one centered at 10.6 nm/s (free parameter) and another at 43.4 nm/s (the mean velocity and its standard deviation, SD = 20.2 nm/s, obtained from the analysis in panel c, were taken as fixed parameters), allows the estimation of the fractions of Dyn1_{331kDa}- α CL homodimers, Dyn1_{331kDa}- α CL-Dyn1_{331kDa}- α heterodimers, and Dyn1_{331kDa}- α homodimers (see Supplementary Note 2 for more information). Source data are provided as a Source Data file.

Wild Type Apo, no DTT (purified and studied under non-reducing conditions)



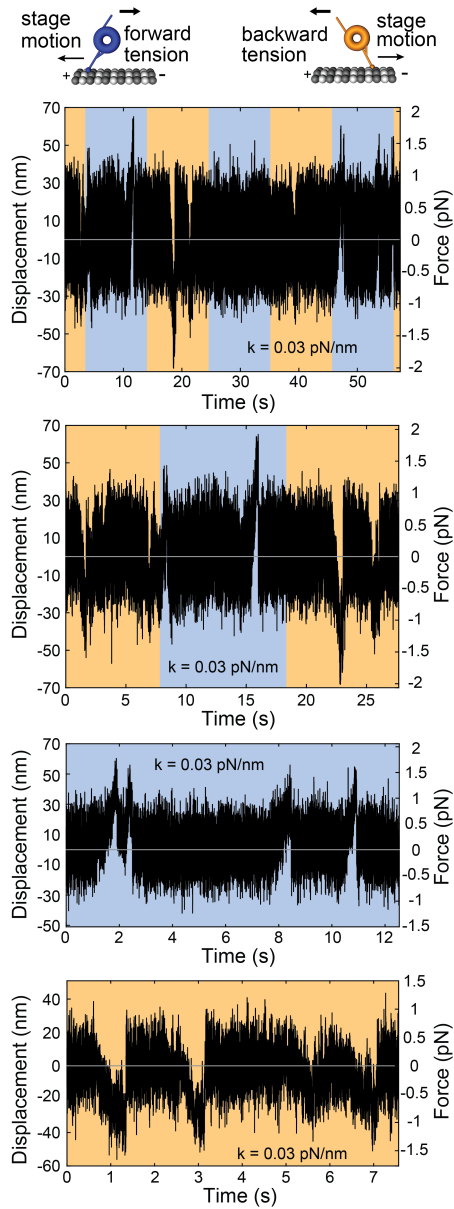
Supplementary Figure 11 Unbinding-force experiments (force/position vs. time) in the absence of nucleotide for the WT motor domain, Dyn1_{331kDa} (VY137). The illustration represents the configuration for backward vs. forward tension. Orange (blue) shaded areas show periods of applied rearward (forward) tension.

α -mutant Apo, no DTT (purified and studied under non-reducing conditions)



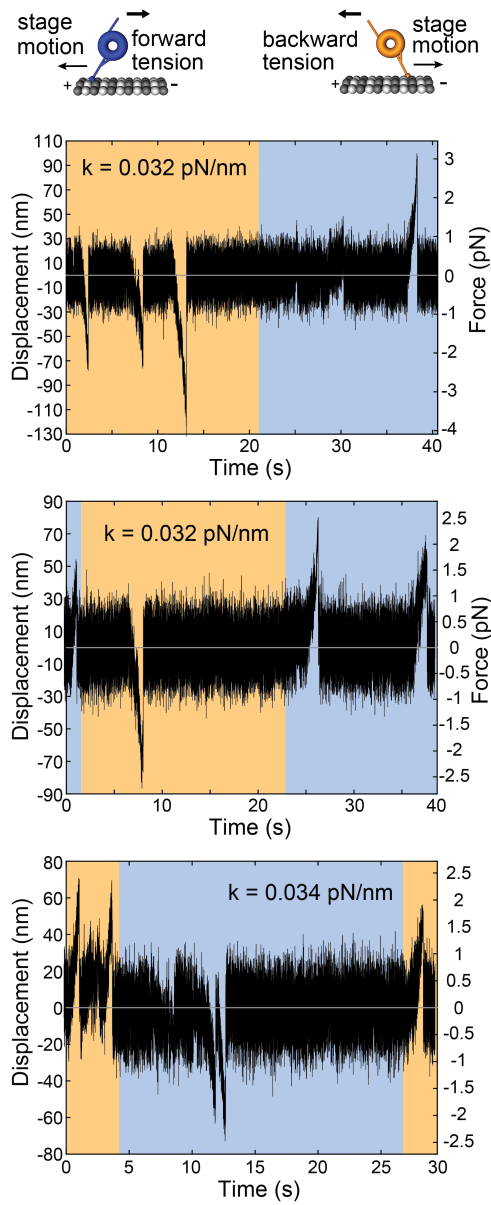
Supplementary Figure 12 Unbinding-force experiments (force/position vs. time) in the absence of nucleotide for the α -mutant motor domain with the cross-linked stalk helices, Dyn1_{331kDa}- α CL. The illustration represents the configuration for backward vs. forward tension. Orange (blue) shaded areas show periods of applied rearward (forward) tension.

β -mutant Apo, no DTT (purified and studied under non-reducing conditions)



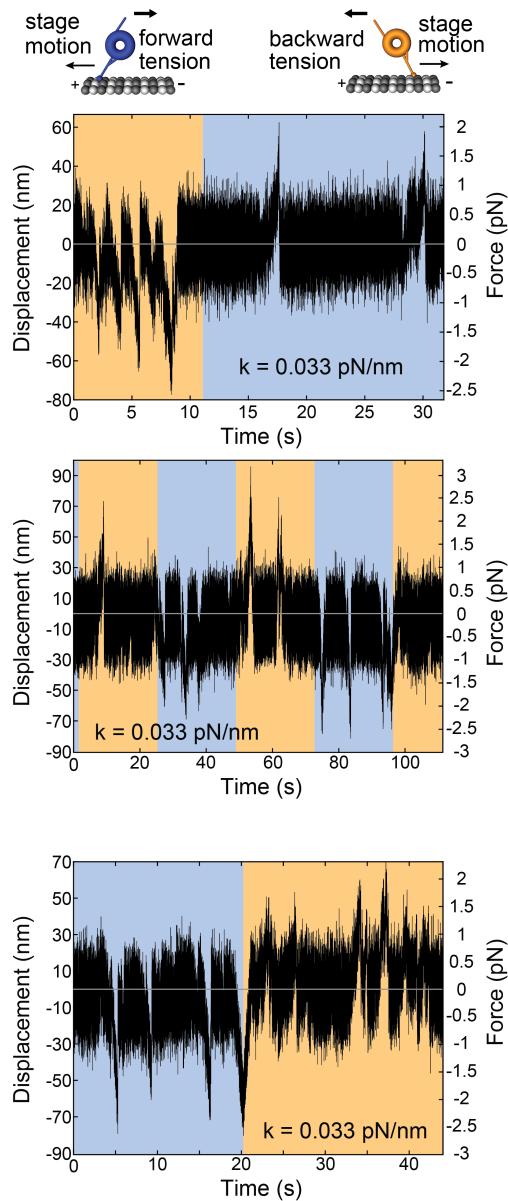
Supplementary Figure 13 Unbinding-force experiments (force/position vs. time) in the absence of nucleotide for the β -mutant motor domain with the cross-linked stalk helices, Dyn1_{331kDa}- β CL. The illustration represents the configuration for backward vs. forward tension. Orange (blue) shaded areas show periods of applied rearward (forward) tension.

γ -mutant Apo, no DTT (purified and studied under non-reducing conditions)



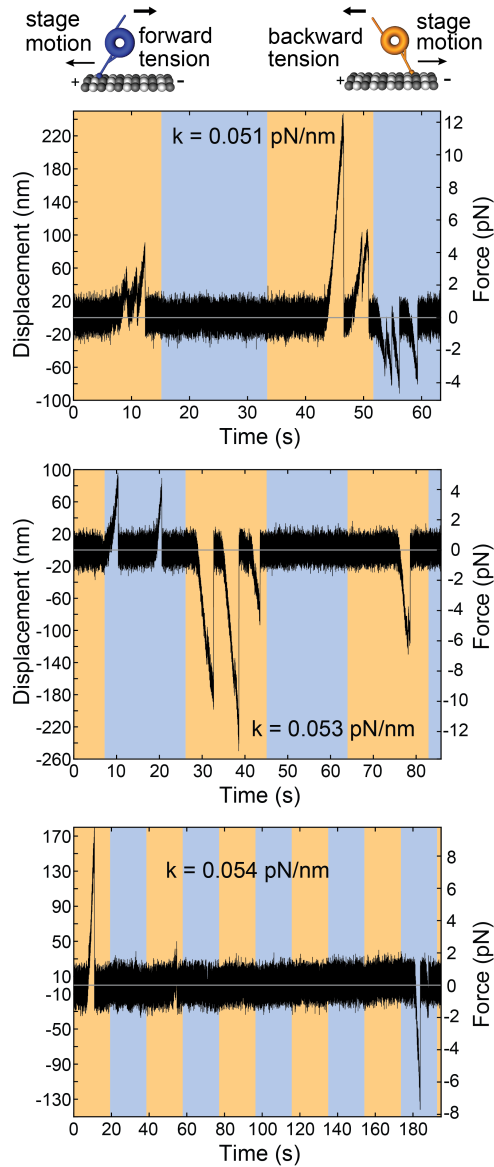
Supplementary Figure 14 Unbinding-force experiments (force/position vs. time) in the absence of nucleotide for the γ -mutant motor domain with the cross-linked stalk helices, Dyn1_{331kDa}- γ CL. The illustration represents the configuration for backward vs. forward tension. Orange (blue) shaded areas show periods of applied rearward (forward) tension.

AAA1 E/Q 1 mM ATP, no DTT (purified and studied under non-reducing conditions)



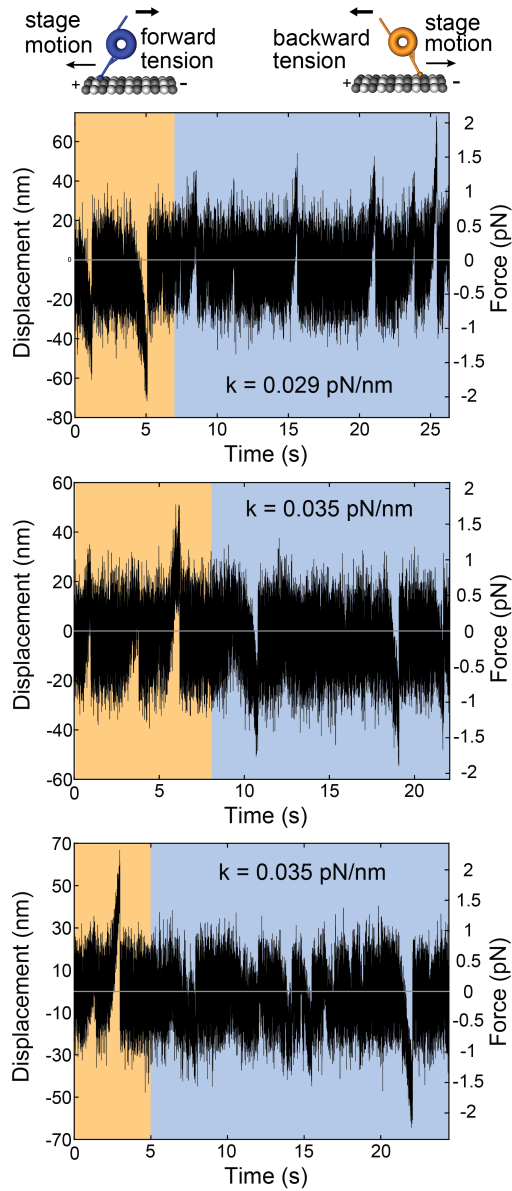
Supplementary Figure 15 Unbinding-force experiments (force/position vs. time) in the presence of 1 mM ATP for the AAA1 E/Q mutant motor domain. The illustration represents the configuration for backward vs. forward tension. Orange (blue) shaded areas show periods of applied rearward (forward) tension.

**α -mutant AAA1 E/Q 1 mM ATP, no DTT
(purified and studied under non-reducing
conditions)**



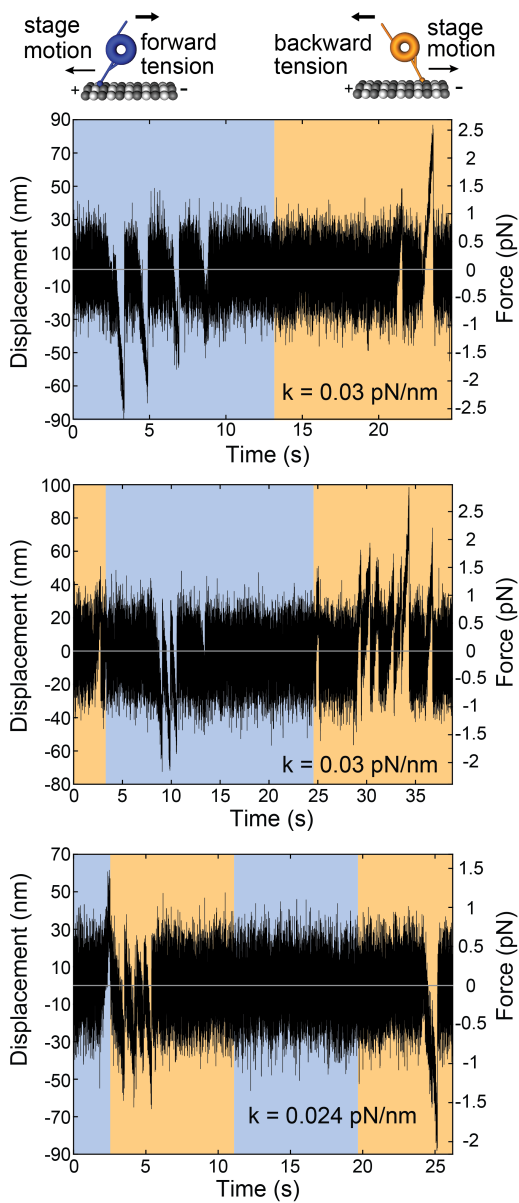
Supplementary Figure 16 Unbinding-force experiments (force/position vs. time) in the presence of 1 mM ATP for the AAA1 E/Q mutant motor domain with the stalk helices cross-linked in the α -registration (AAA1 E/Q Dyn1_{331kDa}- α CL). The illustration represents the configuration for backward vs. forward tension. Orange (blue) shaded areas show periods of applied rearward (forward) tension.

**α -mutant AAA1 E/Q 1 mM ATP, no DTT
+ TCEP**



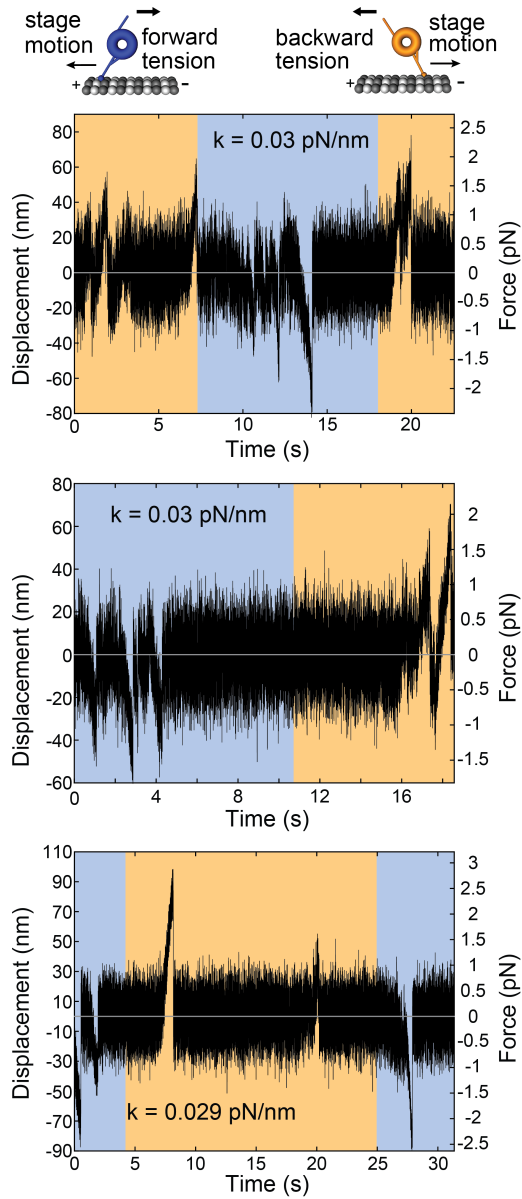
Supplementary Figure 17 Unbinding-force experiments (force/position vs. time) in the presence of 1 mM ATP and 2 mM TCEP for AAA1 E/Q Dyn1_{331kDa}- α CL. The illustration represents the configuration for backward vs. forward tension. Orange (blue) shaded areas show periods of applied rearward (forward) tension.

Δ BUT Apo, no DTT (purified and studied under non-reducing conditions)



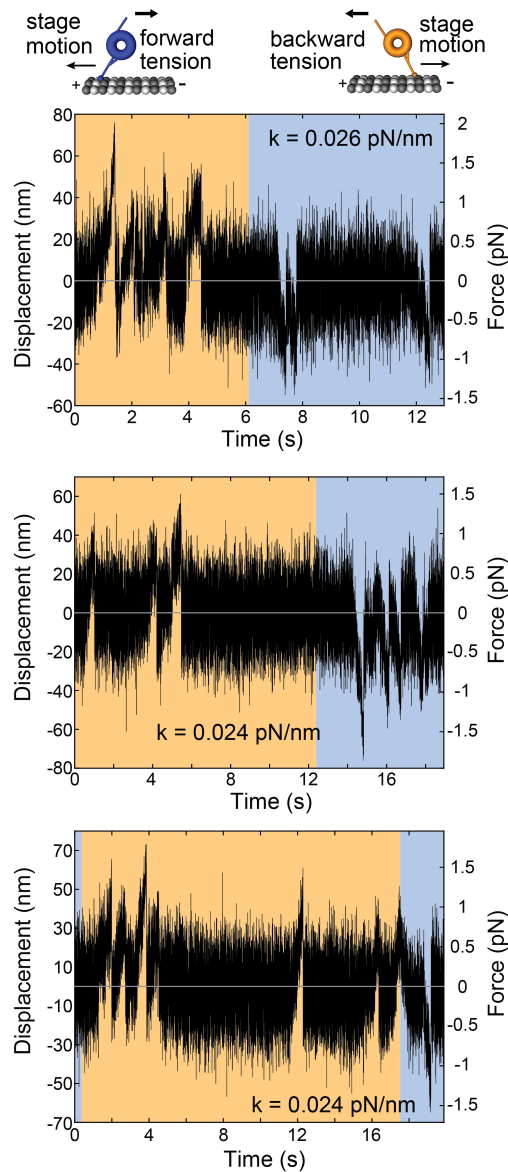
Supplementary Figure 18 Unbinding-force experiments (force/position vs. time) in the absence of nucleotide for the buttress-truncation mutant Δ BUT-Dyn1₃₃₁KD. The illustration represents the configuration for backward vs. forward tension. Orange (blue) shaded areas show periods of applied rearward (forward) tension.

F3446E-VY137 Apo, no DTT (purified and studied under non-reducing conditions)



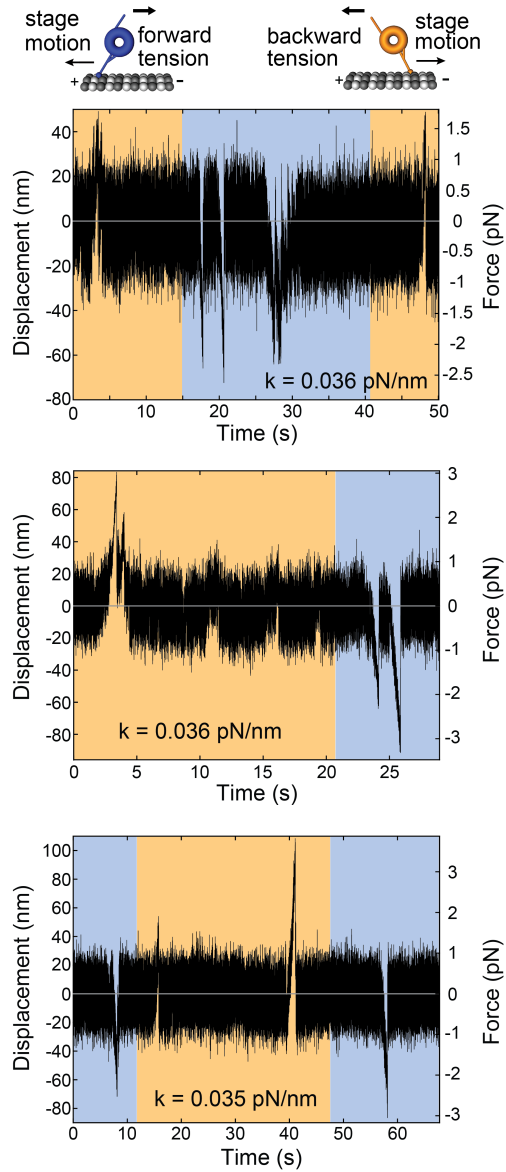
Supplementary Figure 19 Unbinding-force experiments (force/position vs. time) in the absence of nucleotide for the F3446E-Dyn1_{331kDa} mutant motor domain. The illustration represents the configuration for backward vs. forward tension. Orange (blue) shaded areas show periods of applied rearward (forward) tension.

**F3446E-AAA3 E/Q 1 mM ATP
(purified and studied under
non-reducing conditions)**



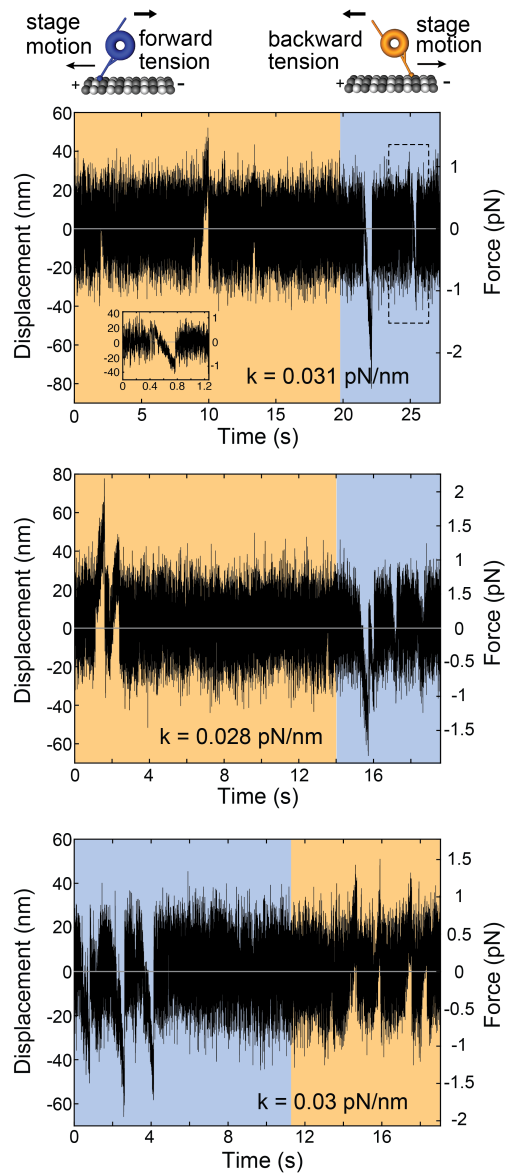
Supplementary Figure 20 Unbinding-force experiments (force/position vs. time) in the presence of 1 mM ATP for the F3446E-AAA3 E/Q CT-GFP mutant motor domain. The illustration represents the configuration for backward vs. forward tension. Orange (blue) shaded areas show periods of applied rearward (forward) tension.

***S. cerevisiae* SRS 89:82**
(non-crosslinked β + registry, studied
under non-reducing conditions)



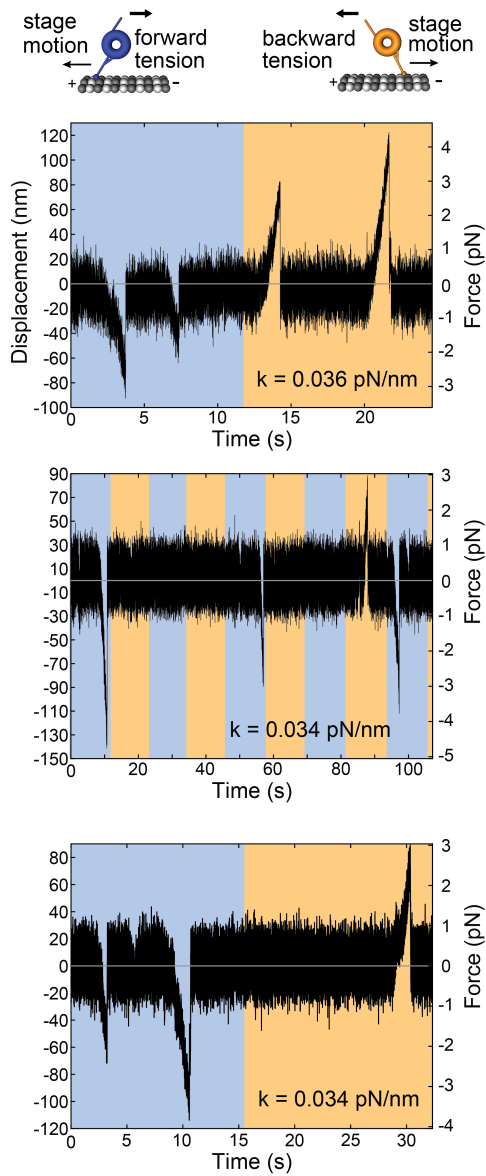
Supplementary Figure 21 Unbinding-force experiments (force/position vs. time) for the SRS- β stalk-MTBD construct with the *S. cerevisiae* stalk-MTBD sequence and non-cross-linked stalk helices. The illustration represents the configuration for backward vs. forward tension. Orange (blue) shaded areas show periods of applied rearward (forward) tension.

***S. cerevisiae* SRS 89:82**
(crosslinked β + registry, studied
under non-reducing conditions)



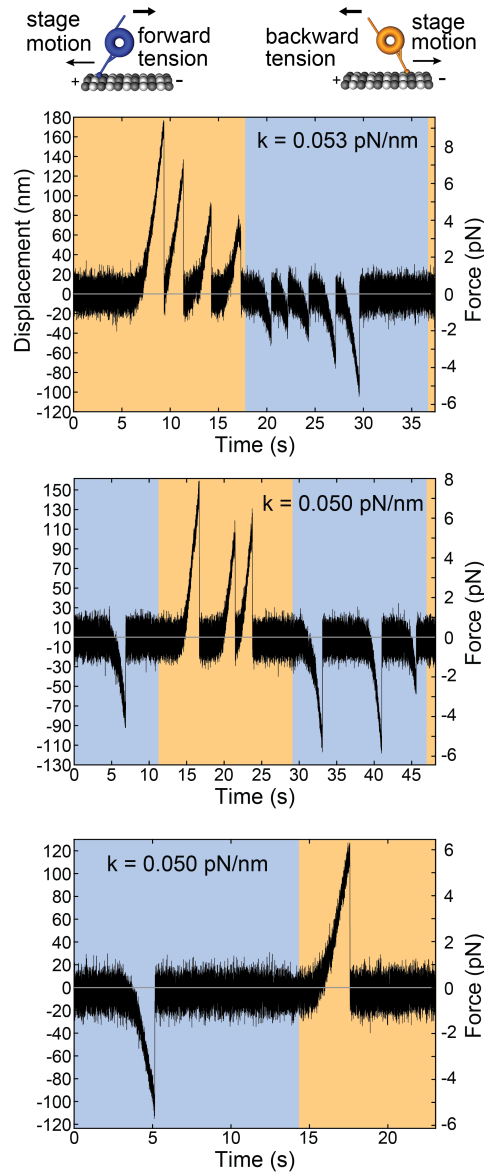
Supplementary Figure 22 Unbinding-force experiments (force/position vs. time) for the SRS- β stalk-MTBD CL construct with the *S. cerevisiae* stalk-MTBD sequence and cross-linked β -registry. The illustration represents the configuration for backward vs. forward tension. Orange (blue) shaded areas show periods of applied rearward (forward) tension.

***S. cerevisiae* SRS 85:82**
(non-crosslinked α registry, studied
under non-reducing conditions)



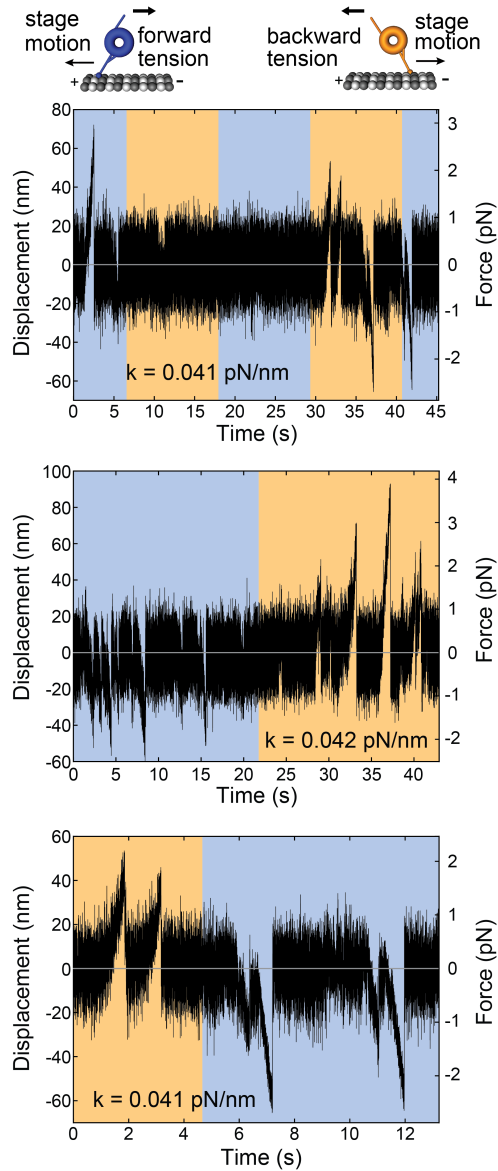
Supplementary Figure 23 Unbinding-force experiments (force/position vs. time) for the SRS- α stalk-MTBD construct with the *S. cerevisiae* stalk-MTBD sequence and non-cross-linked stalk helices. The illustration represents the configuration for backward vs. forward tension. Orange (blue) shaded areas show periods of applied rearward (forward) tension.

***S. cerevisiae* SRS 85:82
(crosslinked α registry, studied
under non-reducing conditions)**



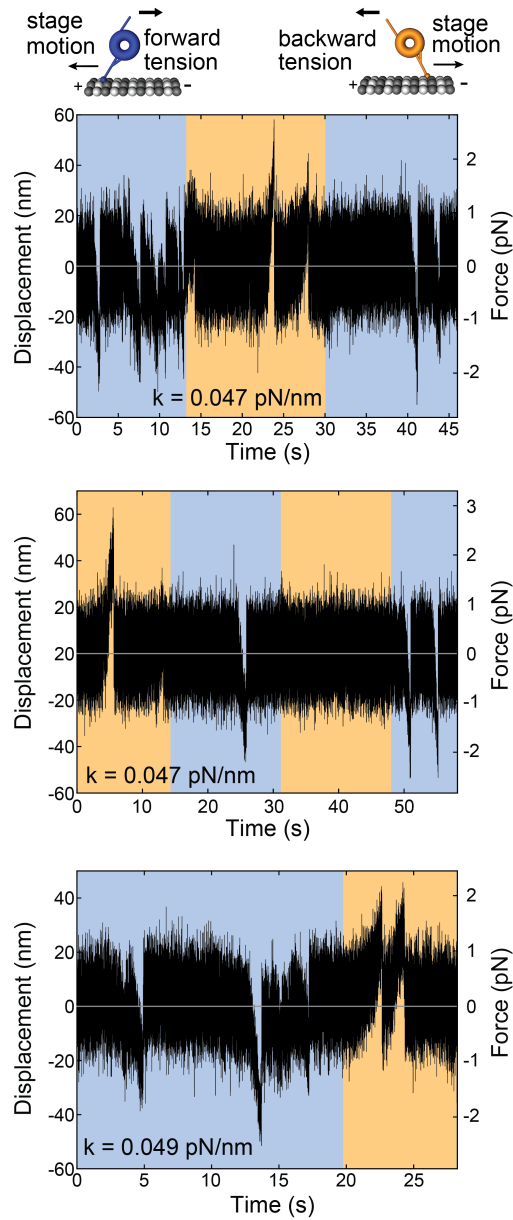
Supplementary Figure 24 Unbinding-force experiments (force/position vs. time) for the SRS- α stalk-MTBD CL construct with the *S. cerevisiae* stalk-MTBD sequence and cross-linked α -registry. The illustration represents the configuration for backward vs. forward tension. Orange (blue) shaded areas show periods of applied rearward (forward) tension.

***S. cerevisiae* SRS 85:82
(crosslinked β^+ registry, studied
under non-reducing conditions)**



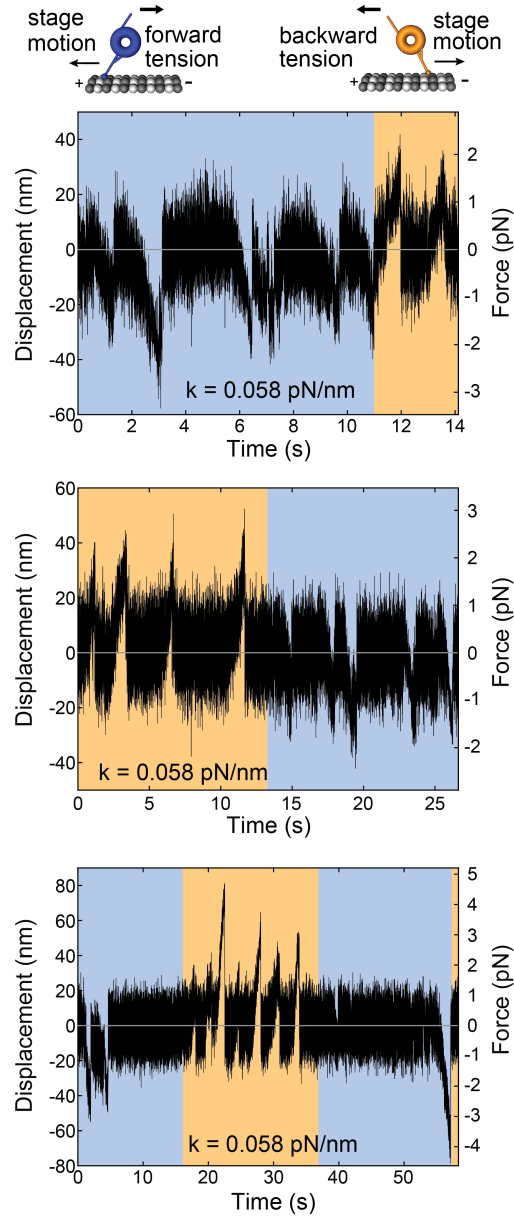
Supplementary Figure 25 Unbinding-force experiments (force/position vs. time) for the SRS- α stalk-MTBD CL construct with the *S. cerevisiae* stalk-MTBD sequence and cross-linked β -registry. The illustration represents the configuration for backward vs. forward tension. Orange (blue) shaded areas show periods of applied rearward (forward) tension.

Mouse SRS 85:82 on MTs
(non-crosslinked α registry, studied
under non-reducing conditions)



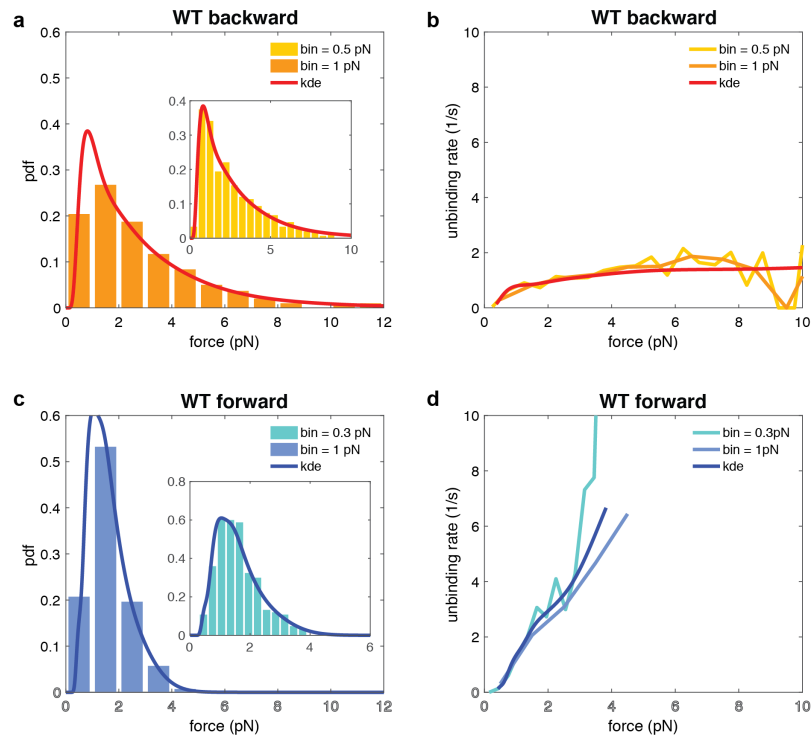
Supplementary Figure 26 Unbinding-force experiments (force/position vs. time) for the mouse SRS- α stalk-MTBD construct with non-cross-linked stalk helices. The illustration represents the configuration for backward vs. forward tension. Orange (blue) shaded areas show periods of applied rearward (forward) tension.

**Mouse SRS 85:82 on axonemes
(non-crosslinked α registry, studied
under non-reducing conditions)**



Supplementary Figure 27 Unbinding-force experiments (force/position vs. time) for the mouse SRS- α stalk-MTBD construct with non-cross-linked stalk helices using axonemes. The illustration represents the configuration for backward vs. forward tension. Orange (blue) shaded areas show periods of applied rearward (forward) tension.

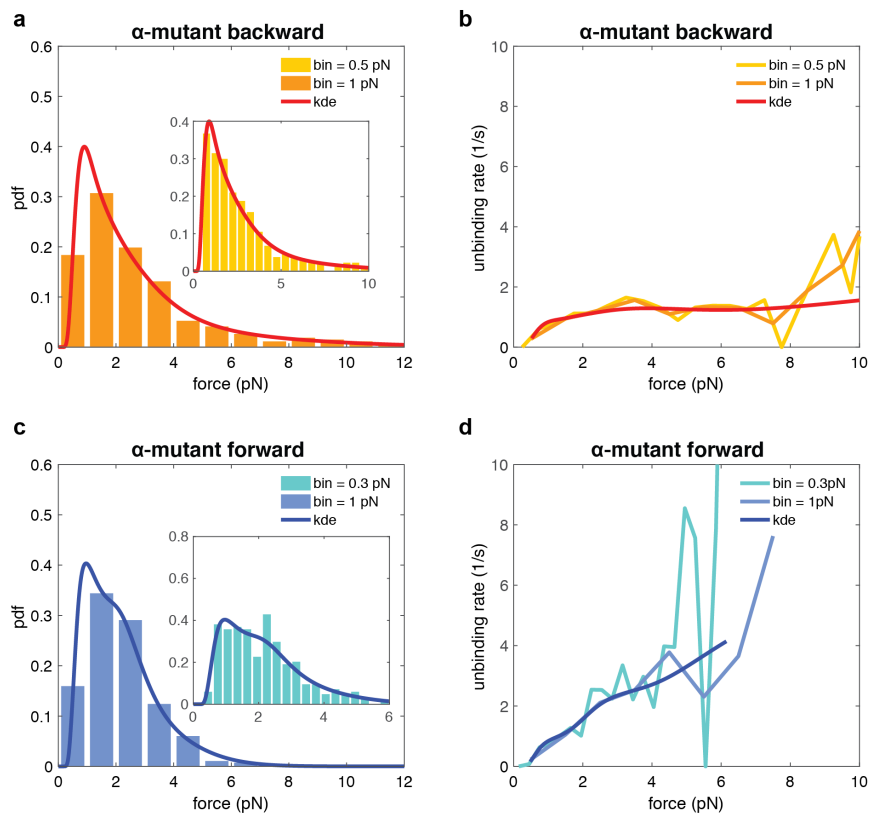
Conversion of WT Apo unbinding-force histograms



Supplementary Figure 28 Comparison of the histogram-based method derived by Dudko and co-workers⁷ with our improved method using kernel-density estimators shown for the WT motor domain, Dyn1_{331kDa}. Both methods determine a probability density function (PDF) from the unbinding force data (*a* and *c*) that is used to calculate the corresponding force-dependent unbinding rates (*b* and *d*). The kernel density estimator (KDE) (solid dark red and blue lines in *a* and *c*) result in a smooth unbinding rates (solid red and dark blue lines in *b* and *d*). The histogram-based method depends on the bin size: increasing the bin size results in an oscillating, non-smooth unbinding rate, because the contour of the histograms no longer reflects accurately the underlying distribution (histograms with larger numbers of bins are shown in the insets of *a* and *c* and the

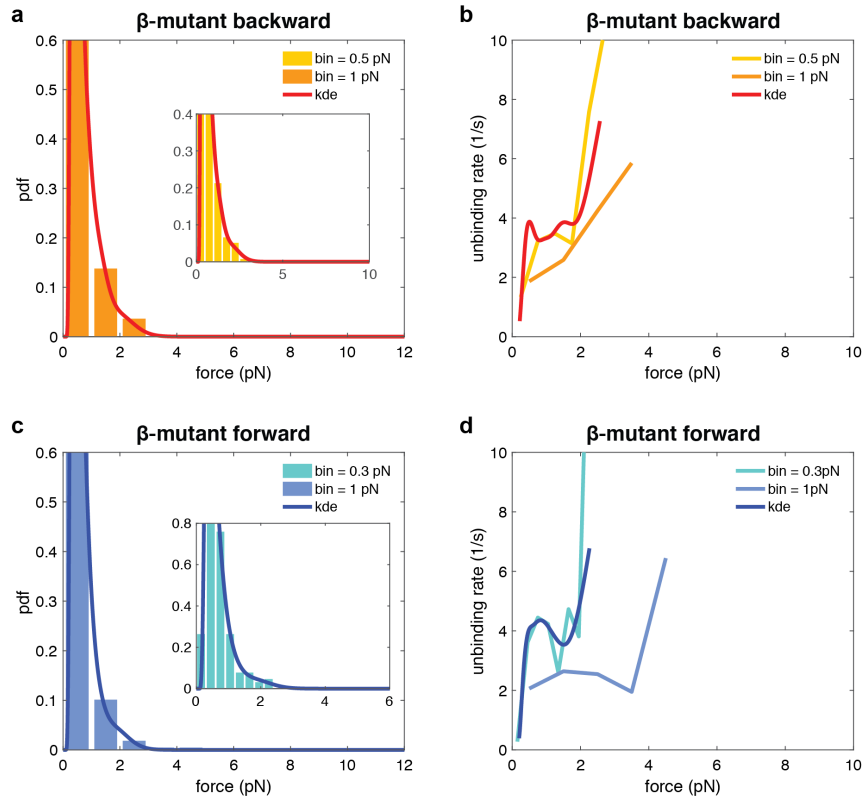
corresponding unbinding rates are displayed in *b* and *d* using the color code depicted in *a* and *b*, respectively).

Conversion of α -mutant Apo unbinding-force histograms into force-dependent unbinding rates:



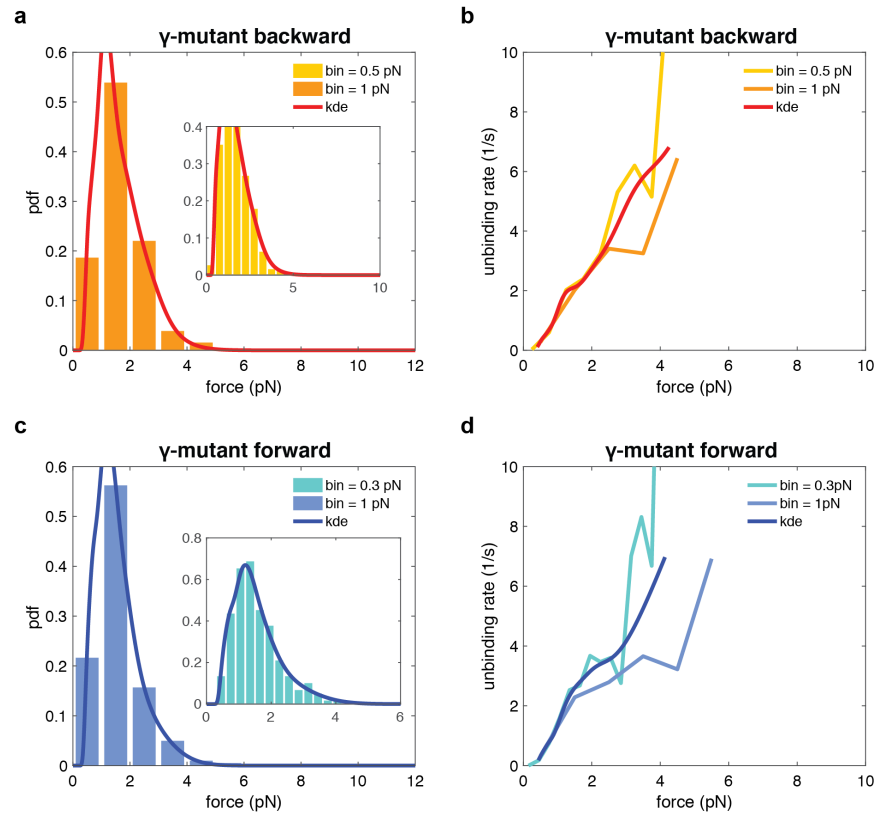
Supplementary Figure 29 As in Supplementary Fig. 28 but for the α -mutant with the cross-linked stalk helices.

Conversion of β -mutant Apo unbinding-force histograms into force-dependent unbinding rates:



Supplementary Figure 30 As in Supplementary Fig. 28 but for the β -mutant with the cross-linked stalk helices.

Conversion of γ -mutant Apo unbinding-force histograms into force-dependent unbinding rates:



Supplementary Figure 31 As in Supplementary Fig. 28 but for the γ -mutant with the cross-linked stalk helices.

Construct	Description	Genotype	Source
VY137	WT Dyn1 _{331kDa}	<i>pGAL-ZZ-TEV-GFP-3xHA-331DYN1</i>	Vale lab
VY863	AAA1 E/Q - Dyn1 _{331kDa}	<i>pGAL-ZZ-TEV-GFP-3xHA-331DYN1 (E1849Q)</i>	Vale lab
GY1	Dyn1 _{331kDa} - α	<i>pGAL-ZZ-TEV-GFP-3xHA-331DYN1 (K3077C, A3250C)</i>	This study
GY2	Dyn1 _{331kDa} - β	<i>pGAL-ZZ-TEV-GFP-3xHA-331DYN1 (I3076C, L3247C)</i>	This study
GY60	AAA1 E/Q-Dyn1 _{331kDa} - α	<i>pGAL-ZZ-TEV-GFP-3xHA-331DYN1 (E1849Q, K3077C, A3250C)</i>	This study
GY67	Δ BUT-Dyn1 _{331kDa}	<i>pGAL-ZZ-TEV-GFP-3xHA-331DYN1 (aa3556-3596 replaced with GSGS)</i>	This study
GY68	Δ BUT-Dyn1 _{471kDa}	<i>PAC11-13xMyc::TRP, nip100Δ::NAT, ZZ-TEV-GFP-GS-HaloTag-GS-3xHA-DYN1(aa3556-3596 replaced with GSGS)</i>	This study
GY71	Δ BUT-E3197K-Dyn1 _{331kDa}	<i>pGAL-ZZ-TEV-GFP-3xHA-331DYN1 (E3197K, aa3556-3596 replaced with GSGS)</i>	This study
GY201	F3446E-Dyn1 _{331kDa}	<i>pGAL-ZZ-TEV-GFP-3xHA-331DYN1 (F3446E)</i>	This study
GY205	F3446E-AAA3 E/Q + C-term GFP	<i>pGAL-ZZ-TEV-3xHA-331DYN1 (E2488Q, F3446E)-GFP</i>	This study
GY207	Dyn1 _{331kDa} - γ mutant	<i>pGAL-ZZ-TEV-GFP-3xHA-331DYN1 (K3077C, L3247C)</i>	This study
GY231	Δ BUT-Dyn1 _{331kDa} - α	<i>pGAL-ZZ-TEV-GFP-3xHA-331DYN1 (K3077C, A3250C, aa3556-3596 replaced with GSGS)</i>	This study
GY243	Dyn1 _{331kDa} with N-term SNAPf-tag	<i>pGAL-ZZ-TEV-GFP-SNAPf-3xHA-331DYN1</i>	This study

GY242	Dyn1 _{331kDa} - β with N-term SNAPf-tag	<i>pGAL-ZZ-TEV-GFP-SNAPf-3xHA-331DYN1 (I3076C, L3247C)</i>	This study
GY247	AAA1 E/Q - Dyn1 _{331kDa} with N-term SNAPf-tag	<i>pGAL-ZZ-TEV-GFP-SNAPf-3xHA-331DYN1 (E1849Q)</i>	This study
GY246	Δ BUT-Dyn1 _{331kDa} with N-term SNAPf-tag	<i>pGAL-ZZ-TEV-GFP-SNAPf-3xHA-331DYN1 (aa3556-3596 replaced with GSGS)</i>	This study
pFC15	SRS mouse dynein stalk MTBD 85:82	SRS-mouse dynein stalk MTBD 85:82-EGFP-6xHis	Cleary et al. 2014, Nat. Commun.
pSYS01	SRS yeast dynein stalk MTBD 85:82	SRS-yeast dynein stalk MTBD 85:82-EGFP-6xHis	This study
pSYS02	SRS yeast dynein stalk MTBD 89:82	SRS-yeast dynein stalk MTBD 89:82-EGFP-6xHis	This study
pSYS03	SRS yeast dynein stalk MTBD 85:82- α	SRS-yeast dynein stalk MTBD 85:82 (K3077C, A3250C) -EGFP-6xHis	This study
pSYS04	SRS yeast dynein stalk MTBD 85:82- β	SRS-yeast dynein stalk MTBD 85:82 (I3076C, L3247C) -EGFP-6xHis	This study
pSYS05	SRS yeast dynein stalk MTBD 89:82- β	SRS-yeast dynein stalk MTBD 89:82 (I3076C, L3247C) -EGFP-6xHis	This study

Table S1: Yeast strains and SRS constructs used in this work. “331DYN1” encodes amino acids 1219-4092 of Dyn1, with predicted molecular weight of 331 kDa (see Reck-Peterson et al. Cell 2016, and remark in footnote on page 8, section “Yeast culture and dynein purification” in Nicholas et al. PNAS 2015), and WT (“wild type”) represents the tail-truncated, single-headed dynein construct without AAA mutation. All yeast strains are based on W303 (*MATa/MAT α {leu2-3,112 trp1-1 can1-100 ura3-1 ade2-1 his3-11,15} [phi+]*) plus *pep4 Δ ::HIS3*, *prb1 Δ* . Except for GY68, all yeast strains express single-headed dyneins.

URA primers	
u1F	gtgattctgggtagaagatcgg
u2R	gagcaatgaaccaataacgaaatc
u3F	cttgacgttcgctcgactgatgagc
u4R	cgatgatgtagtttctggttttaa
URA insertion in stalk for GY1, GY2, GY60, GY207 & GY231	
Stalk-F-up	TGGAGAAATTGCCAAAAACCTTCA
Stalk-R-URA	<u>ccgatcttctaccagaatcac</u> AGCTTCACTAAGGCACGTAAACC
Stalk-F-URA	<u>ttaaaaaccagaactacatcatcg</u> CTGATTGGAAATTGCATAATTTTCAT
Stalk-R-down	ACCAATCTCCACCGTGACTCTG
GY1 & GY60	
Stalk-a1-R	AATATCTTTTT <u>gca</u> TTCCTCTGTAGCCTC
Stalk-a1-F	GAGGCTACAGAGGAA <u>tgc</u> AAAAAGATATT
Stalk-a2-R	TCATTTCTTCAGCGCAAG <u>aca</u> ATTGG
Stalk-a2-F	CCAAT <u>tgt</u> CTTGCCGCTGAAGAAATGA
GY2	
Stalk-b1-R	AATATCTT <u>aca</u> GATTTCTCTGTAGCCTC
Stalk-b1-F	GAGGCTACAGAGGAAATC <u>tgt</u> AAGATATT
Stalk-b2-R	TCATTTCTTC <u>aca</u> GGCAAGTAAATTGG
Stalk-b2-F	CCAATTTACTTGCC <u>tgt</u> GAAGAAATGA
GY207	
Stalk-a1-R	AATATCTTTTT <u>gca</u> TTCCTCTGTAGCCTC
Stalk-a1-F	GAGGCTACAGAGGAA <u>tgc</u> AAAAAGATATT
Stalk-b2-R	TCATTTCTTC <u>aca</u> GGCAAGTAAATTGG
Stalk-b2-F	CCAATTTACTTGCC <u>tgt</u> GAAGAAATGA
URA insertion in buttress for GY67	
But-F-up	GGATGGAGAATTCTTTGATCCAATC
But-R-URA	<u>ccgatcttctaccagaatcac</u> ATTCTCTTCTGTCAAAGTGATGTC
But-F-URA	<u>ttaaaaaccagaactacatcatcg</u> TATTCTATTATCGGTAAGCATAGTG
But-R-down	GTCAAGAGCGGTGGAGAAT
GY67 & GY68	
But-del-R	TTTTTCAAT <u>agaaccagaacc</u> GTATTCGGTATTCAATTTTATCAA

But-del-F	ACCGAATAC <u>cggttctggttct</u> ATTGAAAAAAGCTAAGTGAATCT
URA insertion in MTBD for GY71	
MTBD-F-up	CCAACTGGAGAGATATCCAACAA
MTBD-R-URA	<u>ccgatcttctaccagaatcac</u> ATAAGTAAAATTAGGATCTGACAA
MTBD-F-URA	<u>ttaaaaaccagaaactacatcatcg</u> ACAATTAACAGGGCCAGCAA
MTBD-R-down	TAGCCTGCACGTTACTCATT
GY71	
MTBD-EK-R	GCCCTGTTAATTGT <u>ttt</u> ATAAGTAAAA
MTBD-EK-F	TTTTACTTAT <u>aaa</u> ACAATTAACAGGGC
URA insertion in AAA5 for GY201 & GY205	
AAA5-F	CTTGAGTGTGGCTTGATAAGA
AAA5-R-URA	<u>ccgatcttctaccagaatcac</u> TCTAACTGCATTTTCTAATCTTTT
AAA5-F-URA	<u>ttaaaaaccagaaactacatcatcg</u> GAAGGAAGTGTAGTTATAATTCAGGA T
AAA5-R	TGGGATCGCAAGAGTGAATG
GY201 & GY205	
AAA5-FE-R	TACACTTC <u>ttc</u> TCTAACTGC
AAA5-FE-F	GCAGTTAG <u>Aaaa</u> GGAAGTGTA
Amplification of SNAPf-tag (S. cerevisiae codon optimized)	
SNAPf-F	ATGGATAAGGACTGCGAAATGAA
SNAPf-R	ACCCAAACCTGGTTTACCTAAT
GY242, GY243, GY246 & GY247	
DYN314-F-up	GTTTACATCATGGCTGACAAACA
DYN314-R-down	TGTTTGTCAGCCATGATGTAAAC
GFP-SG-R	cggcggcttctaataccgtATTACCCTGTTATCCCTATCTAGATTTGTACA ATTCATCCAT

Gal-F	acggattagaagccgccga
R-Sce-URA	ttatgtgagagtttaaaaaccagaaactacatcatcgTTATTTTCAGGAAAGTTTC GGAGG
u1F-RV	cgatgatgtagtttctggtttta
u2R-RV	CTTGACGTTTCGTTCTGACTGATGAGC
u3F-RV	GAGCAATGAACCCAATAACGAAATC
u4R-RV	gtgattctgggtagaagatcgg
GFP-URA-F	ccgatcttctaccagaaatcacGTTTACATCATGGCTGACAAACA
GFP-SNAPf-R	TTCATTTTCGCAGTCCTTATCCATACTACCTCTAGATTTGTACAAT TCATCCATAC
SNAPf-HA-F	ATTAGGTAAACCAGGTTTGGGTGGTTCATACCCATACGATGTT CCTGAC
Replacement of mouse dynein stalk- MTBD with S. cerevisiae dyneins talk- MTBD in pFC15	
SRS-F	CTTGAGGCACTTCTCCTGC
SRS-R	GAGCCATGAAGTctgcagCGAAACGTAACAGTGCTTCTTC
Sc85-F	GCACTGTTAGCTgtcgacGTAGGTCTCGAAAACTAAACG
Sc89-F	GCACTGTTAGCTgtcgacAGATTTGTTAATGTAGGTCTCGAAA
Sc82-R	GCAGGAGAAGTGCCTCAAGAGTGTTTCAGCCACCTTTCTTTTC
CC1 – α mutation	
CC1a-F	AGAGGAAATCtgcAAGATATTGAAAGTACAAGAAG
CC1a-R	GTAGCCTCCTGCTTTCTTTC
CC2 – α mutation	
CC2a-F	TTTACTTGCCtgtGAAGAAATGACACAGG
CC2a-R	TTGGCCTTCGTCTTCAATG
CC1 – β mutation	
CC1b-F	TACAGAGGAAtgcAAAAAGATATTGAAAGTACAAG
CC1b-R	GCCTCCTGCTTTCTTTCC
CC2 – β mutation	
CC2b-F	GAAGGCCAATtgtCTTGCCGCTG

CC2b-R	GTCTTCAATGATTCGAACTCTATTC
--------	---------------------------

Table S2: List of primers used for the generation of yeast strains and SRS constructs.

Supplementary References

1. Gutiérrez-Medina, B., Fehr, A.N. & Block, S.M. Direct measurements of kinesin torsional properties reveal flexible domains and occasional stalk reversals during stepping. *Proc Natl Acad Sci USA* **106**, 17007-17012 (2009).
2. Cleary, F.B. et al. Tension on the linker gates the ATP-dependent release of dynein from microtubules. *Nat Commun* **5**, 4587 (2014).
3. Svoboda, K. & Block, S.M. Biological applications of optical forces. *Annu Rev Biophys Biomol Struct* **23**, 247-285 (1994).
4. Nicholas, M.P., Rao, L. & Gennerich, A. An improved optical tweezers assay for measuring the force generation of single Kinesin molecules. *Methods Mol Biol* **1136**, 171-246 (2014).
5. Ray, C., Brown, J.R. & Akhremitchev, B.B. Correction of systematic errors in single-molecule force spectroscopy with polymeric tethers by atomic force microscopy. *J Phys Chem B* **111**, 1963-1974 (2007).
6. Munoz, V. & Cerminara, M. When fast is better: protein folding fundamentals and mechanisms from ultrafast approaches. *Biochem J* **473**, 2545-2559 (2016).
7. Dudko, O.K., Hummer, G. & Szabo, A. Theory, analysis, and interpretation of single-molecule force spectroscopy experiments. *Proc Natl Acad Sci USA* **105**, 15755-15760 (2008).
8. Nicholas, M.P. et al. Cytoplasmic dynein regulates its attachment to microtubules via nucleotide state-switched mechanosensing at multiple AAA domains. *Proc Natl Acad Sci USA* **112**, 6371-6376 (2015).